2018

Combustion Behavior Of Sub-Millimeter Sized Oxygenated And N-Alkane Fuel Droplets

Mohammad Fahd Ebna Alam
University of South Carolina

COMBUSTION BEHAVIOR OF SUB-MILLIMETER SIZED OXYGENATED AND N-ALKANE FUEL DROPLETS

by

Mohammad Fahd Ebna Alam

Bachelor of Science
Bangladesh University of Engineering & Technology, 2007

Master of Science
National University of Singapore, 2012

Submitted in Partial Fulfillment of the Requirements

For the Degree of Doctor of Philosophy in

Mechanical Engineering

College of Engineering and Computing

University of South Carolina

2018

Accepted by:

Tanvir I. Farouk, Major Professor

Bihter Padak, Committee Member

Chen Li, Committee Member

Jamil A. Khan, Committee Member

Cheryl L. Addy, Vice Provost and Dean of the Graduate School

DEDICATION

This thesis is dedicated to the taxpayers of *Bangladesh*, *Singapore* and *the United States of America* whose unconditional generous support, often perceived as '*indirect*', enabled me to enjoy a near tuition-free undergraduate and graduate level academic experience.

ACKNOWLEDGMENTS

The author expresses his sincere gratitude towards numerous researchers, colleagues, educators and family members for their relentless support and sacrifices during the course of this Ph.D. work. To adequately thank and state their unconditional help and love, this mere 'acknowledgment' is a small token of appreciation for a much greater noble contribution in my life. I wish to thank them all.

First, I would like to thank all the University of South Carolina officials and staffs whose 'behind the curtain' role unequivocally made my Ph.D. journey smooth and enjoyable. To be more specific, within the mechanical engineering department, I want to accolade Ms. Misty O'Donnell, Ms. Lalitha Ravi and Ms. Renee Jenkins for their assistance. I also appreciate my thesis committee members (Dr. Jamil Khan, Dr. Bihter Padak, and Dr. Chen Li), for their time, guidance and suggestion. In addition, special appreciation to the NASA is rightfully due to its generous financial aid throughout the entire doctoral period. Other funding organizations, namely- U of SC graduate school, the ASGSR, the Combustion Institute are also acknowledged.

I believe the old English adage *'A person is known by the company he keeps'* is undeniably true for the graduate students. Indeed, I have been blessed and benefitted from my 'ReActing Systems and Advanced Energy Research (RASAER)' lab mates in numerous ways. Their prudence, perseverance, and friendship have enriched me to grow over time as a better researcher. Outside the U of SC, my friends and coworkers at the Princeton University and the National University of Singapore are thankfully

acknowledged. Special thanks to Mac Haas and Sang Hee Won for their long-lasting research impact on me.

Perhaps some relation works best when not institutionalized, and Frederick L. Dryer is a perfect example in relation to my graduate research. His immense wisdom, creativity, and passion for scientific inquisitiveness have remarkably influenced me over these years. I feel delighted considering that through his scientific legacy I found my Ph.D. mentor at the U of SC.

I would like to sincerely thank my parents (Mrs. Farida Yeasmin and Mr. AZM Shah Alam) for their life-long supports and sacrifices. Without their selfless commitment, I would have never come this far where I belong now. And, a very special thank to my wife Dr. Tamanna Alam for her angelic presence in my life and work.

Finally, I offer my sincerest gratitude to Dr. Tanvir Farouk, for his care, guidance, support, hope, advice, motivation, and mentorship for the last five years. It has truly been an honor and amazing experience working with you.

ABSTRACT

The primary scientific explorations of this thesis work are to better understand (a) microgravity fire-suppression of untested extinguisher, (b) combustion kinetic model refinement of renewable fuel butanol (C_4H_9OH) isomers, and (c) directly induced cool flame dynamics of higher n-alkane fuels from an isolated small droplet combustion perspective employing computational fluid dynamics with comprehensive chemical kinetics. The chronological development of the research direction shifts from a relatively small fuel like methanol (CH_3OH) to heavier straight paraffinic fuel n-decane (n-$C_{10}H_{22}$). The first installment of the thesis is directed towards answering the feasibility of then-newly considered fire suppressant xenon (Xe) for microgravity space application by the National Aeronautics and Space Administration (NASA). Methanol was used as model fuel to assess the combustion behavior under xenon-rich environment. The comprehensive analysis revealed that xenon promotes longer burning time and higher flame temperature compared to existing other diluents/extinguishers and can support hot flame with much lesser oxygen content than its counterparts. The exceptionally low thermal diffusivity of xenon is identified to be responsible for the significantly higher peak gas temperature and prolonged burn time. This detailed analysis clearly debilitates the potential of xenon as a next-generation fire-suppressant for microgravity applications and helped NASA in safeguard financial investment for International Space Station (ISS) experiments using xenon.

The second installment of the thesis outlines the efforts directed towards improving the gas phase kinetic model of butanol isomers based on droplet combustion experiments and computations. This is a unique contribution where the traditional gas-phase experiment/theory-driven kinetic model is further refined in light of critical recommendations from the droplet combustion analysis. The comprehensive kinetic model of Sarathy et al. (*Combust. Flame, 2012*) is one of the two widely used model for butanol isomers which has been extensively validated against homogeneous gas phase experiments. The numerical simulation of the butanol droplet combustion experiments at atmospheric conditions predicted the faster burning rate and larger flame diameter using the above model. An exhaustive perturbation analysis is carried on chemical, thermodynamic and transport parameters influences (while simultaneously isolating their cross-influences) to pinpoint the root cause of faster burning tendency of the model. The synthesized results from this huge variable-matric perturbation revealed that the isomer-specific species transport parameters were culpable, and recommendations were made to update those Lennard-Jones potential parameters. Once updated, the computational predictions significantly improves for the *Sarathy et al.* model based on the feedback from droplet combustion.

The final segment of the thesis discusses the direct initiation of cool flame combustion for submillimeter-sized higher n-alkane droplets (n-heptane and n-decane) for possible terrestrial experiments without the necessity of radiative extinction as frequently encountered onboard the ISS experiments. It has been found that the dimensionality of the droplet (D_o = 0.5 mm) statistically reduces the possibility of achieving direct cool flame burn for the droplet by simply varying the ignition energy

initiation. Therefore, it was conceptualized that a combination of a reduced ignition source and induction chemistry modulation may hold the possibility of direct initiation of cool flame for n-C_7H_{16} and n-$C_{10}H_{22}$ even in ground-based drop tower experiments. To facilitate this idea, we numerically investigate the droplet combustion under selective ozone (O_3) augmented ambient where O_3 serves as an induction chemistry modulator through its liberation of atomic O via molecular decomposition. The available atomic O then reacts with the surrounding fuel producing OH radical, and eventually water and heat. This latter heat input acts as a secondary thermal feedback to the droplet surface maintaining steady surface burning rate which then stabilizes the cool flame very near the droplet surface. It was found that the fuel physical properties, especially flash point, play a decisive role in determining the nature of the initial cool flame dynamics and the ozone requirements. Higher flash point fuel (here, n-$C_{10}H_{22}$) is likely to undergo initial dumped cool flame oscillation than its lower value counterpart (n-C_7H_{16}) and will require higher O_3 loading under identical ambient. In the near-limit condition, such directly introduced cool flame fails to attain a steady burn and enters into a continuously evolving oscillatory cool flame. Analyses further indicate that the dynamic interaction of degenerate chain branching and chain termination/propagation reaction classes of QOOH (Q=C_nH_{2n}) species associated with the low-temperature kinetic regimes, and continuous fuel leakage across the flame location contribute to the ever-increasing trends of the oscillation magnitude.

PREFACE

This thesis reports the combustion behavior of sphero-symmetric small droplets for two different classes of fuels (oxygenated alcohols and n-alkanes) under diversified ambient conditions with the individual unique objective for each study. The research outcomes from this dissertation work were timely published in the leading combustion field-specific journals. The author prepared the thesis chapters 3-7 (in consultation with the thesis adviser) from those published articles with necessary amendments following the guidelines from the graduate school of the University of South Carolina, SC, USA. As a consequence, chapter relevant thorough background information from literature is provided at the beginning of each chapter. However, an abridged critical review of the droplet combustion literature is also included in the 1st chapter to complement the rationale of this Ph.D. work. It should be noted that the necessary approval from the publishing agencies and collaborators were sought in advance for this dissertation. The list of correlated chapters and the associated published article can be found on page 11.

TABLE OF CONTENTS

LIST OF TABLES

LIST OF FIGURES

CHAPTER 1

INTRODUCTION

1.1 PROBLEM STATEMENT

The efficient conversion of fossil fuels to useful energy has been an active area of research ever since the development of steam engine by Sir James Watt and the post-industrial revolution [1]. Since then, fossil fuels have incredibly the preferred choice of energy production in the form of '*shaft output*' from the prime movers (i.e., engines, gas turbines, propellers, boilers and so on). Consequently, it is anticipated that the fossil fuels (gaseous and condensed phase) will also remain the automatic choice of ground, marine and aviation transportation systems for forth-coming future [2]. Such a prolific use of fossil fuels is primarily due to their extraordinary energy density irrespective of any defined metric (unit mass or volume basis) as illustrated in Figs. 1.1 and 1.2. Therefore, despite the resurgence of renewable energy sources in recent times (solar, wind, tidal, biomass etc.), combustion technology will remain the principal source of energy conversion for centuries.

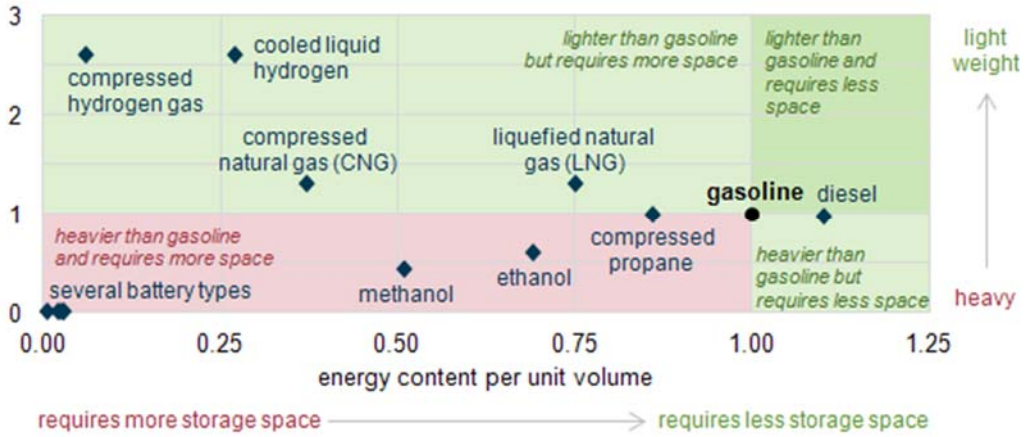

Figure 1.1 Comparison of energy content per unit volume for different fossil fuels and battery types (normalized against the conventional gasoline). Courtesy- United States energy information administration (https://www.eia.gov).

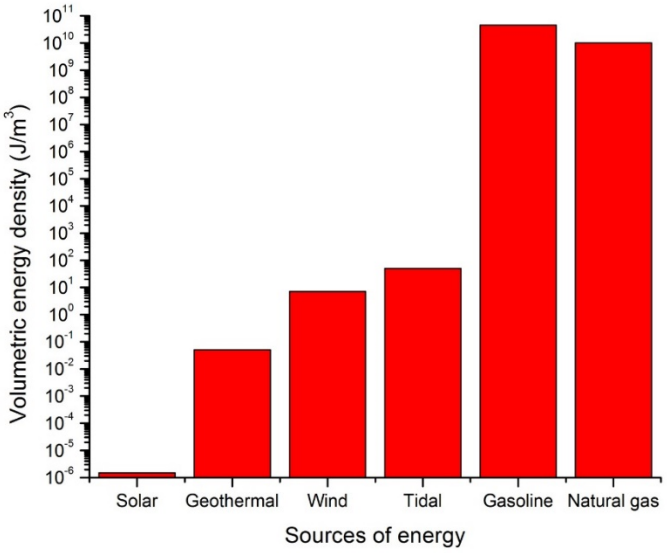

Figure 1.2 Comparison of volumetric energy density for different energy sources. The plot is recreated after the reported data in reference [3]. Data for wind is for 5 m/s.

However, the boon of combustion technology is not a singular entity and is often rationally criticized for contributing to the harmful emissions, posing detrimental effects on the environment as well as human health. Therefore, modern combustion technology simultaneously aims for higher conversion efficiency and lower perilous emission to tackle the ever stringent regulatory constraints [4, 5]. In relation to the fuel combustion, its ignition, flame development, and pollutant formation are inevitably interconnected. Therefore, the fundamental insights regarding the flame dynamics and species evolutions (including the harmful ones) are typically studied in standardized combustion and/or oxidation settings at desired thermodynamic states (P, T). Historically, such fundamental endeavors are carried out extensively using shock tubes [6], flow reactors [7], jet-stirred reactors [8], rapid compression machines [9], burner stabilized premixed flames [10] and opposed diffusion flame burners [11]. Although these test facilities are far from practical ideality for combustion devices, they offer unique opportunities to individually study ignition, flame characteristics and species evolution (i.e., reaction kinetics). In addition,

due to their simplified flow field, the detail kinetic analysis is possible for these zero- or one-dimensional problems. While these experimental platforms and associated kinetic analyses serve as the foundational stage for the combustion research, they have two major concerns- (a) the studies have to be conducted in gas phase reactant mixtures, and (b) they are either steady state [7, 8, 10, 11] with transport effect, or transient in nature [6, 9] ignoring altogether the transport effect. Therefore, there exists a natural gap in studying the fuel combustion considering both the unsteady flame dynamics and the transport effect. The investigation of isolated single fuel droplet combustion in absence of (under significantly reduced) gravity offers a unique opportunity to probe liquid fuel combustion under unsteady transport dependent environment [12]. With such an advantageous canonical configuration, the physical problem becomes classical Stefan flow problem [13] where enthalpy and species transports are one-dimensional in radial coordinate. Computationally, such a facile reacting fluid domain can be modeled with detailed kinetics [14, 15], even to validate associated submodels, e.g., radiation model [16, 17], transport model (multicomponent vs. mixture average) [18] and water dissolution model [15, 19-21].

Interestingly, although one-dimensional droplet combustion may appear simple in configuration, it has relevance to the complex spray environment by incorporating moving boundary effects, unsteady heat conduction and mass diffusion in the droplet and surrounding gas, variable properties (dependent on temperature and composition), phase equilibrium at the interface, radiation dynamics, and a detailed kinetic mechanism for the combustion process. Traditionally, isolated droplet combustion studies (with or without the gravity) are conducted to understand the fuel ignition, burning rate characteristics, flame

dynamics and spreading [22-24]. Therefore, there is a need to explore the outer regime of conventionality to apply droplet combustion approach, namely- (a) fire extinguishment, (b) kinetic model validation and improvement, and (c) new combustion technology study. This thesis work is dedicated to exploring these less-ventured pathways where computational droplet combustion can enhance the understanding of liquid fuel combustion.

1.2 LITERATURE REVIEW

Study of single isolated or array of isolated droplets has existed nearly seven decades since the pioneering work of G.A.E. Godsave [25, 26]. These initial investigations were primarily empirical in nature, therefore covering a wide range of fuels, e.g., benzene, tertiary butyl benzene, decalin, n-heptane etc. Along the line, Kumagai and coworkers were the forerunners in studying the combustion behavior of isolated droplet under reduced gravity environment [27, 28]. These investigators are the first to conduct research on spherical diffusion flames in absence of gravity and formulated a theoretical framework to study it numerically. In an independent study, Goldsmith and Penner [29] improved the simplified model of Godsave and also performed extensive experimental investigations [30] to delineate the role of increased ambient oxidizer, pressure and temperature on burning rate. To further excel in understanding the droplet combustion in terms of high-pressure, Spalding [31] proposed a transient theoretical model to determine the frame locations and burning rate at elevated pressure conditions. By deploying statistical formulations, Willams [32] then tried to predict the droplet growth, new droplet formation, collision and aerodynamic forces on droplets under spray condition. He further explored the validity of typical droplet burning steady-state assumptions and showed that these

simplifying assumptions can lead up to 20% error in predictions [33]. In contemporary time, researchers also engaged continuous photography and video recording techniques [34] to understand the dynamics of droplet combustion. As the importance of droplet combustion became more prominent from spray perspective, researchers like Hottel et al. [35] experimentally pursued the combustion behavior of different heavy fuels.

The pivotal works of the fifties (i.e., till 1960) played an instrumental role to motivate the researchers to study droplet combustion with multifaceted research objectives. Combustion of the droplet and its subsequent burning behavior has been studied for rocket combustor application [36], high-pressure systems [37-39], denotation configuration [40], super-critical condition [41], evaporation model development [42] and for the ignition and extinction of droplets [43, 44]. Kassoy and Williams are the first to propose a theoretical formulation accounting for variable property effect on droplet combustion along with finite rate chemistry [45], and showed that numerical predictions improved significantly over constant fluid property approach.

A critical evaluation of the presented studies suggests that while these improved our understanding of droplet combustion, they are based either convective experiments (forced or/and natural) or simplified computations, both of which required further research to address complicated spray environment. Consequently, there had been a necessity to address more practically relevant droplet combustion studies. In their innovative experiments, Faeth and Lazar [46] conducted tests for droplet combustion of alcohol and paraffinic fuels in the downstream of the flat flame burner to emulate droplet burning under gaseous product distribution environment. These authors also extended their research efforts towards bipropellant droplet combustion near critical point condition [47]. In an

independent study, Kumagai et al. [48] conducted a '*paradigm-shift*' study of isolated droplet combustion under free-fall condition retaining the spherical flame configuration to decoupling the role of external convective perturbation. Concurrently, Aldred and coworkers [49] experimentally explored the transient dynamics of relatively smaller droplet combustion with a conclusion of the inadequacy of the-then existing theoretical models. In the form of theoretical treatment, Law [50] proposed an asymptotic analysis of ignition and extinction of liquid fuel droplet which was then further improved to account the internal mixing considering the unsteady effect of multicomponent droplet [51]. Based on this contributing works, Law and Sirignano [52, 53] developed fully transient droplet combustion model. Crespo and Linan [54] also deployed asymptotic analysis to explore the effect of unsteady effects of droplet combustion and evaporation. In pursuit of developing more realistic theoretical models, Law et al. [55] improved their previous formulations incorporating the convective effect to unsteady multicomponent model. By the late 1970s, an emulsion of water-fuel mixture received attention across the combustion communities due to its relevance to practical application, and it was venture as a binary mixture under droplet configuration [56-58]. At this point, the research direction steered towards a better understanding of the role of reaction chemistry on droplet combustion through finite rate kinetics [59, 60]. Expressing the hot flame chemistry with single irreversible reaction step, Sirignano [61, 62] refined the previously developed single droplet theory under convective environment. Comprehensive details of the literature discussed so far can also be found in the review article of Law [63] and Faeth [64].

With the advancement of computational tools and diagnostics capabilities, freely falling [65] and micro- and/or reduced-gravity [66-68] droplet combustion gained

popularity due to its geometrical constraint with well-defined boundary conditions. The works lead by F.L. Dryer at the Princeton University were the first to deploy computational fluid dynamics (CFD) in analyzing sphero-symmetric droplet combustion invoking detailed kinetics [69, 70]. These authors have successfully demonstrated the necessity of detailed kinetics in reproducing the experimental targets against reduced- or micro-gravity tests [71]. At this point in time, a careful synthesis of four decades of droplet combustion research (1950s-1990s) illustrates that the research thrust was first initiated by the empirical terrestrial experimentation (with or without gravity) which simultaneously led to the theoretical development of isolated droplet combustion phenomena. Subsequently, the role of chemistry was included in numerical consideration through single-step finite rate chemistry, and finally the development of CFD analysis with detailed kinetics.

Beginning in the early nineties (the 1990s), the research direction with isolated droplet combustion shifts from global observational and/or fundamental targets to individualistic physical phenomena base understanding. To accommodate such objectives, methanol (CH_3OH) was a generic choice of fuel due to its simplified chemistry and non-sooting tendency [16, 19-21, 72-81]. To a lesser extent, ethanol was also studied for reduced gravity ambient [15]. These relatively recent studies primarily enriched our knowledge for specific physical cases, e.g.- water dissolution, diffusion and internal mixing limit, radiation influence on burning etc. Subsequently, researchers across the globe contributed to pushing the frontier limit of isolated sphero-symmetric droplet combustion for complex fuels and their mixtures [14, 18, 82-91] considering the necessity of practicality and to explaining the emergence of new combustion concepts (e.g., multiphase cool flames [92, 93]). To highlight the phenomenal scientific contributions originating

from the isolated droplet combustion study over the last three decades is beyond the scope of this literature review, and is well documented in the review articles of Aggarwal [23] and Sirignano [24], and in respective chapters hereafter. However, a careful reexamination of all these major studies shows that the isolated droplet combustion can be further deployed to harness deeper insight for (a) fire suppressant effectiveness, (b) improving/refining detailed chemistry to complex fuels, and (c) oscillatory behavior of low temperature driven cool flames. This existing knowledge gap was the main intrinsic motivation to pursue this dissertation work in the field of isolated droplet combustion employing high fidelity CFD code with detailed kinetics.

1.3 SCOPE AND ORGANIZATION OF THE THESIS WORK

Since the seminal works of Godsave [25, 26], attention for isolated droplet has been given exclusively for large diameter droplets (order of several millimeters, analytical/experimental/computational) including the experiments conducted onboard the international space station [89]. To facilitate a gravityless environment for large diameter droplets, testings were primarily conducted in either space shuttle experiments or in the ISS as a terrestrial test site would demand very high drop tower free-fall height. To the contrary, smaller droplets (D_o < 1.0 mm) require much less drop hight, thus opening the opportunity to do the testing in ground-based facility avoiding the expansive space-based testing [94]. This thesis work focuses on the numerical analysis of small diameter droplet combustion for a variety of practical fuels to extend the potentiality of droplet combustion in understanding the fire dynamics, reaction kinetics, and cool flame combustion.

Chapter 1 briefly introduces the general problem statement of this thesis work, followed by its scopes and organization. This chapter also registers the significant archival publications arising from this Ph.D. research.

Chapter 2 outlines the details of the numerical framework of the one-dimensional droplet combustion code that has been used in this thesis. This chapter first introduces the general conservation equations followed by the descriptions of the sub-models incorporated here, namely- radiation, diffusion, fiber heat feedback and water dissolution models.

Chapters 3-7 contain the core sections of this thesis research. As already hinted, the broader goal of this investigation is to extend the droplet combustion capability to the field of fire extinction, reaction kinetics and new combustion concept (here, the cool flame of the smaller droplet). In chapter 3, the potential of an untested fire extinguisher gas- xenon (Xe), for microgravity application is explored through the computation of droplet combustion. Methanol has been used as model fuel for this study and a prior validation of the computation was made against NASA ISS FLEX-563 test data containing 63% (v/v) of xenon. Necessary recommendations were made to the NASA for xenon's limiting viability as a next-generation fire suppressant.

Chapter 4 and 5 discuss the combustion analysis of n-butanol and its isomers primarily focusing on the kinetic aspects as viewed from smaller droplet burning perspective. These studies are also complemented by the experimental counterpart performed by the collaborators at the Cornell University (led by Professor C.T. Avedisian) in a drop tower facility supporting small droplet combustion ($D_o < 0.6$ mm).

Chapter 6 shifts the research direction towards the numerical exploration of a concurrent new research topic- 'cool flame' from multiphase droplet perspective. Cool flame phenomena in droplet configuration have been investigated previously for large diameters only with a preceding extinction of the precursor hot flame. Here, we advance the mechanistic concept of directly instituted cool flame for sub-millimeter sized n-alkane (n-C_7H_{16}, n-$C_{10}H_{22}$) droplets without the necessity of radiative extinction of the hot flame. Subsequently, in chapter 7, the cool flame has been studied in a near-limiting condition where a quasi-steady cool flame transitions to an ever-increasing oscillatory flame. The inception, growth, and dynamics of such an oscillatory flame are discussed at length in this chapter. Finally, chapter 8 serves as the closure of this thesis highlighting major contributions and recommendations for future research direction.

1.4 PEER-REVIEWED PUBLICATIONS

i. **F.E. Alam**, T.I. Farouk, F.L. Dryer. Computational study of oscillatory 'cool flame' for sub-millimeter sized n-heptane droplet. Accepted for publication in the Proceedings of the Combustion Institute (2018). Thesis chapter # 7.

ii. **F.E. Alam**, S.H. Won, T.I. Farouk, F.L. Dryer. Ozone assisted cool flame combustion of sub-millimeter sized n-alkane droplets at atmospheric and higher pressure. In press status, Combustion & Flame, 2018. Thesis chapter # 6.

iii. T.I. Farouk, D. Dietrich, **F.E. Alam**, F.L. Dryer. Isolated n-decane droplet combustion - dual stage and single stage transition to "cool flame" droplet burning. Proceeding of the Combustion Institute (Volume 36, 2017). Thesis chapter # 6.

iv. Y.C. Liu[§], **F.E. Alam**[§], Y. Xu, F.L. Dryer, C.T. Avedisian, T.I. Farouk. Combustion

characteristics of butanol isomers in multiphase configurations. Combustion & Flame (Volume 169, 2016). [§]Equal contributing author. Thesis chapter # 5.

v. **F.E. Alam**, T.I. Farouk, F.L. Dryer. Effectiveness of xenon as fire suppressant under microgravity combustion environment. Combustion Science & Technology (Volume 88, 2016). Thesis chapter # 3.

vi. **F.E. Alam**, Y.C. Liu, C.T. Avedisian, F.L. Dryer, T.I. Farouk. n-Butanol droplet combustion: numerical modeling and reduced gravity experiments. Proceeding of the Combustion Institute (Volume 35, 2015). Thesis chapter # 4.

vii. **F.E. Alam**, F.M. Haas, T.I. Farouk, F.L. Dryer. Influence of trace nitrogen oxides on natural gas oxidation: flow reactor measurements and kinetic modeling. Energy & Fuels (Volume 31, 2017). *This article is not related to the droplet combustion, however, it was published during the Ph.D. tenure.*

1.5 REFERENCES

[1] R.C. Allen, The British Industrial Revolution in Global Perspective, Cambridge University Press, Cambridge, 2009.

[2] C. National Research, Transforming Combustion Research through Cyberinfrastructure, The National Academies Press, Washington, DC, 2011.

[3] B.E. Layton, A Comparison of Energy Densities of Prevalent Energy Sources in Units of Joules Per Cubic Meter, International Journal of Green Energy, 5 (2008) 438-455.

[4] J.E. Dec, Advanced compression-ignition engines—understanding the in-cylinder processes, Proceedings of the Combustion Institute, 32 (2009) 2727-2742.

[5] R.D. Reitz, G. Duraisamy, Review of high efficiency and clean reactivity controlled compression ignition (RCCI) combustion in internal combustion engines, Progress in Energy and Combustion Science, 46 (2015) 12-71.

[6] R.K. Hanson, D.F. Davidson, Recent advances in laser absorption and shock tube methods for studies of combustion chemistry, Progress in Energy and Combustion Science, 44 (2014) 103-114.

[7] F.L. Dryer, F.M. Haas, J. Santner, T.I. Farouk, M. Chaos, Interpreting chemical kinetics from complex reaction–advection–diffusion systems: Modeling of flow reactors and related experiments, Progress in Energy and Combustion Science, 44 (2014) 19-39.

[8] O. Herbinet, G. Dayma, Jet-Stirred Reactors, in: F. Battin-Leclerc, J.M. Simmie, E. Blurock (Eds.) Cleaner Combustion: Developing Detailed Chemical Kinetic Models, Springer London, London, 2013, pp. 183-210.

[9] S.S. Goldsborough, S. Hochgreb, G. Vanhove, M.S. Wooldridge, H.J. Curran, C.-J. Sung, Advances in rapid compression machine studies of low- and intermediate-

temperature autoignition phenomena, Progress in Energy and Combustion Science, 63 (2017) 1-78.

[10] F.N. Egolfopoulos, N. Hansen, Y. Ju, K. Kohse-Höinghaus, C.K. Law, F. Qi, Advances and challenges in laminar flame experiments and implications for combustion chemistry, Progress in Energy and Combustion Science, 43 (2014) 36-67.

[11] U. Niemann, K. Seshadri, F.A. Williams, Accuracies of laminar counterflow flame experiments, Combustion and Flame, 162 (2015) 1540-1549.

[12] M.Y. Choi, F.L. Dryer, Microgravity Combustion: Fire in Free Fall (in *Microgravity Droplet Combustion*), in: H.D. Ross (Ed.), Academic Press, 2001, pp. 183-297.

[13] F.A. Williams, Combustion Theory, 2nd ed., Westview Press, Boulder, Colorado, USA, 1994.

[14] A.J. Marchese, F.L. Dryer, V. Nayagam, Numerical modeling of isolated n-alkane droplet flames: initial comparisons with ground and space-based microgravity experiments, Combustion and Flame, 116 (1999) 432-459.

[15] A. Kazakov, J. Conley, F.L. Dryer, Detailed modeling of an isolated, ethanol droplet combustion under microgravity conditions, Combustion and Flame, 134 (2003) 301-314.

[16] A.J. Marchese, F.L. Dryer, The Effect of Non-Luminous Thermal Radiation in Microgravity Droplet Combustion, Combustion Science and Technology, 124 (1997) 371-402.

[17] A.J. Marchese, F.L. Dryer, R.O. Colantonio, Radiative effects in space-based methanol/water droplet combustion experiments, Symposium (International) on Combustion, 27 (1998) 2627-2634.

[18] K.G. Kroenlein, Numerical Simulation of Isolated Droplet Combustion Under Microgravity Conditions, in: Doctoral Thesis, Mechanical & Aerospace Engineering, Princeton University, NJ, USA, 2007.

[19] A.J. Marchese, F.L. Dryer, The effect of liquid mass transport on the combustion and extinction of bicomponent droplets of methanol and water, Combustion and Flame, 105 (1996) 104-122.

[20] A. Lee, C.K. Law, An Experimental Investigation On the Vaporization and Combustion of Methanol and Ethanol Droplets, Combustion Science and Technology, 86 (1992) 253-265.

[21] B.L. Zhang, F.A. Williams, Alcohol droplet combustion, Acta Astronautica, 39 (1996) 599-603.

[22] S.S. Sazhin, Advanced models of fuel droplet heating and evaporation, Progress in Energy and Combustion Science, 32 (2006) 162-214.

[23] S.K. Aggarwal, Single droplet ignition: Theoretical analyses and experimental findings, Progress in Energy and Combustion Science, 45 (2014) 79-107.

[24] W.A. Sirignano, Advances in droplet array combustion theory and modeling, Progress in Energy and Combustion Science, 42 (2014) 54-86.

[25] G.A.E. Godsave, Combustion of Droplets in a Fuel Spray, Nature, 164 (1949) 708.

[26] G.A.E. Godsave, Studies of the combustion of drops in a fuel spray—the burning of single drops of fuel, Symposium (International) on Combustion, 4 (1953) 818-830.

[27] S. Kumagai, H. Isoda, Combustion of fuel droplets in a falling chamber, Symposium (International) on Combustion, 6 (1957) 726-731.

[28] H. Isoda, S. Kumagai, New aspects of droplet combustion, Symposium (International) on Combustion, 7 (1958) 523-531.

[29] M. Goldsmith, On the Burning of Single Drops of Fuel in an Oxidizing Atmosphere, Journal of Jet Propulsion, 24 (1954) 245-251.

[30] M. Goldsmith, Experiments on the Burning of Single Drops of Fuel, Journal of Jet Propulsion, 26 (1956) 172-178.

[31] D.B. Spalding, Theory of Particle Combustion at High Pressures, ARS Journal, 29 (1959) 828-835.

[32] F.A. Williams, Spray Combustion and Atomization, The Physics of Fluids, 1 (1958) 541-545.

[33] F.A. Williams, On the Assumptions Underlying Droplet Vaporization and Combustion Theories, The Journal of Chemical Physics, 33 (1960) 133-144.

[34] K. Kobayasi, An experimental study on the combustion of a fuel droplet, Symposium (International) on Combustion, 5 (1955) 141-148.

[35] H.C. Hottel, G.C. Williams, H.C. Simpson, Combustion of droplets of heavy liquid fuels, Symposium (International) on Combustion, 5 (1955) 101-129.

[36] R.S. Levine, Experimental status of high frequency liquid rocket combustion instability, Symposium (International) on Combustion, 10 (1965) 1083-1099.

[37] T.A. Brzustowski, R. Natarajan, Combustion of aniline droplets at high pressures, The Canadian Journal of Chemical Engineering, 44 (1966) 194-201.

[38] D.E. Rosner, On liquid droplet combustion at high pressures, AIAA Journal, 5 (1967) 163-166.

[39] R. Natarajan, T.A. Brzustowski, Some New Observations on the Combustion of Hydrocarbon Droplets at Elevated Pressures, Combustion Science and Technology, 2 (1970) 259-269.

[40] F.B. Cramer, The onset of detonation in a droplet combustion field, Symposium (International) on Combustion, 9 (1963) 482-487.

[41] G.M. Faeth, D.P. Dominicis, J.F. Tulpinsky, D.R. Olson, Supercritical bipropellant droplet combustion, Symposium (International) on Combustion, 12 (1969) 9-18.

[42] S. Kotake, T. Okazaki, Evaporation and combustion of a fuel droplet, International Journal of Heat and Mass Transfer, 12 (1969) 595-609.

[43] C.E. Polymeropoulos, R.L. Peskin, Ignition and extinction of liquid fuel drops—Numerical computations, Combustion and Flame, 13 (1969) 166-172.

[44] J.W.A. Rosser, B.J. Wood, An experimental study of fuel droplet ignition, AIAA Journal, 7 (1969) 2288-2292.

[45] D.R. Kassoy, F.A. Williams, Variable property effects on liquid droplet combustion, AIAA Journal, 6 (1968) 1961-1965.

[46] G.M. Faeth, R.S. Lazar, Fuel droplet burning rates in a combustion gas environment, AIAA Journal, 9 (1971) 2165-2171.

[47] R.S. Lazar, G.M. Faeth, Bipropellant droplet combustion in the vicinity of the critical point, Symposium (International) on Combustion, 13 (1971) 801-811.

[48] S. Kumagai, T. Sakai, S. Okajima, Combustion of free fuel droplets in a freely falling chamber, Symposium (International) on Combustion, 13 (1971) 779-785.

[49] J.W. Aldred, J.C. Patel, A. Williams, The mechanism of combustion of droplets and spheres of liquid n-heptane, Combustion and Flame, 17 (1971) 139-148.

[50] C.K. Law, Asymptotic theory for ignition and extinction in droplet burning, Combustion and Flame, 24 (1975) 89-98.

[51] C.K. Law, Multicomponent droplet combustion with rapid internal mixing, Combustion and Flame, 26 (1976) 219-233.

[52] C.K. Law, Unsteady droplet combustion with droplet heating, Combustion and Flame, 26 (1976) 17-22.

[53] C.K. Law, W.A. Sirignano, Unsteady droplet combustion with droplet heating—II: Conduction limit, Combustion and Flame, 28 (1977) 175-186.

[54] A. Crespo, A. LiÑAn, Unsteady Effects in Droplet Evaporation and Combustion, Combustion Science and Technology, 11 (1975) 9-18.

[55] C.K. Law, S. Prakash, W.A. Sirignano, Theory of convective, transient, multicomponent droplet vaporization, Symposium (International) on Combustion, 16 (1977) 605-617.

[56] J.C. Lasheras, A.C. Fernandez-Pello, F.L. Dryer, Initial Observations on the Free Droplet Combustion Characteristics of Water-In-Fuel Emulsions†, Combustion Science and Technology, 21 (1979) 1-14.

[57] J.C. Lasheras, A.C. Fernandez-Pello, F.L. Dryer, Experimental Observations on the Disruptive Combustion of Free Droplets of Multicomponent Fuels, Combustion Science and Technology, 22 (1980) 195-209.

[58] C.K. Law, C.H. Lee, N. Srinivasan, Combustion characteristics of water-in-oil emulsion droplets, Combustion and Flame, 37 (1980) 125-143.

[59] P. Botros, C.K. Law, W.A. Sirignano, Droplet Combustion in a Reactive Environment, Combustion Science and Technology, 21 (1980) 123-130.

[60] T. Saitoh, O. Nagano, Transient Combustion of a Fuel Droplet with Finite Rate of Chemical Reaction, Combustion Science and Technology, 22 (1980) 227-234.

[61] W.A. Sirignano, Fuel droplet vaporization and spray combustion theory, Progress in Energy and Combustion Science, 9 (1983) 291-322.

[62] B. Abramzon, W.A. Sirignano, Droplet vaporization model for spray combustion calculations, International Journal of Heat and Mass Transfer, 32 (1989) 1605-1618.

[63] C.K. Law, Recent advances in droplet vaporization and combustion, Progress in Energy and Combustion Science, 8 (1982) 171-201.

[64] G.M. Faeth, CURRENT STATUS OF DROPLET AND LIQUID COMBUSTION A2 - CHIGIER, N.A, in: Energy and Combustion Science (Student Edition One), Pergamon, 1979, pp. 149-182.

[65] C.H. Wang, X.Q. Liu, C.K. Law, Combustion and microexplosion of freely falling multicomponent droplets, Combustion and Flame, 56 (1984) 175-197.

[66] C.T. Avedisian, J.C. Yang, C.H. Wang, On low-gravity droplet combustion, Proceedings of the Royal Society of London. A. Mathematical and Physical Sciences, 420 (1988) 183.

[67] B.D. Shaw, F.L. Dryer, F.A. Williams, J.B. Haggard, Sooting and disruption in spherically symmetrical combustion of decane droplets in air, Acta Astronautica, 17 (1988) 1195-1202.

[68] J.i. Sato, M. Tsue, M. Niwa, M. Kono, Effects of natural convection on high-pressure droplet combustion, Combustion and Flame, 82 (1990) 142-150.

[69] S.Y. Cho, R.A. Yetter, F.L. Dryer, Mathematical modelling of liquid droplet combustion in micro-gravity, Mathematical and Computer Modelling, 14 (1990) 790-794.

[70] M.Y. Choi, F.L. Dryer, J.B. Haggard Jr, M.H. Brace, Further observations of microgravity droplet combustion in the Nasa-Lewis drop tower facilities: A digital processing technique for droplet burning data, in: AIP Conference Proceedings, AIP, 1990, pp. 338-361.

[71] B. Knight, F.A. Williams, Observations on the burning of droplets in the absence of buoyancy, Combustion and Flame, 38 (1980) 111-119.

[72] M.Y. Choi, F.L. Dryer, J.B.J. Haggard, M.H. Brace, The Burning Behavior of Methanol Droplets in Humid Air, in: Eastern States Fall Technical Meeting of the Combustion Institute, Clearwater Beach, FL, December 1988, 1988.

[73] A. Makino, C.K. Law, On the controlling parameter in the gasification behavior of multicomponent droplets, Combustion and Flame, 73 (1988) 331-336.

[74] S.Y. Cho, M.Y. Choi, F.L. Dryer, Extinction of a free methanol droplet in microgravity, Symposium (International) on Combustion, 23 (1991) 1611-1617.

[75] J.C. Yang, G.S. Jackson, C.T. Avedisian, Combustion of unsupported methanol/dodecanol mixture droplets at low gravity, Symposium (International) on Combustion, 23 (1991) 1619-1625.

[76] M.Y. Choi, Droplet combustion characteristics under microgravity and normal-gravity conditions, in: Mechanical & Aerospace, Princeton University, NJ, USA, 1992.

[77] D.L. Dietrich, J.B. Haggard Jr, F.L. Dryer, V. Nayagam, B.D. Shaw, F.A. Williams, Droplet combustion experiments in spacelab, Symposium (International) on Combustion, 26 (1996) 1201-1207.

[78] A.J. Marchese, F.L. Dryer, R.O. Colantonio, V. Nayagam, Microgravity combustion of methanol and methanol/water droplets: Drop tower experiments and model predictions, Symposium (International) on Combustion, 26 (1996) 1209-1217.

[79] B.L. Zhang, J.M. Card, F.A. Williams, Application of rate-ratio asymptotics to the prediction of extinction for methanol droplet combustion, Combustion and Flame, 105 (1996) 267-290.

[80] B.L. Zhang, F.A. Williams, Effects of the Lewis number of water vapor on the combustion and extinction of methanol drops, Combustion and Flame, 112 (1998) 113-120.

[81] C. Chauveau, I. Gökalp, D. Segawa, T. Kadota, H. Enomoto, Effects of reduced gravity on methanol droplet combustion at high pressures, Proceedings of the Combustion Institute, 28 (2000) 1071-1077.

[82] J.B. Wei, B.D. Shaw, Reduced Gravity Combustion of Propanol Droplets in Oxygen-Inert Environments, Combustion Science and Technology, 181 (2009) 1480-1494.

[83] M.C. Hicks, V. Nayagam, F.A. Williams, Methanol droplet extinction in carbon-dioxide-enriched environments in microgravity, Combustion and Flame, 157 (2010) 1439-1445.

[84] B.D. Shaw, J.B. Wei, Influence of Gravity and Ambient Pressure on Combustion and Flammability of n-Heptane and 1-Propanol Droplets in Air-Diluent Environments, Combustion Science and Technology, 183 (2011) 969-983.

[85] T.I. Farouk, Y.C. Liu, A.J. Savas, C.T. Avedisian, F.L. Dryer, Sub-millimeter sized methyl butanoate droplet combustion: Microgravity experiments and detailed numerical modeling, Proceedings of the Combustion Institute, 34 (2013) 1609-1616.

[86] S. Nakaya, K. Fujishima, M. Tsue, M. Kono, D. Segawa, Effects of droplet diameter on instantaneous burning rate of isolated fuel droplets in argon-rich or carbon dioxide-rich ambiences under microgravity, Proceedings of the Combustion Institute, 34 (2013) 1601-1608.

[87] V. Nayagam, Activation energy asymptotics for methanol droplet extinction in microgravity, Combustion and Flame, 160 (2013) 2638-2640.

[88] D.L.D. Vedha Nayagam, Michael C. Hicks, Forman A. Williams, Methanol Droplet Combustion in Oxygen-Inert Environments in Microgravity, 8th US National Combustion Meeting, 2013, 2013 (2013).

[89] D.L. Dietrich, V. Nayagam, M.C. Hicks, P.V. Ferkul, F.L. Dryer, T. Farouk, B.D. Shaw, H.K. Suh, M.Y. Choi, Y. Liu, C.T. Avedisian, F.A. Williams, Droplet Combustion Experiments Aboard the International Space Station, Microgravity Sci. Technol., (2014) 1-12.

[90] Y.C. Liu, Y. Xu, M.C. Hicks, C.T. Avedisian, Comprehensive study of initial diameter effects and other observations on convection-free droplet combustion in the standard atmosphere for n-heptane, n-octane, and n-decane, Combustion and Flame, 171 (2016) 27-41.

[91] T.I. Farouk, Y. Xu, C.T. Avedisian, F.L. Dryer, Combustion characteristics of primary reference fuel (PRF) droplets: Single stage high temperature combustion to multistage "Cool Flame" behavior, Proceedings of the Combustion Institute, 36 (2017) 2585-2594.

[92] V. Nayagam, D.L. Dietrich, P.V. Ferkul, M.C. Hicks, F.A. Williams, Can cool flames support quasi-steady alkane droplet burning?, Combustion and Flame, 159 (2012) 3583-3588.

[93] V. Nayagam, D.L. Dietrich, M.C. Hicks, F.A. Williams, Cool-flame extinction during n-alkane droplet combustion in microgravity, Combustion and Flame, 162 (2015) 2140-2147.

[94] F.E. Alam, Y.C. Liu, C.T. Avedisian, F.L. Dryer, T.I. Farouk, n-Butanol droplet combustion: Numerical modeling and reduced gravity experiments, Proceedings of the Combustion Institute, 35 (2015) 1693-1700.

CHAPTER 2

ISOLATED SPHERO-SYMMETRIC DROPLET COMBUSTION MODEL UNDER MICROGRAVITY CONDITION

2.1 MATHEMATICAL FORMULATION

The transient, sphero-symmetric droplet combustion model simulating liquid phase droplet oxidizing in an infinite medium is thoroughly described in the following section in consultation with the previously published articles [1-3]. All the physical submodels those are considered in the isolated droplet combustion code is schematically illustrated in Fig. 2.1. Coupled mass, energy and species transport equations are simultaneously solved in both the phases liquid and gas phases. The governing equations and associated submodels are described in the forthcoming sections.

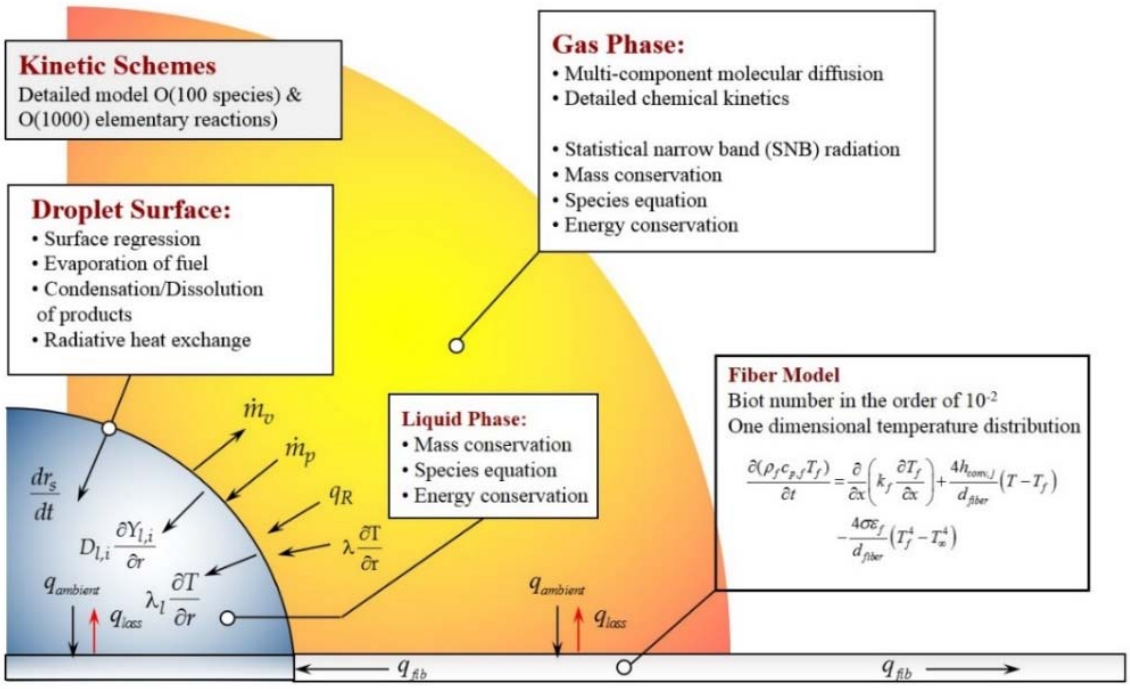

Figure 2.1 Schematic diagram of isolated sphero-symmetric one-dimensional droplet combustion model.

2.2 GAS PHASE CONSERVATION EQUATIONS

$$\frac{\partial \rho_g}{\partial t} + \frac{1}{r^2}\frac{\partial}{\partial r}\left(r^2 \rho_g v_g\right) = 0 \tag{1}$$

$$\rho_g \frac{\partial Y_{g,i}}{\partial t} + \rho_g v_g \frac{\partial Y_{g,i}}{\partial r} + \frac{1}{r^2}\frac{\partial}{\partial r}\left(r^2 \rho_g V_{r,i}\right) = \dot{\omega}_{g,i} \tag{2}$$

$$\rho_g C_{p,g} \frac{\partial T_g}{\partial t} + \rho_g C_{p,g} v_g \frac{\partial T_g}{\partial r}$$

$$= \frac{1}{r^2}\frac{\partial}{\partial r}\left\{ r^2 \lambda_g \frac{\partial T_g}{\partial r}\right\} - \rho_g \sum_{i=1}^{n}\left(Y_{g,i} V_{r,i} C_{p,g}\right)\frac{\partial T_g}{\partial r} \tag{3}$$

$$- \sum_{i=1}^{n} \dot{\omega}_{g,i} h_{g,i} - \nabla . q_R + S_{loss/gain,fiber}$$

Equation of state following ideal gas law

$$\rho_g = \frac{P}{R\, T_g}\left\{\sum_{i=1}^{n}\frac{Y_{g,i}}{W_i}\right\}^{-1} \tag{4}$$

Here, t = time, r = radial coordinate, ρ_g = mixture density, T_g = mixture temperature, $C_{p,g}$ = mixture heat capacity at constant pressure, λ_g = mixture thermal conductivity, v_g = radial fluid velocity, $V_{r,i}$ = diffusion fluid velocity of i-th species, $Y_{g,i}$ = mass fraction of i-th species, ω_i = mass production rate of i-th species, P = pressure and W_i = molecular weight of i-th species.

The parameter $S_{loss,\ fiber}$ is the loss and gain due to presence of tether fiber. As the fiber is present in a limited region only, the associated loss/gain term can be presented in terms of ratio of the fiber and domain volume, as expressed in the below expression

$$S_{loss\ /\ gain,fiber,} = \int_{r_-}^{r_+} \frac{4h_\infty n_f}{d_{fiber}}\left(T - T_f\right) r^2 \frac{A_{fiber} l_{fiber}}{V_{\frac{liquid}{gas}}}\, dr \tag{5}$$

$$A_{fiber} = \pi r_{fiber}^2 \; and \; V_{liq/gas} = \frac{4}{3}\pi r_{liq/gas}^3$$

Here, h_∞ is the convection coefficient, n_f = 1 (rod arrangement), 2 (single fiber arrangement) or 4 (cross-string arrangement), d_{fiber} is the diameter of the fiber, T_{fiber} is the fiber temperature, and T is the domain (liquid/gas) temperature. Depending on the value of (T-T_{fiber}), the fiber can act as a source ($T < T_{fiber}$) or sink ($T > T_{fiber}$).

2.3 LIQUID PHASE CONSERVATION EQUATIONS

$$\frac{\partial \rho_l}{\partial t} + \frac{1}{r^2}\frac{\partial}{\partial r}(r^2 \rho_l v_l) = 0 \tag{6}$$

$$\rho_l \frac{\partial Y_{l,i}}{\partial t} + \rho_l v_l \frac{\partial Y_{l,i}}{\partial r} - \frac{1}{r^2}\frac{\partial}{\partial r}\left(r^2 D_l \frac{\partial Y_{l,i}}{\partial r}\right) = 0 \tag{7}$$

$$\rho_l C_{P,l} \frac{\partial T_l}{\partial t} + \rho_l C_{P,l} v_l \frac{\partial T_l}{\partial r} = \frac{1}{r^2}\frac{\partial}{\partial r}\left(r^2 \lambda_l \frac{\partial T_l}{\partial r}\right) + S_{loss/gain,fiber} \tag{8}$$

$Y_{l,i}$ = liquid phase mass fraction; v_l = flow velocity; D_l = effective diffusion coefficient; ρ_l = mass density; h_l = constant pressure liquid enthalpy; T_l = temperature in liquid phase; λ_l = thermal conductivity.

2.4 BOUNDARY CONDITIONS

Zero gradient boundary condition is imposed in the droplet center.

$$\left.\frac{\partial Y_{l,i}}{\partial r}\right|_{r=0} = 0$$
$$\left.\frac{\partial T_l}{\partial r}\right|_{r=0} = 0 \tag{9}$$

And, in the far field i.e. r = ∞ (defined as 200 x r_d)

$$Y_{g,i}\big|_{r=\infty} = Y_{g,i,\infty}$$
$$T\big|_{r=\infty} = T_{ambient} \tag{10}$$

Here, $Y_{g,i,\infty}$ = mass fraction of i-th species in the ambient and T_∞ = ambient temperature.

In addition to the boundary conditions at r = 0 and r = ∞, the temperature continuity and conservation of mass and energy across the liquid-interface were imposed.

$$\left(T_g = T_l\right)\big|_{r=r_d} = T_s \tag{11}$$

$$\frac{dr_d}{dt} = \left(v_l - \left(v_g - v_l\right)\frac{\rho_g}{\rho_l}\right)\Big|_{r=r_d} \tag{12}$$

$$\left(D_l \frac{\partial Y_{l.i}}{\partial r} - \left(v_g - v_l\right)\frac{\rho_g}{\rho_l}\left(Y_{l,i} - \varepsilon_i\right)\right)\Big|_{r=r_d} = 0 \tag{13}$$

$$\left(\lambda_l \frac{\partial T_l}{\partial r} - \lambda_g \frac{\partial T_g}{\partial r} - \left\{\rho_g\left(v_g - v_l\right)\sum_{i=1}^{n_l} \epsilon_i L_i\right\} + q_R\right)\Big|_{r=r_d} = 0 \tag{14}$$

r_d is the instantaneous droplet radius, L_i is the latent heat of the i-th species in the liquid phase, and ε_i is the fractional gasification rate of the i-th species in the liquid phase, as defined

$$\varepsilon_i = \frac{\dot{m}_i}{\sum_{i=1}^{n_l} \dot{m}_l} \tag{15}$$

Here, $\dot{m}$ is the total gasification rate of the i-th species in the liquid phase, n_l is the number of species in the liquid phase.

2.5 ONE DIMENSIONAL FIBER ENERGY MODEL

Fiber supported droplets experience heat feedback through the support fiber by conduction heat transfer [4]. The present model accounts this additional heat transfer effect

considering a one dimensional (1D) heat conduction model . The fiber diameters (d_{fiber}) are typically < 100 μm for ISS [5] and drop tower [6] experiments. The associated Biot (Bi) number is on the order of 10^{-2} [3] and the application of 1D heat flow formulation is thus justified.

$$\frac{\partial\left(\rho_f C_{p,f} T_f\right)}{\partial t} = \frac{\partial}{\partial x}\left(k_f \frac{\partial T_f}{\partial x}\right) + \frac{4h_\infty}{d_{fiber}}\left(T_\infty - T_f\right) \tag{16}$$

In the above equation, ρ_f is the fiber density, $C_{p,f}$ is the fiber specific heat, k_f is the thermal conductivity, T_f is the fiber temperature, h_∞ is the convection coefficient, and d_{fiber} is the fiber diameter. In computing the convection coefficient, the fiber is assumed as horizontally placed cylinder, and $Nu_\infty = 0.36$ for the stagnant case [7]. In addition, other established Nusselt number correlations has been adopted [8, 9] and the overall droplet burning characteristics (burning rate, extinction diameter, and extinction time) were found to be sensitive less than 1% [3].

2.6 TRANSPORT AND RADIATIVE EFFECTS

The gas phase diffusion and the heat conduction terms in equations (2) and (3) were evaluated using multicomponent formulation proposed by Kee et al. (1986) using their Fortran based transport library TRANLIB [10]. Temperature dependent liquid phase data of pure component were taken from the compilation of Daubert & Danner [11].

To consider the radiative heat transfer effect, the liquid droplet and the infinity can be modeled as two concentric spheres, originally formulated by Viskanta and Merriam [12] assuming these two spheres are separated by a radiating and absorbing medium. The original formulation of Viskanta and Merrium (1968) was developed for steady-state condition. Within the droplet combustion code framework, Marchesee et al. [1] first

considered 'non-luminous' thermal radiation (NLTR) and demonstrated significant prediction improvements for large diameter (D_o > 1 mm) methanol/methanol-water droplets. In the NLTH model, these authors and then later Kazakov et al. [2] considered radially varied Plank-mean coefficient (κ_p).

Following these works, the radiation sub-model is further updated through the thesis work of Kenneth Kroenlein [13] to include computationally more efficient statistical narrow band (SNB) formulation. The implemented radiation model initially originates from the work of Lasic and Oinas [14] who developed a new category of SNB correlated-k (SNB-CK) model. In this model, the authors reordered the absorption coefficients in the line-by-line (LBL) method into a monotonic k-distribution in a narrow spectral range producing exact results with lower computational cost [15]. This yields better predictability over Curtis-Godson correlation. In addition, the SNB-CK model allow the implementation of discrete ordinate method (DOM) [16]. However, the shortcomings of this model is that it is numerically iterative, and occasionally convergence is not guaranteed. To circumvent this situation for multi-component gas mixture, Chen et al. [17] proposed a fitted SNB-CK model and validated their proposed model against spherically evolving flames at higher pressure. In this fitted SNB-CK model, the gas transmissivity (τ_υ) at a wave number υ over a light path L is given as-

$$\tau_\upsilon = exp\left[-\pi b\left(\sqrt{1+\frac{4SL}{\pi b}}-1\right)/2\right] \qquad (17)$$

Here, $b = 2\beta_\upsilon/\pi$, $S = k_\upsilon X_P$, and $\beta_\upsilon = 2\pi\gamma_\upsilon\delta_\upsilon$ are the SNB model parameters for CO, CO_2 and H_2O. By systematically performed an inverse Laplace transformation, a

distribution function for the absorption coefficient at each narrow band can be developed as below [14]

$$f(k) = 0.5k^{3/2}(bS)^{1/2} * \ exp\left[0.25\pi b\left(1 - \frac{S}{k} - \frac{k}{S}\right)\right] \tag{18}$$

And the cumulative function of k-distribution became

$$g(k) = \frac{1}{2}\left[1 - erf\left(\sqrt{\frac{\pi bS}{4k}} - \sqrt{\frac{\pi bk}{4S}}\right)\right] + \frac{1}{2}\left[1 - erf\left(\sqrt{\frac{\pi bS}{4k}} - \sqrt{\frac{\pi bk}{4S}}\right)\right] e^{\pi b} \tag{19}$$

Assuming a Gauss type quadrature, the following expression is used to compute the average radiation intensity at each narrow band.

$$I_v = \sum_{i=1}^{N} \omega_i I_v[k_i(g_i)] \tag{20}$$

In this equation, N = Gaussian quadrature points, ω_i = weight function, and g_i = Gaussian point. In the above formulation, the term '$k_i(g_i)$' requires iterative scheme to solve and typically diverges. To resolve this issue, Chen et al. proposed replacing the '$k_{ii}/S(b)$' term by a fitted function $F_i(b)$. this fitted function covers all Gaussian points for CO, CO_2 and H_2O using the existing SNB database [18]. For a radiatively participating gas mixtures, the total S-parameter is calculated from optically thin and thick limits by employing-

$$S = S_{CO} + S_{CO_2} + S_{H_2O} \tag{21}$$

$$\frac{S^2}{b} = \frac{S_{CO}^2}{b_{CO}} + \frac{S_{CO_2}^2}{b_{CO_2}} + \frac{S_{CO_2}^2}{b_{H_2O}} \tag{22}$$

The governing equation for the spectral radiative transfer equation in spherical coordinates at each band in m-direction is-

$$\mu_m \frac{\partial I_{\nu m}}{\partial r} + \frac{2\mu_m I_{\nu m}}{r} + \frac{1}{r}\frac{\partial}{\partial \mu_m}\left[(1-\mu_m^2)\, I_{\nu m}\right] = -k_\nu I_{\nu m} - k_\nu I_{b\nu} \tag{23}$$

In the above equation, $\mu_m = Cos(\theta_m)$ for polar angle θ and I_b is the blackbody radiation intensity. Further details of the fitted SNB-CK radiation models can be found in reference [17].

2.7 BURNING RATE AND VARIATION OF LIQUID PHASE DENSITY

Following the imposed velocity boundary condition at the droplet surface, we can derive the instantaneous burning rate as-

$$K_b = -\frac{d}{dt}(d_d^2) = -8r_d\frac{d}{dt}(d_d) = -8r_p v_l|_{r=r_p} - 8r_p(v_g - v_l)\frac{\rho_g}{\rho_l}\Big|_{r=r_p} \tag{24}$$

$$= K_1 + K_2$$

where, K_1 describes the droplet size change due to variation in liquid-phase density and K_2 is actual liquid mass gasification rate.

$$K_1 = -\frac{8}{\rho_l r_d}\int_0^{r_d}\frac{\partial \rho_l(T_l, Y_{l,i})}{\partial t}dr$$

$$= -\frac{8}{\rho_l r_d}\left(\int_0^{r_d}\frac{\partial \rho_l}{\partial T_l}\frac{\partial T_l}{\partial t}dr + \sum_{i=1}^{n_l}\int_0^{r_d}\frac{\partial \rho_l}{\partial Y_{l,i}}\frac{\partial Y_{l,i}}{\partial t}dr\right) \tag{25}$$

$$K_2 = -8r_d(v_g - v_l)\frac{\rho_g}{\rho_l}\Big|_{r=r_d} \tag{26}$$

The contribution of K_1 to total burning rate, K_b is only discernible during the ignition and extinction/flame-out transients. Over the QSS burning period, its contribution diminishes to zero as previously shown by Kazakov et al. [2].

2.8 WATER DISSOLUTION EFFECT

There are distinct classes of fuels (e.g., methanol and ethanol) for which selective combustion generated products from the flame front (e.g., water, H_2O) can dissolve back in to the liquid droplet [19]. The solubility of water in fuel, active -OH group and fuel chain length and structure all together dictate the water dissolution effect. Therefore, for such fuels, the role of liquid phase mass-transport must be considered as this directly contributes to the water absorption phenomena and its subsequent effect on the quasi-steady state (QSS) and flame-extinction burning phase. The liquid mass Peclet number, as defined below, is used to characterize the effects of liquid-phase transport.

$$Pe_{l,m} = r_p \frac{\left|\frac{dr_p}{dt}\right|}{D_l} = \frac{1}{8}\frac{\left|\frac{d(d_p)^2}{dt}\right|}{D_l} = \frac{1}{8}\frac{K_b}{D_l} \tag{27}$$

A lower value of liquid mass Peclet number preferentially transfers the condensed water interior to the droplet resulting in higher water accumulation (referred as 'Well-mixed Limit'). To the contrary, for higher value of $Pe_{l,m}$, only a thin layer of absorbed water is formed at the droplet boundary without significant water accumulation (known as 'Diffusion Limit'). The droplet burning rate (K_b) is computed as part of the solution, thus the value of the $Pe_{l,m}$ is dictated primarily by the value of effective liquid diffusivity (D_l). In the model, only the value of D_l is empirically calculated [2, 19]. It should be emphasized that all other model variables are remained as detail as possible.

2.9 NUMERICAL METHODS

The complete set of coupled partial differential and algebraic equations are discretized first in space and then integrated in an automated fashion as a set of coupled

ordinary differential-algebraic equations in time. Spatial discretization is performed according to a node-centered finite volume scheme with a second-order accuracy. The gas-liquid interface demarcates the volume boundaries for which the inner zone represents the condensed phase liquid fuel and the outer zone represents the gas phase ambient and the far field. The discretized mass flux is represented on cell interfaces and not cell centers, in the manner traditionally referred to as a staggered grid to avoid oscillatory solutions. Numerical integration of the final set of discretized equations is performed using a fifth order backward difference formula and a variable time step utilizing a fully implicit multipoint interpolation. This method is appropriate for the large range of time scales and overcomes stability constraints imposed by a chemically reacting system and automatic time-step variation.

2.10 REFERENCES

[1] A.J. Marchese, F.L. Dryer, The Effect of Non-Luminous Thermal Radiation in Microgravity Droplet Combustion, Combustion Science and Technology, 124 (1997) 371-402.

[2] A. Kazakov, J. Conley, F.L. Dryer, Detailed modeling of an isolated, ethanol droplet combustion under microgravity conditions, Combustion and Flame, 134 (2003) 301-314.

[3] T. Farouk, F.L. Dryer, Microgravity droplet combustion: effect of tethering fiber on burning rate and flame structure, Combustion Theory and Modelling, 15 (2011) 487-515.

[4] D.L. Dietrich, J.B. Haggard, F.L. Dryer, V. Nayagam, B.D. Shaw, F.A. Williams, Droplet combustion experiments in spacelab, Symposium (International) on Combustion, 26 (1996) 1201-1207.

[5] D.L. Dietrich, V. Nayagam, M.C. Hicks, P.V. Ferkul, F.L. Dryer, T. Farouk, B.D. Shaw, H.K. Suh, M.Y. Choi, Y. Liu, C.T. Avedisian, F.A. Williams, Droplet Combustion Experiments Aboard the International Space Station, Microgravity Sci. Technol., (2014) 1-12.

[6] F.E. Alam, Y.C. Liu, C.T. Avedisian, F.L. Dryer, T.I. Farouk, n-Butanol droplet combustion: Numerical modeling and reduced gravity experiments, Proceedings of the Combustion Institute, 35 (2015) 1693-1700.

[7] S.W. Churchill, H.H.S. Chu, Correlating equations for laminar and turbulent free convection from a horizontal cylinder, International Journal of Heat and Mass Transfer, 18 (1975) 1049-1053.

[8] G.E. Andrews, D. Bradley, G.F. Hundy, Hot wire anemometer calibration for measurements of small gas velocities, International Journal of Heat and Mass Transfer, 15 (1972) 1765-1786.

[9] D.C. Collis, M.J. Williams, Two-dimensional convection from heated wires at low Reynolds numbers, Journal of Fluid Mechanics, 6 (1959) 357-384.

[10] R.J. Kee, G. Dixon-Lewis, J. Warnatz, M.E. Coltrin, J.A. Miller, A Fortran computer code package for the evaluation of gas-phase multicomponent transport properties, Sandia National Laboratories Report SAND86-8246, 13 (1986) 80401-81887.

[11] T.E. Daubert, R.P. Danner, H. Sibul, C. Stebbins, Physical and thermodynamic properties of pure chemicals: data compilation, (1989).

[12] R. Viskanta, R.L. Merriam, Heat Transfer by Combined Conduction and Radiation Between Concentric Spheres Separated by Radiating Medium, Journal of Heat Transfer, 90 (1968) 248-255.

[13] K.G. Kroenlein, Numerical Simulation of Isolated Droplet Combustion Under Microgravity Conditions, in: Doctoral Thesis, Mechanical & Aerospace Engineering, Princeton University, NJ, USA, 2007.

[14] A.A. Lacis, V. Oinas, A description of the correlated k distribution method for modeling nongray gaseous absorption, thermal emission, and multiple scattering in vertically inhomogeneous atmospheres, Journal of Geophysical Research: Atmospheres, 96 (1991) 9027-9063.

[15] F. Liu, G.J. Smallwood, Ö.L. Gülder, Application of the statistical narrow-band correlated-k method to non-grey gas radiation in CO2–H2O mixtures: approximate

treatments of overlapping bands, Journal of Quantitative Spectroscopy and Radiative Transfer, 68 (2001) 401-417.

[16] W.A. Fiveland, Discrete Ordinate Methods for Radiative Heat Transfer in Isotropically and Anisotropically Scattering Media, Journal of Heat Transfer, 109 (1987) 809-812.

[17] Z. Chen, X. Qin, B. Xu, Y. Ju, F. Liu, Studies of radiation absorption on flame speed and flammability limit of CO2 diluted methane flames at elevated pressures, Proceedings of the Combustion Institute, 31 (2007) 2693-2700.

[18] A. Soufiani, J. Taine, High temperature gas radiative property parameters of statistical narrow-band model for H2O, CO2 and CO, and correlated-K model for H2O and CO2, International Journal of Heat and Mass Transfer, 40 (1997) 987-991.

[19] A.J. Marchese, F.L. Dryer, The effect of liquid mass transport on the combustion and extinction of bicomponent droplets of methanol and water, Combustion and Flame, 105 (1996) 104-122.

CHAPTER 3

EFFECTIVENESS OF XENON AS FIRE SUPPRESSANT UNDER MICROGRAVITY COMBUSTION ENVIRONMENT

3.1 ABSTRACT

The 'FLame EXtinguishment' (FLEX) program conducted by the National Aeronautics and Space Administration (NASA) onboard the International Space Station (ISS) has been assisting in developing fire-safety protocols for reduced gravity applications through microgravity droplet combustion experiments. A wide range of fuels including alcohols and alkanes have been studied under different ambient conditions encompassing the deployment of different diluents with compositional variation. A prime focus of this on-going research endeavor has been to assess the relative effectiveness of atmospheric composition and pressure changes on fire suppression under 'reduced' gravity conditions. This chapter compiles the results of detailed numerical simulations investigating the combustion and extinction characteristics of isolated sphero-symmetric methanol droplets burning in xenon (Xe) enriched environments. Subsequently, comparative analysis of diluent behaviors under identical conditions using argon (Ar), carbon dioxide (CO_2) and helium (He) as an alternative diluent choice to nitrogen (N_2) is also reported. The CFD predictions are compared against the ISS experiments with the good agreement and with less satisfactory agreement against the earlier results published by Shaw et al. [1]. It is found that xenon augmented ambient results in reduced burning rate, larger extinction diameter and counter-intuitively, prolonged burning time. The limiting oxygen index (LOI) for xenon is found be significantly lower than argon, carbon dioxide or helium. The numerical analyses also indicate that the lower thermal diffusivity of xenon is the principal factor responsible for the remarkably lower LOI. In addition, the

role of water accumulation within the methanol droplet and its relevance to the extinction process is also discussed. It is concluded that the combined observation of elevated peak gas temperature, exceptionally slow diffusive heat loss and the lower LOI value associated with xenon as a diluent all detract from its utility for suppressing fire concerns in reduced gravity applications.

3.2 INTRODUCTION

Combustion of sphero-symmetric isolated fuel droplets under quiescent conditions provides well-characterized opportunities to obtain fundamental data on the coupling of chemical kinetics and transport in diffusion-limited combustion. It also strengthens our understanding of elementary combustion properties such as burning rate, flame structure, extinction phenomena, and limiting oxygen index. Moreover, modeling aspect of isolated, spherically symmetric combustion configuration offers opportunities to include substantial detail in the sub-model components describing chemical kinetics, diffusive transport, and radiative interactions. A majority of the present fire safety knowledge encompasses situations in which changes in gas density caused by the heat generated from the combustion event results in natural convective effects. Evaluating the effects of diluent substitution on fire extinguishment and the effectiveness of different diluents as fire suppressants under low gravity applications where natural convective effects are absent is important to present and future space missions. Observing extinction phenomena under such conditions also helps us comprehending the role of specific finite-rate chemistry and diffusive/radiative interactions on extinction. Finally, combustion of spherically symmetric liquid fuel droplet offers a fundamental advantageous canonical

experimental venue to generate data for developing/testing the relevant sub-model components, their simplification and relative significance toward an accurate description of the coupled physical-chemical processes governing liquid fuel utilization [2].

For a systematic analysis of different limiting cases, methanol (CH_3OH) has frequently been a fuel of choice because of its non-sooting combustion behavior; however, the hygroscopic nature of this smallest alcohol introduces additional physical complexities [3, 4]. Choi et al. [3] were first to denote the non-linear d^2 –law behavior for methanol droplets burning in air and attributed this behavior to the dissolution of combustion products especially water from the gas phase into the liquid droplet. Choi et al. [5] and Lee & Law [6] measured the absorbed product during methanol droplet combustion for both free falling and suspended droplets. Their measurements confirmed that substantial amount of water is absorbed over the droplet combustion lifetime. In a following numerical work, Marchese and Dryer [7] highlighted the role of liquid phase internal circulation/motion on the water absorption phenomena and showed that the liquid phase within the droplet needed to be assumed as well mixed in order to achieve the agreement of predictions and experimental measurements. Dwyer et al. [8] in their multidimensional numerical work showed that water dissolution in methanol droplets introduces significant surface-tension-driven liquid motions. All these earlier works suggested that the extinction process of smaller sized methanol droplets were governed by water dissolution and subsequent gasification effects. Interestingly, compared to methanol, ethanol is less affected by water dissolution due to its azeotropic properties [9].

Cho et al. [10] conducted combustion experiments with methanol droplets in $He-O_2$ mixtures to determine extinction diameters. The highly conductive $He-O_2$ environment

facilitates higher burning rates that promote extinction in short duration. In an independent study with methanol/dodecanol droplets, it was shown that pure methanol droplets burning in air exhibited extinction at a non-zero droplet diameter [11]. Chaveau and coworkers [12], studied methanol droplet combustion at higher pressure and concluded that the d^2 law holds true for all ambient pressure up to 1.4 times that of the critical pressure for pure methanol. They also confirmed that the burning rate constant varied as $Gr^{1/4}$. However, their experimental burn time never extended to the extinction conditions, where non-linearity in d^2 behavior is prevalent. Further analysis of water absorption and dissolution in methanol droplet combustion revealed that water-dissolution driven extinction becomes less important at higher pressure [13]. Marchese et al. [14] showed that for methanol droplets burning in air, the radiative heat loss becomes increasingly important with initial droplet sizes greater than 1 mm, leading eventually to radiative extinction at sufficiently large diameters. Marchese's work also highlighted that a wide range of gas-phase Lewis numbers (Le) exist for the different species within the flame structure, contrary to assumptions typically applied in asymptotic analyses [15, 16]. In an independent study [17], a number of microgravity drop tower experiments were conducted and analyzed to study the effects of CO_2 enriched environments. Though CO_2 is a radiatively participating diluent, studies concluded that moderate-sized droplets underwent diffusive extinction with little influence of the changes in radiative transport.

Methanol droplet combustion has been studied numerically in the past [16, 18-22]. Despite this long-standing history, studies pertaining to diluent exchange and effect of diluents on fire suppression behavior from droplet combustion perspective have been relatively few [4, 21, 23-25]. The present work substantially advances the study of

isolated droplet combustion specifically in xenon-enriched diluent environments over earlier works [1, 26], by considering space-based, larger diameter experiments and computational models that encompass detailed chemistry, multi-component diffusion, and comprehensive radiative coupling. New simulation results on the effect of xenon on isolated methanol droplet combustion under microgravity conditions are reported based upon an evolutionarily developed one-dimensional sphero-symmetric transient combustion model as described in chapter 2 and references therein [4, 9, 14, 21, 27, 28]. The model predictions are first compared against the recent experiments conducted onboard the ISS. Subsequently, numerical predictions of droplet regression, peak gas phase temperature and flame stand-off ratio (FSR) with varying O_2 (i.e., Xe) mole fraction for different initial diameter are presented. Average burning rate ($K_{o,avg}$), average flame stand-off ratio (FSR_{avg}) and normalized extinction (D_{ext}/D_o) diameter data as a function of O_2 mole fraction are evaluated to determine the limiting oxygen index (LOI). The computational analyses also highlight the influence of argon, carbon dioxide and helium on the combustion characteristics (especially LOI) in order to assess the diluent effects found with xenon. Finally, analyses are presented concerning methanol droplet water dissolution effects resulting from diluent modifications.

3.3 RESULTS AND DISCUSSION

Numerical simulations of isolated methanol droplet combustion are performed for three different initial diameters, D_o = 1.0, 1.5 and 2.0 mm covering a broad range of xenon mole fraction in the ambient with the Xe/O_2 volumetric ratio systematically varied. Similar computations are also conducted for argon, carbon dioxide, and helium diluents.

The detailed methanol oxidation mechanism of Li et al. [29] consisting of 21 species undergoing 93 elementary reactions with the hydrogen oxidation sub-model update of Burke et al. [30] is employed for this study. The liquid phase properties of methanol are evaluated using the data correlations from Daubert and Danner [31]. All results presented here are obtained using a total of 220 spatial grid points; 70 grids points in the liquid domain and 150 in the gas phase (shown to yield a grid-independent solution).

3.3.1 MODEL VALIDATION

The present numerical study is undertaken principally to analyze the recently conducted experiments onboard ISS under Flame Extinguishment (FLEX) program. The details of the experimental procedures in performing tests, including data collection and reduction methodologies can be found in Dietrich et al. [32]. No additional data processing for the experimental data is performed as part of the current work. From the ISS FLEX test matrix, 'FLEX 563' is judiciously chosen for model validation and detailed analysis purpose, since this test used the maximum xenon displacement of nitrogen as diluent (D_o = 2.771 mm, X_{O2} = 8%, X_{Xe} = 63% /balance N_2). Figure 3.1 compares the predicted droplet diameter regression, flame stand-off ratio and flame diameter evolution against the ISS experimental data for identical conditions. The simulation results agree well with the measurements [$RMSE_{flame,dia}$ = 3.08 mm (Low light level ultraviolet camera), 2.87 mm (Color Camera); $RMSE_{FSR}$ = 1.32 (Low light level ultraviolet camera), 1.29 (Color Camera)]. The model captures the non-linearity observed in the experimental droplet regression data (Figure 3.1 (a)). The vertical line passing through all three subplots indicates the location of flame extinction (t ~ 4.90 s).

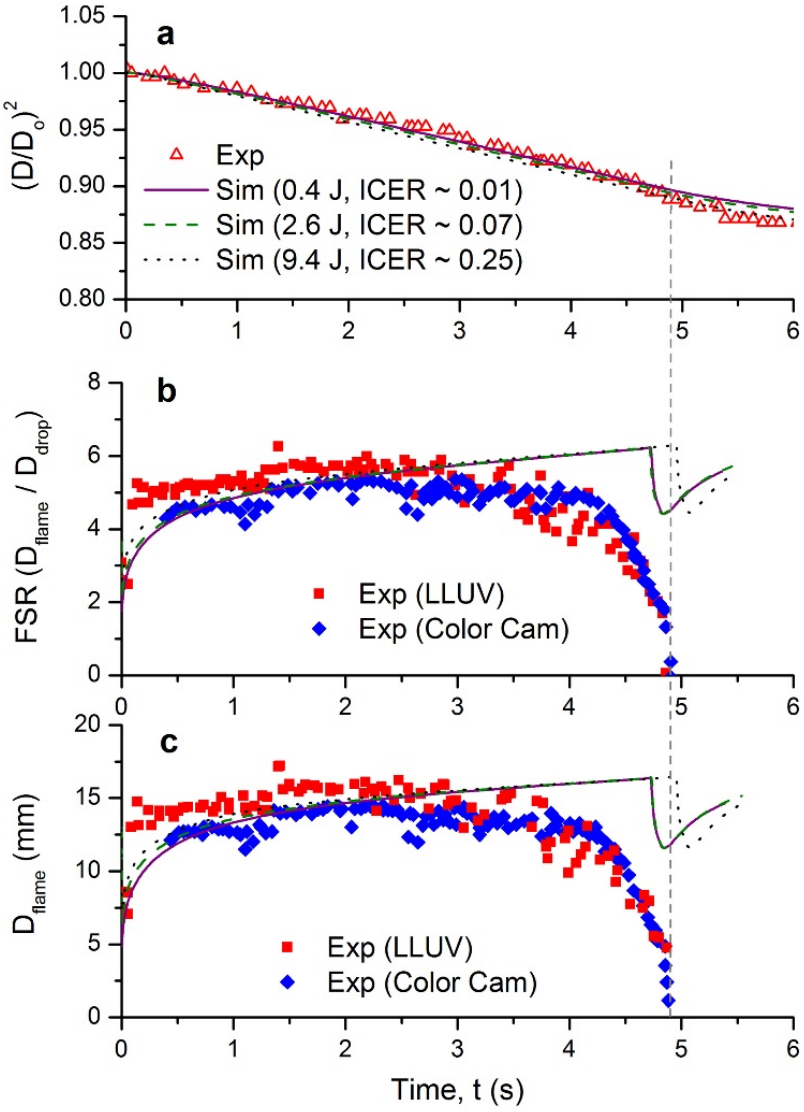

Figure 3.1 Comparison of numerical prediction and experimental data of (a) droplet diameter regression, (b) flame stand-off ratio, and (c) flame diameter for methanol droplet combustion (D_o = 2.771 mm, X_{O2}=8%, X_{Xe}=63% / balance N_2) at 1 atm pressure (ISS FLEX 563 test). Influence of variable ignition to chemical energy ratio (ICER) appears in subplot (a).

While the droplet diameter regression predictions are in good agreement, the flame stand-off ratio and flame diameter temporal evolution predictions deviate during the initial stage of burning as well as towards the end of the burn time as droplet extinction is approached; t > 3.5 s (Figure 3.1 (b) and 3.1 (c)). However, deviations in the flame evolution predictions and experimental data during the quasi-steady burn phase are

minimal. The scatter in the experimental data reflects the larger uncertainties associated with the flame diameter determination procedure. These discrepancies arise from the nature of the measurements as well as the methods utilized to extract the flame position. No natural convective effects or significant droplet drift are observed in the selected experiment. Furthermore, the role of natural convection is confirmed to be negligible through analyses considering maximum flame temperatures between 1000 K and 2000 K and flame diameters based upon maximum temperature location [2].

The hot wire approach used to initiate the droplet combustion involves several uncharacterized issues - ignition energy magnitude and it's spatial deposition, dynamics, and symmetry which are difficult to prescribe computationally [32]. The total ignition energy appears to be a key factor influencing droplet combustion behavior, though no accurate experimental characterization is readily available. Thus, numerical predictions based upon three different levels of total ignition energy, all deposited in similar sphero-symmetric spatial distributions about the initial droplet, are performed to parametrically evaluate its effect. Three ignition-to-combustion energy ratios (0.01, 0.07 and 0.25) were compared. Ignition energies of these magnitudes are observed to affect only the initial transient burning observations (Figure 3.1). For an ignition energy lower than 0.4 J, quasi-steady burning could not be established, as also found in an earlier analysis [33] for similar droplet initial diameter. Model predictions are also compared with the data reported by Shaw et al. [1], and results are shown in the supplementary Figure 3.11.

3.3.2 ROLE OF INITIAL DIAMETER AND XENON CONTENT

The effects of initial droplet diameter and ambient xenon displacement on the predicted temporal profiles of droplet diameter regression, peak gas temperature and flame stand-off ratio (FSR) are presented in Figure 3.2. Though a wide range O_2/Xe ambiance and drop diameters are studied, for visual clarity, Figure 3.2 presents only the results for three O_2 molar fractions (0.21, 0.10 and 0.07) and two initial droplet diameters (1.0 mm and 2.0 mm). The droplet diameter regression rate decreases with an increase in ambient xenon mole fraction (i.e. decreasing O_2) for a given droplet diameter, resulting in a lower burning rate (K_o), and diminished peak gas temperature (Figure 3.2 (c) and (d)). Increased xenon displacement reduces the average thermal conductivity (k) and increases specific heat capacity (C_p), hence decreasing thermal diffusivity (α) of the surrounding gas mixture. For the larger diameter case, increasing xenon content results in a decrease in regression rate, an increase in extinction diameter, and a longer burning time. Even at the highest xenon concentration, a quasi-steady burning phase was attainable. In comparison, smaller droplets having identical ambient conditions to the larger diameter cases burned at a faster rate due to lower heat loss and consequentially produced smaller extinction diameters. Unlike the results for other diluents (helium, carbon dioxide), at increased loading condition (i.e. low oxygen concentration), higher xenon displacements promote rather than degrade quasi-steady combustion [4].

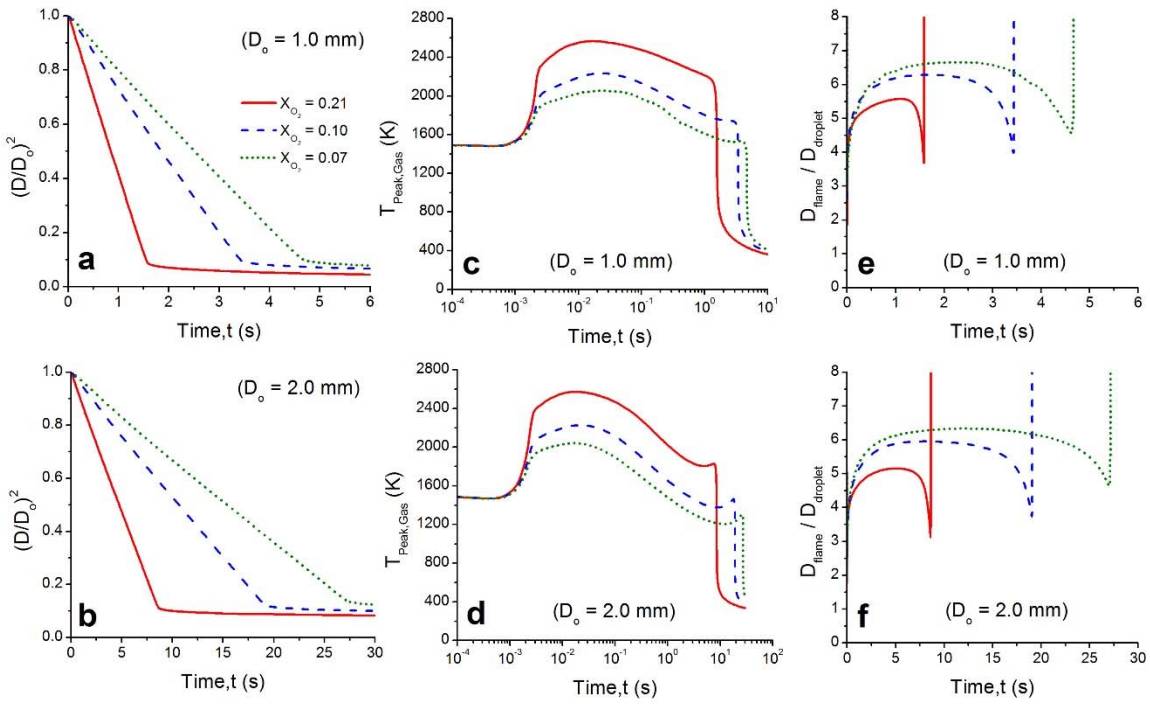

Figure 3.2 Numerical prediction of droplet diameter regression (subplot (a) and (b)), peak gas temperature (subplot (c) and (d)) and flame stand-off ratio, FSR (subplot (e) and (f)) for different initial methanol droplet diameters in varying O_2/Xe ambience (1 atm, 298 K). Top row D_o = 1 mm, bottom row D_o = 2 mm.

The temporal evolution of the peak gas temperature as a function of xenon concentration for the same three exemplary cases is presented in Figure 3.2 ((c) and (d)). An increase in xenon content decreases both the maximum value of the peak gas temperature and the maximum rate of increase of the peak gas temperature (dT_{max}/dt). It is found that the lower thermal conductivity and higher heat capacity of xenon are the causes of the observed changes in early-stage temperature evolution (c.f. Table 3.1). For the same ambient condition, lower peak temperatures occur with increased initial diameter, primarily as a result of radiative heat loss. For instance, at t ~1 s for 21% O_2, 1 mm droplet exhibits a peak temperature of 2212 K while the 2 mm droplet yields 2020 K, a difference of ~ 190 K. As depicted in Figure 3.2 (subplots (e) and (f)), the flame stand-

off ratio (FSR) is found to be weakly dependent on the initial droplet sizes studied and strongly dependent on ambient gas composition. Illustratively, for 21% O_2/79% Xe composition, the FSR during the quasi-steady burn period was found to be ~ 5.0 for D_o = 2.0 mm which then increased to ~5.5 for D_o = 1.0 mm. However, when xenon mole fraction is raised to 93% from 79% (D_o = 2.0 mm), the FSR escalates to ~ 6.4. In microgravity liquid droplet combustion, the flame relocates itself in the region where the fuel and oxidizer are in the stoichiometric condition. Increasing dilution results in a larger radial distance where the stoichiometry condition for fuel-oxidizer mixture occurs, and hence a larger FSR.

Table 3.1 Transport and thermodynamic properties of the different diluent gases (Properties are evaluated at T = 300 K and 700 K, P = 1 atm). Data are from [31].

Diluent Gas	**Molecular Weight, M_w, (kg/kmol)**	**Thermal Conductivity, k (W/m-K)**	**Specific Heat, C_p (J/Kg-K)**	**Density, ρ (Kg/m^3)**	**Thermal Diffusivity, α (m^2/s)**
Temperature 300 K					
He	4.0026	0.1560	5196.52	0.1604	1.8712×10^{-04}
CO_2	44.0095	0.0168	845.45	1.7730	1.1108×10^{-05}
Ar	39.9480	0.0177	634.72	1.6025	2.1195×10^{-05}
Xe	131.2930	0.0056	158.31	5.2903	6.5750×10^{-06}
Temperature 700 K					
He	4.0026	0.2811	5192.87	0.0688	7.8711×10^{-04}
CO_2	44.0095	0.0493	1126.87	0.7562	5.7851×10^{-05}
Ar	39.9480	0.0334	520.50	0.6862	9.5074×10^{-05}
Xe	131.2930	0.0116	158.51	2.2562	3.2559×10^{-05}

3.3.3 AVERAGE BURNING PARAMETERS IN XENON RICHED AMBIENT

The average burning rate ($K_{o,avg}$), average flame stand-off ratio (FSR_{avg}) and normalized extinction diameter (D_{ext}/D_o) as a function of ambient oxygen content (X_{O2}) for initial droplet diameters of 1.0, 1.5 and 2.0 mm are presented in Figure 3.3. The average quantities are obtained by time-averaging the instantaneous values (K_o and FSR) between $t = 0.1 * t_b$ and $t = 0.95 * t_b$, where t_b is the total burn time. We define the total burn time (t_b) as the time difference between ignition and extinction/flame-out and exclude the vaporization phase after extinction. It can be seen in Figure 3.3 (a) that an increase in the ambient xenon content (i.e., decrease in oxygen) reduces $K_{o,avg}$. The presence of xenon reduces the thermal diffusivity of the ambient gas significantly, as evidently shown in Table 3.1. As a consequence, the energy feedback to the droplet surface from the flame zone diminishes, resulting in lower burning rate. For smaller droplet, $K_{o,avg}$ varies almost linearly as a function of ambient xenon concentration. As D_o becomes larger a non-linearity is observed at higher xenon content due to an emerging dominance of increasing heat losses at the oxygen-deprived condition. The non-linearity at low oxygen concentration indicates radiative heat losses under such conditions [34].

The variation of the average flame stand-off ratio (FSR_{avg}) as a function of ambient oxygen concentration (i.e. increasing xenon concentration) for the same three different initial droplet diameters are depicted in Figure 3.3b. The FSR_{avg} initially increases with decreasing oxygen content, reaching a peak beyond which it starts to fall drastically. This sharp decline in FSR_{avg} is primarily due to the inability to sustain a quasi-steady burning at reduced oxygen environment which initiates the flame to relocate itself very close to the droplet surface to compensate the net heat loss of the system. The oxygen content for

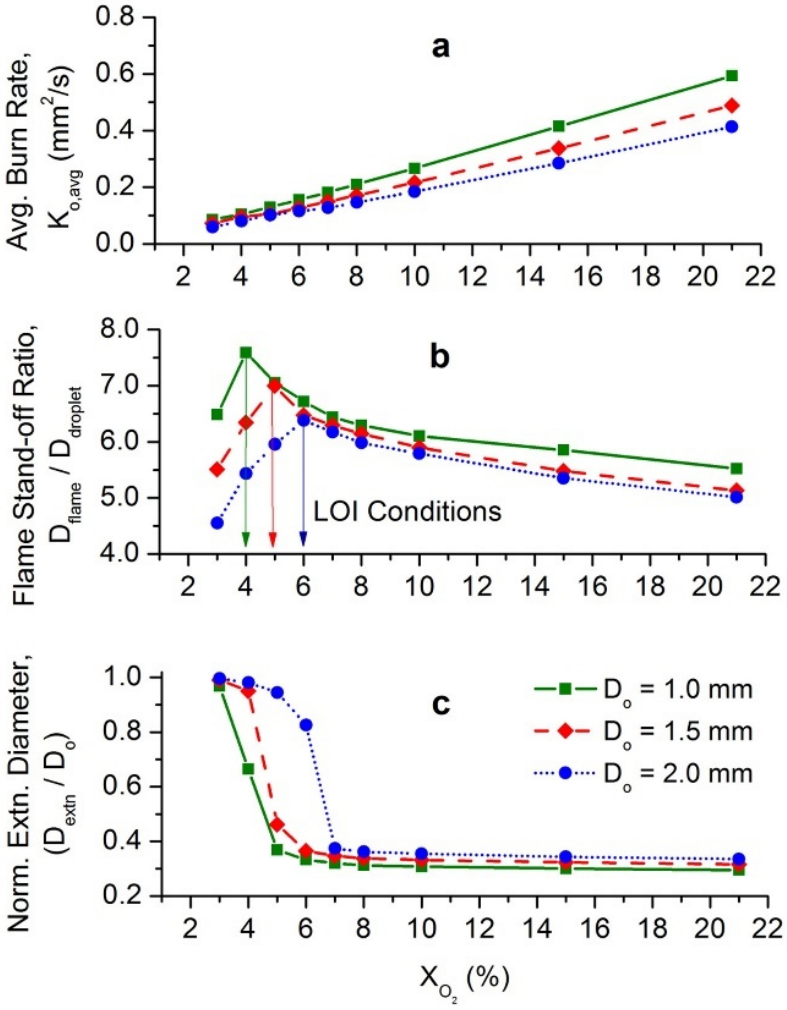

Figure 3.3 Numerical prediction of (a) average burning rate, $K_{o,avg}$ (b) average flame stand-off ratio, FSR_{avg}, and (c) normalized extinction diameter (D_{ext}/D_o) for different initial diameter methanol droplets under varying O_2/Xe ambient (1 atm, 298 K).

which the maximum FSR_{avg} occurs defines the limiting oxygen index (LOI), as further decreases in the oxygen concentrations yield to unsustainable (quasi-steady) combustion behavior. Furthermore, at a fixed O_2 concentration, larger droplets yield reduced FSR_{avg} values as a consequence of the increase in heat loss. Hence, the LOI for different initial droplet diameter is observed to increase as the initial droplet diameter is increased. The LOI for D_o values of 1.0 mm, 1.5 mm and 2.0 mm were found to be ~ 4%, 5%, and 6%, respectively. This trend is evident in the normalized extinction diameter results presented

in Figure 3.3 (c). As the LOI condition is attained, the extinction diameter increases sharply for each of the respective cases. In contrast to the LOI results found for nitrogen (e.g., 11% for D_o = 1.5 mm at 1 atm [4]), the LOI for xenon under the similar ambient condition is reduced by a factor of 2.2.

3.3.4 COMPARATIVE ANALYSIS AMONG DIFFERENT DILUENTS

In order to assess the effectiveness of xenon as a diluent candidate to improve fire safety criteria under microgravity conditions, the combustion characteristics of xenon-enriched ambient are compared with those against helium (He), carbon dioxide (CO_2) and argon (Ar) augmented atmospheres and the comparison is illustrated in Figure 3.4. The simulation results presented in this figure are for D_o = 1.5 mm, X_{O2} = 21% and balance diluent. Helium is found to produce the maximum burning rate, largest extinction diameter, and shortest burn time. The higher thermal diffusivity (c.f. Table 3.1) of helium leads to increased heat transfer to both the droplet surface as well as to the far-field (i.e., a thicker flame structure). The heat feedback to the surface increases the droplet burning rate while the losses to the far-field promote earlier flame extinction. Droplet combustion for the three remaining diluent cases all show relatively similar, lower burning rates and temporal locations for flame extinction are in close proximity to one another. Droplet burning in CO_2 has the lowest burning rate K_o (i.e. the slowest droplet diameter regression). The presence of high concentration of CO_2 in the ambient (in comparison to nitrogen) reduces the average thermal conductivity, increases the specific heat of the ambient mixture, and increases the heat capacity of the surrounding gas mixture. The overall result is decreased thermal diffusive losses. The radiative heat loss also increases

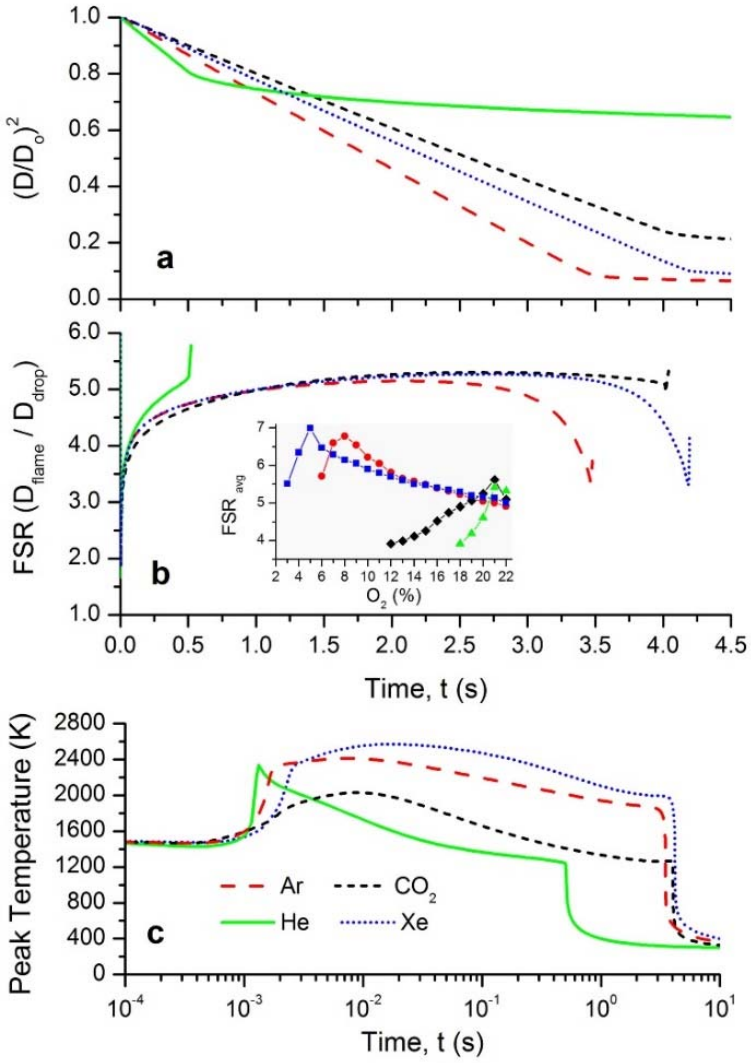

Figure 3.4 Computational comparison of the diluent effect on methanol droplet combustion: (a) droplet diameter regression, (b) flame stand-off ratio and (c) peak gas temperature. Subplot (b) Inset figure: average flame stand-off (FSR_{avg}) ratio for different diluents. (D_o = 1.5 mm, X_{O2} = 21%, balance diluent, ambient condition-1 atm, 298 K).

as CO_2 is a radiatively participating medium [21]. Droplet burning in CO_2 is found to have both the lowest flame temperature and the slowest rate of increase of the peak gas temperature $\left(\frac{dT_{max}}{dt}\right)$ (c.f. Figure 3.4 (c)). Both the lower thermal conductivity and the higher heat capacity of CO_2 contribute to the differences observed in the early stages of the temperature evolution with increasing CO_2 in the ambient. The decrease in $\left(\frac{dT_{max}}{dt}\right)$

also results in the shift of temporal location for peak gas temperature towards longer burning times, which is analogous to having a larger flame evolution time from the premixed state at ignition to diffusive controlled combustion. Presence of the CO_2 in the ambient significantly decreases the peak gas temperature within the diffusive flame zone, as well as the rate at which the peak flame temperature decreases over the quasi-steady burn.

The combustion characteristics of methanol droplet (burning rate & FSR evolution) in xenon enriched ambient lies between those found with carbon dioxide and argon. Xenon results in the longest period of time (Figure 3.4 (b)). From the fire safety viewpoint, it is expected that the more desirable diluent should promote rapid flame extinguishment. Thus, xenon underperforms in achieving this target ($t_{ext,Xe}$ / $t_{ext,CO2}$ / $t_{ext,Ar}$ ~ 4.275 s / 4.050 s / 3.375 s). Xenon as a diluent also results in the highest flame temperature (Figure 3.4 (c)), especially the during quasi-steady burning. In fact, xenon exhibits the smallest thermal diffusivity amongst the studied diluents by several factors (see, Table 3.1). In addition to this transport property, Xenon also has a low specific heat, the maximum flame temperature, and reduced diffusive losses, culminating in the lowest LOI compared to other diluents studied (Figure 3.4 (b)).

Since the FSR_{avg} has been used as a marker for the LOI, the variation of FSR_{avg} as a function of ambient oxygen concentration for the different diluents is presented in the inset of Figure 3.4 (b). The FSR_{avg} increases with decreasing oxygen concentration (i.e. increasing diluent concentration) to meet the stoichiometric condition at a further distance from the liquid fuel droplet surface. This increase in flame position occurs until the LOI condition is achieved. For the carbon dioxide and helium diluent cases, a limited

region of the increasing FSR_{avg} is observed. For oxygen concentrations lower than the LOI, the FSR_{avg} falls sharply as the flame development becomes fully transient (no quasi-steady burning is observed). In comparison to argon, the FSR_{avg} in xenon increases in small increments as a function of oxygen concentration. The slow variation is due to the fact that oxygen has the lowest mass diffusivity in xenon (e.g., at 1000 K, $D_{O2\text{-}Xe} = 1.032$ cm^2/s < $D_{O2\text{-}CO2} = 1.295$ cm^2/s < $D_{O2\text{-}Ar} = 1.578$ cm^2/s < $D_{O2\text{-}He} = 6.434$ cm^2/s). Consequently, xenon exhibits the lowest LOI, which is directly related to the limiting diffusive transport capabilities. For instance, LOI for D_o =1.5 mm was found to be 5%, 8%, 21% and 21% for xenon, argon, helium and carbon dioxide respectively. The combination of a very low LOI and longer burn times points to xenon being a poor choice as a 'fire suppressant' diluent under microgravity conditions.

The influence of the thermal transport properties on the combustion characteristics is further illustrated in Figure 3.5. The plots summarize the spatially varying temperature profile for two different conditions, X_{O2} (21%) / $X_{diluents}$ (79%) (t~0.01 s) and for X_{O2} (10%) / $X_{diluents}$ (90%) (t~0.03 s). The highest peak gas temperature with xenon is clearly discernible. These consistent higher temperature profiles for xenon are a direct consequence of its thermal diffusivity (Figure 3.5 (c)) which enables xenon ambient to accumulate substantial thermal energy. To the contrary, because of its excessively high thermal conductivity (viz. thermal diffusivity, α) helium demonstrates the opposite behavior. The consequence of the unique transport characteristics of xenon is further explored through diluent exchange simulations with nitrogen (N_2), reported in the supplementary Figure 3.12. These simulations are performed for D_o = 1.5 mm with varying N_2/Xe exchange ratio at fixed oxygen concentration (X_{O2} = 21%). Due to the

exceptionally low thermal diffusivity (α), the gas phase temperature is found to monotonically increase with the reductions in burning rate (K) and a more prolonged burn time as the volume fraction of xenon is increased.

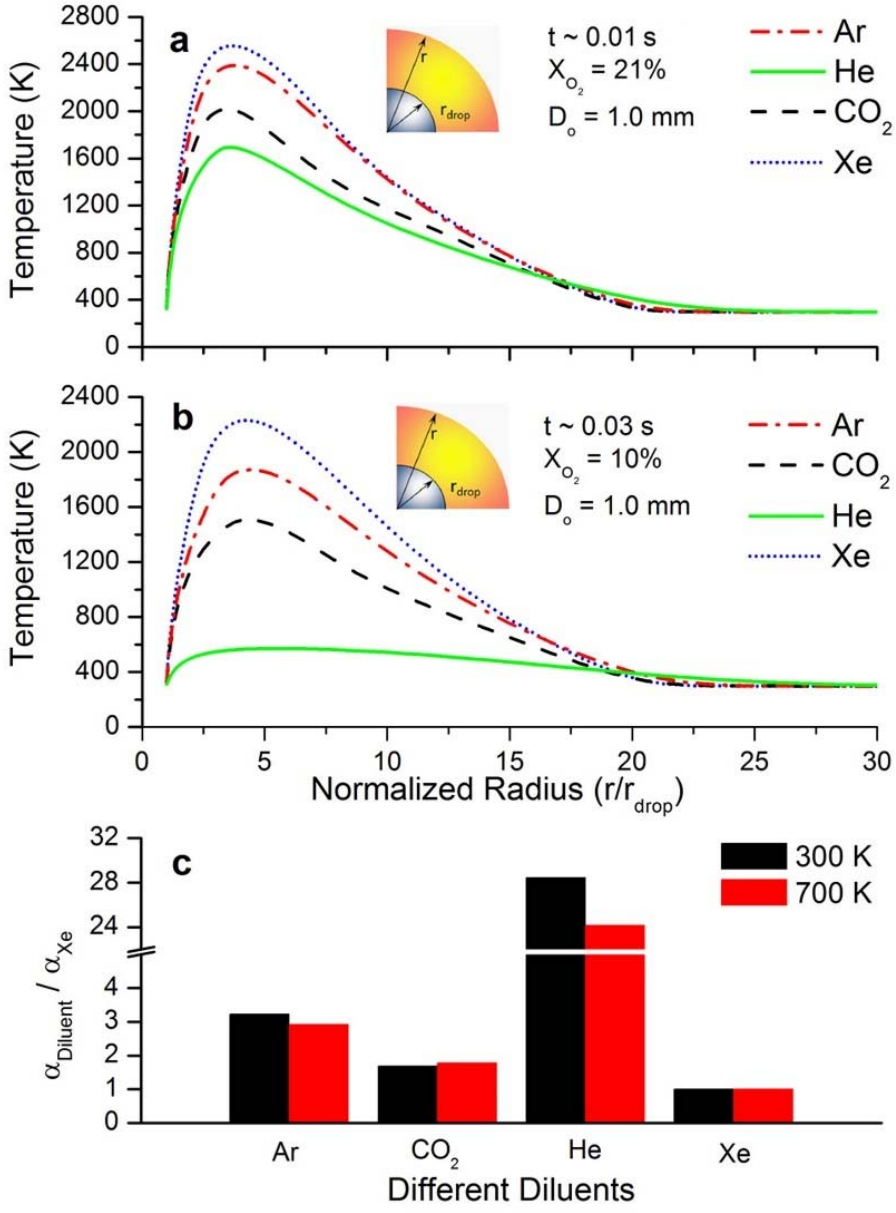

Figure 3.5 Predicted spatial distribution of gas temperature at different time instances for D_o = 1 mm, X_{O2} = 21% with balance amount of different diluents (a) time, t ~ 0.0105 s (b) time, t ~ 0.03 s (c) comparison of thermal diffusivity of different diluents at 300 K and 700 K.

3.3.5 THIRD BODY REACTION COLLISION FREQUENCY FOR XENON

The methanol chemical kinetic model used in this numerical study does not include the third body collision efficiency for xenon due to the lack of appropriate data in the literature. We assumed the third body collision efficiency to be identical that of argon. Figure 3.6 summarizes the sensitivity of the average burning rate at the respective LOI conditions for D_o = 1.0 mm, 1.5 mm and 2.0 mm to the xenon collision efficiency factor. Simulations were conducted for efficiency factors relative to argon of 0.5, 1, and 2. The predictions show that the average burning rates of the individual cases are insensitive to the variation in the collision efficiency factor.

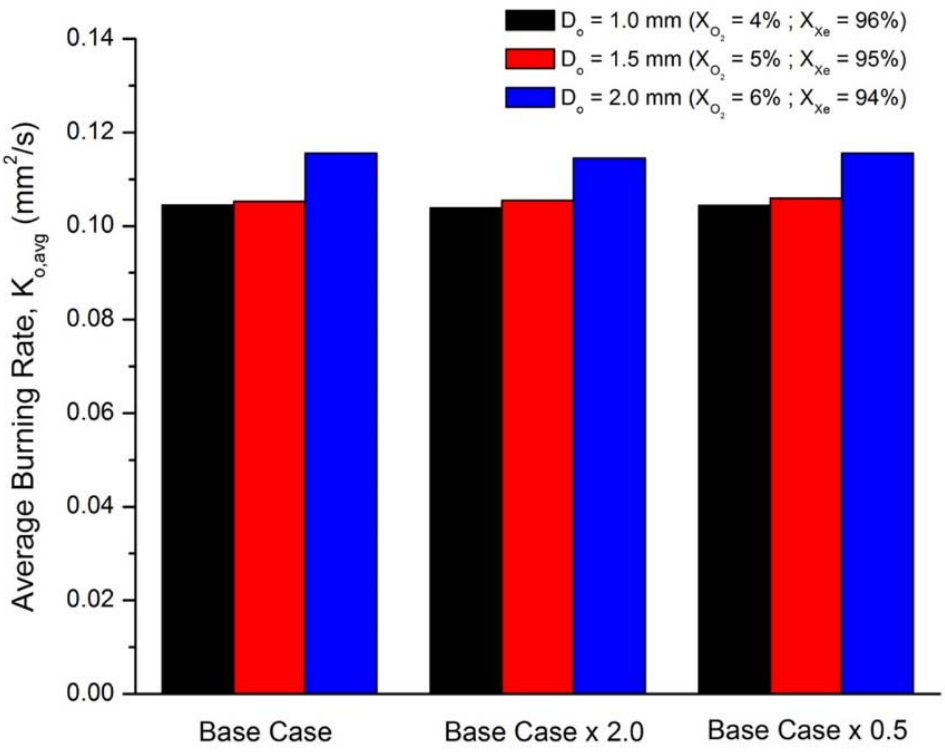

Figure 3.6 Sensitivity of third body collision efficiency of xenon on the average burning rate for different initial diameters at respective LOI conditions. D_o = 1.0 mm (X_{O2} = 4% ; X_{Xe} = 96%), D_o = 1.5 mm (X_{O2} = 5% ; X_{Xe} = 95%) and D_o = 2.0 mm (X_{O2} = 6% ; X_{Xe} = 94%).

3.3.6 LIQUID PHASE WATER DISSOLUTION UNDER DIFFERENT DILUENTS

Water absorption during methanol droplet combustion is a well-known phenomenon that results from their mutually infinite solubility [10]. Spatially integrated total water accumulation (at near extinction condition) inside a methanol droplet (D_o = 1.5 mm) with different diluents is illustrated in Figure 3.7. The binary diffusion coefficient of water in different diluents for a temperature range up to 1000 K is depicted as an inset in the figure. An increase in xenon concentration (viz. decrease in oxygen) results in an increase in overall water mass fraction until the LOI condition is achieved. However, the binary diffusion coefficient of water-in-xenon, $D_{H2O\text{-}Xe}$ [35], is lower than that of $D_{H2O\text{-}Ar}$ and $D_{H2O\text{-}CO2}$. Thus, it can be inferred that the longer burning time in xenon-enriched ambient enables the methanol droplet to absorb more water during the course of combustion compared to other diluents, despite the lower $D_{H2O\text{-}Xe}$ value. Water accumulation with argon as a diluent is similarly large. Contrary to the droplet extinction in carbon dioxide and helium ambient, extinction in xenon and argon can be related mainly to water dissolution that migrates from the flame front location (i.e. combustion generated water) to the liquid droplet [6, 7].

Subsequently, the aforementioned droplet cases are simulated again to replicate pure vaporization in various bath gas quiescent ambient for a 5 minute time considering 40% relative humidity. Detailed analysis of peak water mass fraction is illustrated in Figure 3.8. The ambient gas composition strongly influences the amount of water that is being absorbed during vaporization of the initially pure methanol droplet. It is found that methanol droplet evaporates completely in helium augmented ambient. To the contrary, significant fuel fraction remains in the condensed phase for other diluents with xenon

exhibiting highest resistance to water dissolution. These observations are consistent with the binary diffusion coefficients of a water-in-diluent trend for the various diluents (inset, Figure 3.7). The fact that xenon enriched conditions limit water absorption during the pre-ignition stage suggests that extinction diameters measured under such conditions are less likely to be perturbed by droplet growth and deployment procedures in humid atmospheres. This analysis clearly highlights that the droplet formation and deployment phase at the ISS test rig (before providing ignition source) can experience substantial water dissolution effects for methanol fuel prior to combustion.

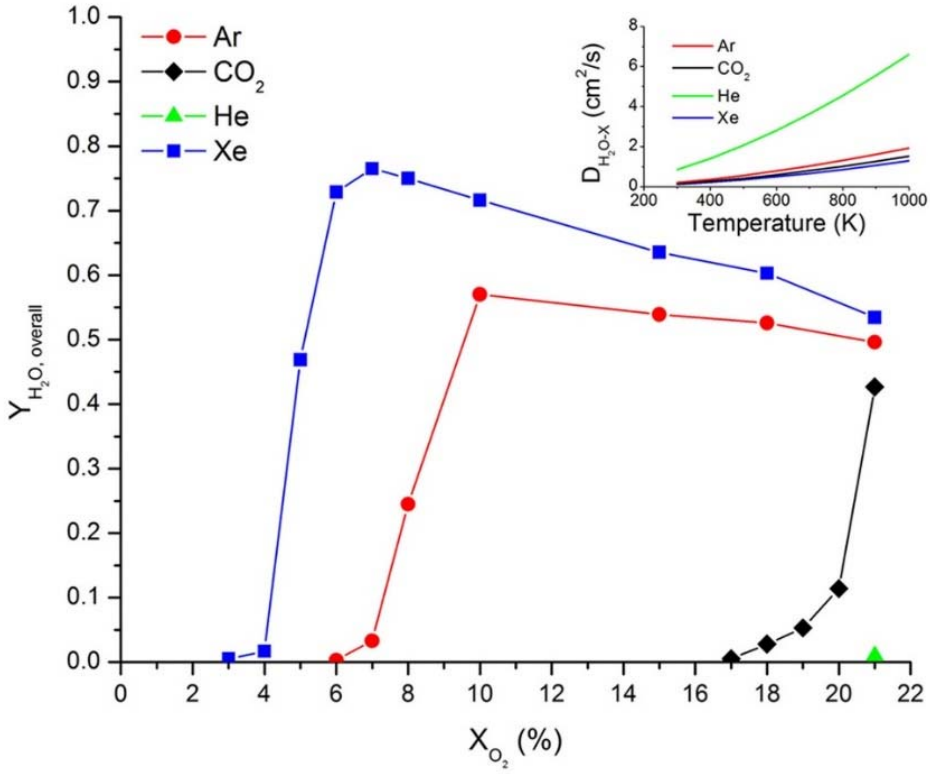

Figure 3.7 Predicted overall liquid phase water mass fraction (Y_{H2O}) at near extinction for varying O_2 concentration in different diluents. Initial droplet size, D_o = 1.5 mm. For helium, only X_{O2} = 21% case is shown. Inset figure: binary diffusion coefficient of water in different diluents up to 1000 K ambient temperature.

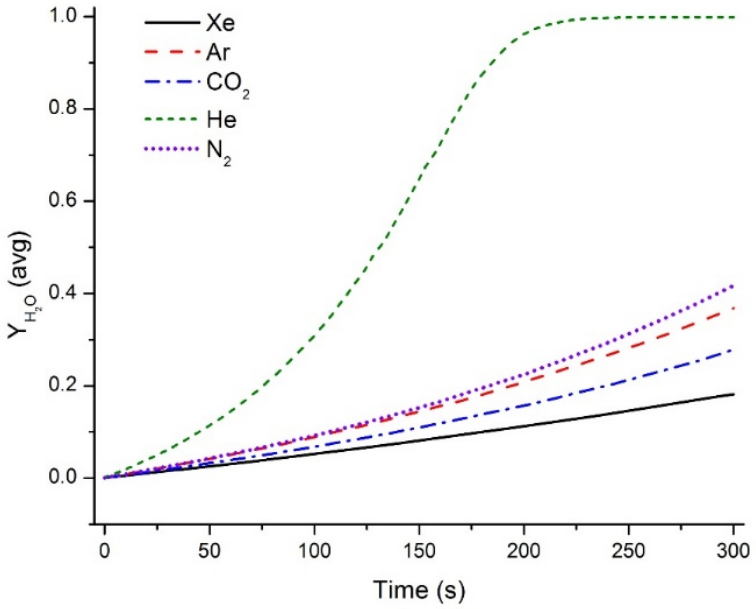

Figure 3.8 Vaporization study of methanol droplet under different diluent condition (D_o = 1.5 mm, X_{O2} = 21%, 1 atm, 298 K and 40 % relative humidity).

3.3.7 WATER MASS FRACTION DISTRIBUTION NEAR FLAME EXTINCTION POINT FOR DIFFERENT DILUENTS

Equally compelling to the previous time-dependent discourse, spatial variation of water mass fraction within the droplet, and that in the gas phase is also analyzed. It is stated earlier that the effect of water accumulation inside the droplet can significantly influence the extinction process. Figure 3.9 summarizes the gas phase water mass fraction distribution against normalized radius (r/r_{drop}) for four different diluents at different time snaps near the extinction process. The initial droplet diameter is 1.5 mm and the simulations are performed at ambient condition X_{O2} = 0.21 and $X_{Diluent}$ = 0.79. For the case of helium, the Y_{H2O} profile remains nearly the same as the droplet approaches extinction. Utilizing the FSR data presented in Figure 3.4 (b) and correlating those results with the time range investigated here, it is observed that the helium-filled ambient contains water as much as 22.5% (by mass) at the flame location near extinction.

Following the same treatment, the maximum estimation of water content near the point of extinction for CO_2, Ar and Xe is 11%, 14%, and 6% respectively. Additionally, the water concentration profile in argon and xenon showed an interesting slope reversal trend adjacent to the droplet surface as the droplet approaches extinction – instead of water being absorbed into the droplet, water from the droplet started to diffuse out from the droplet into the gas phase. These interesting observations suggest that not only the water absorption but also its subsequent gasification are important attributes of methanol droplet extinction in argon and xenon bath gases [36].

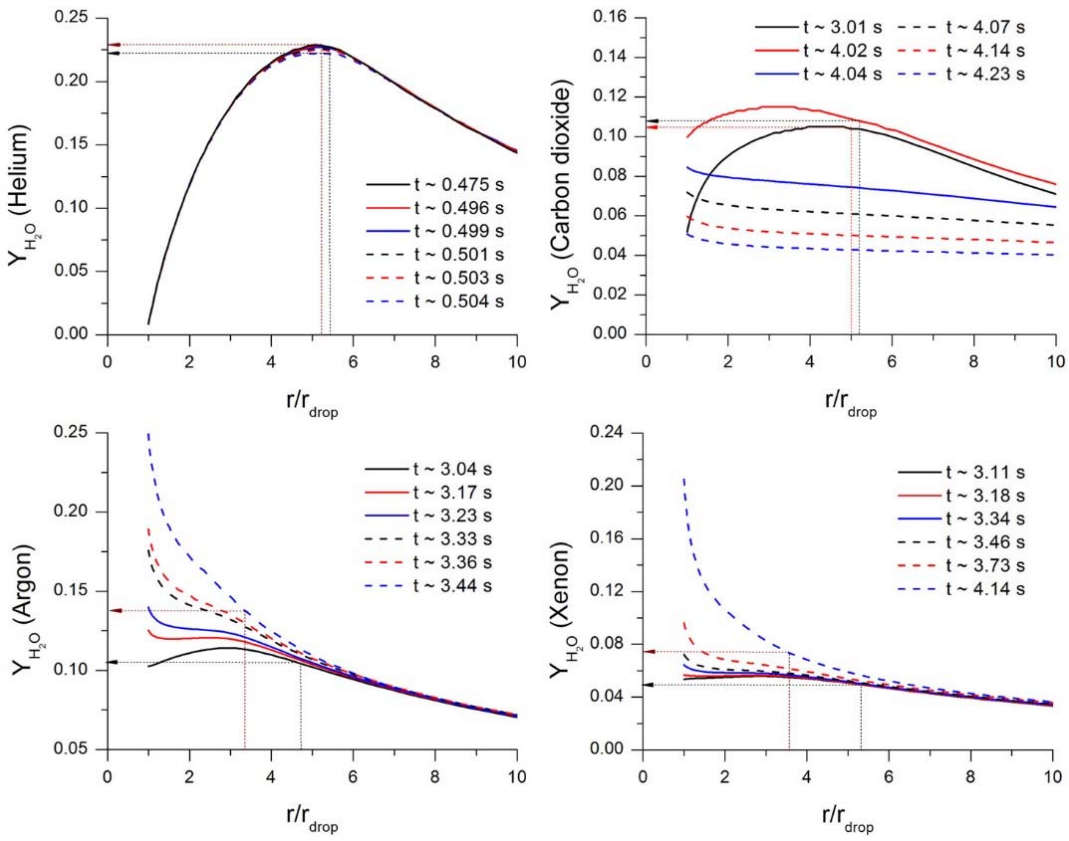

Figure 3.9 Predicted spatial-temporal profile of water mass fraction in the gas phase at near extinction and quasi-steady time snaps prior to extinction for different diluents. Ambient composition: X_{O2}=0.21 and $X_{Diluent}$=0.79. Identical ignition source and initial droplet, D_o = 1.5 mm.

The liquid phase spatial distribution of water mass fraction for the above cases is summarized in Figure 3.10. Methanol droplet in helium accumulates the negligible amount of water during the combustion process with trace amount being transported at the droplet center. Despite the highest value of $D_{H2O\text{-}He}$ amongst the four diluents, the excessively higher gasification rate ($K_{methanol}$) in helium literally poses a 'diffusion barrier' for water in reaching the droplet surface resulting in negligible amounts of water dissolution. In the carbon dioxide enriched ambient, water absorption as high as 40 – 45% (by mass) can be observed through the extinction process which is primarily governed by the radiative heat loss effect. Analogous to the gas phase observation, methanol droplet water uptake (at the point of extinction) exceeds approximately ~83% and ~90% for argon and xenon augmented surrounding respectively. It is worthwhile to mention that compared to argon, extinction in xenon enriched environment takes ~20% additional burn time eventually fostering the observed water absorption in xenon. It has been reported in numerous publications that internal circulation/mixing enhances the water absorption process. In our present simulations, a well-mixed droplet is assumed by imposing a liquid phase unity Lewis number. The influence of the liquid phase Lewis number on the liquid and gas phase water profile is further investigated and reported in the supplementary Figure 3.13. It should be noted that a unity Lewis number at the liquid phase resembles a well-mixed condition (i.e. internal circulation) while a value set to 'zero' replicates the absence of internal circulation. Without a well-mixed condition, very little water gets absorbed into the droplet and results in much smaller predicted extinction diameters.

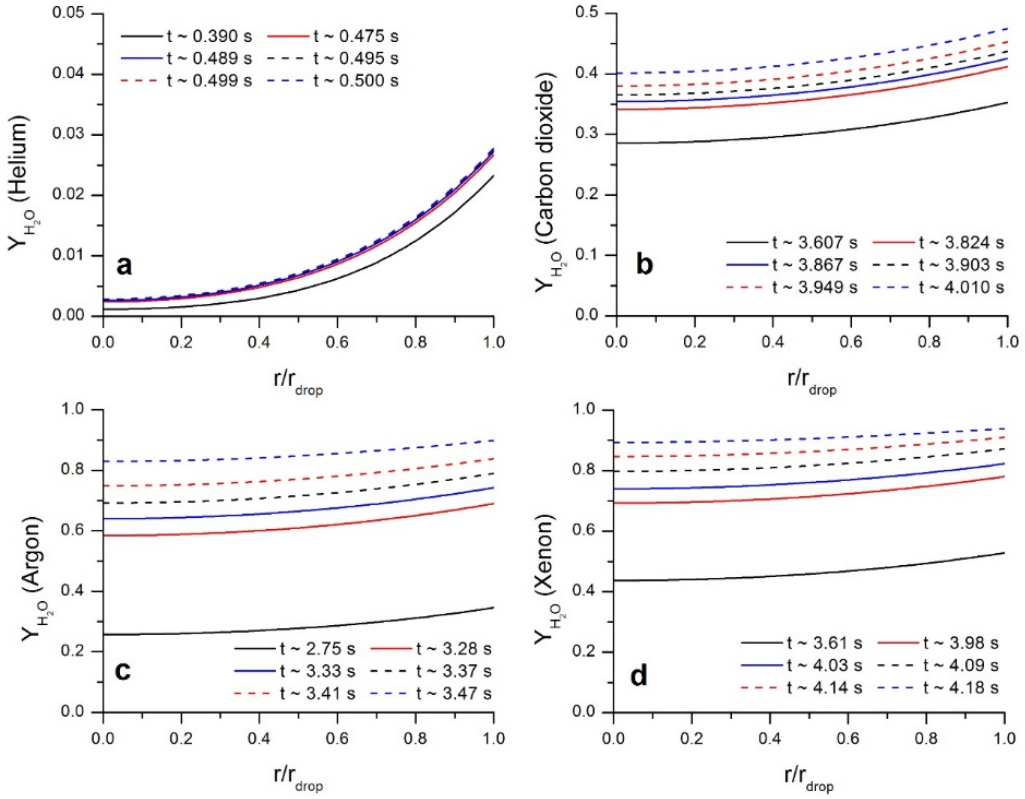

Figure 3.10 Predicted spatial-temporal profile of water mole fraction in the liquid phase at different time snaps near extinction and quasi-steady time prior to extinction. Ambient composition: X_{O2}=0.21 and $X_{Diluent}$=0.79. Identical ignition source and initial droplet diameter, D_o = 1.5 mm.

3.4 CONCLUDING REMARKS

The effectiveness of xenon as a potential fire suppressant for microgravity application has been numerically studied using a recently developed transient, sphero-symmetric droplet combustion model. Methanol is chosen as the model fuel. Three different initial droplet diameters, D_o (1.0 mm, 1.5 mm and 2.0 mm) are considered. For each of these initial droplet diameters, simulations are performed for varying xenon content (mole fraction) in the ambient. *A priori* predictions against ISS test data shows satisfactory agreement. Additional numerical computations are performed to further elucidate the role(s) of diluent species and substitution amounts on the droplet burning parameters

important in terms of fire safety in low gravity environments. The findings of these studies can be summarized as follows-

1. The initial ignition source energy variation has negligible influence on the quasi-steady droplet burning, only minimally affecting the initial ignition transient.
2. The droplet regression rate decreases with increasing xenon content (i.e. decreasing O_2) for a fixed droplet diameter contributing reductions in burning rate and earlier flame extinction at larger extinction diameters.
3. An increase in xenon content diminishes both the maximum peak gas temperature and maximum rate of increase of the peak gas temperature dT_{max}/dt.
4. The flame stand-off ratio (FSR) is found to weakly dependent on the initial droplet sizes while it is strongly affected by the ambient gas composition.
5. The exceptionally low thermal diffusivity of xenon is primarily responsible for the significantly higher peak gas temperature and remarkably low LOI in comparison to helium, carbon dioxide, argon, and nitrogen diluent.
6. Xenon promotes longest burn time compared to other diluents. The unified understanding of longest burn time, maximum peak gas temperature, and lowest LOI conditions clearly suggests that xenon is not an effective choice to improve fire safety characteristics in reduced gravity environments.
7. The LOI for xenon was found to be ~4%, 5% and 6% for 1.0, 1.5 and 2.0 mm droplet sizes respectively. Comparative analysis among four diluents revealed that the LOI was 5%, 8%, 21% and 21% for xenon, argon, helium and carbon dioxide respectively for the same initial drop diameter (D_o = 1.5 mm).

8. Contrary to the heat loss driven extinction phenomena observed with carbon dioxide and helium diluent, extinction in xenon and argon are found to be primarily influenced by water dissolution and it's re-gasification effects.
9. Prior to the extinction, gas phase medium may contain significant water content. Helium-filled ambient was found to hold as high as ~22.5% (by mass) of water near the flame zone whereas CO_2, Ar and Xe surrounding accommodated ~11%, ~14% and ~7% of water respectively. On the other hand, the liquid phase maximum water mass fraction for CO_2, Ar and Xe ambient may attain values as high as ~48%, ~88% and ~93% respectively.

3.5 SUPPLEMENTARY FIGURES

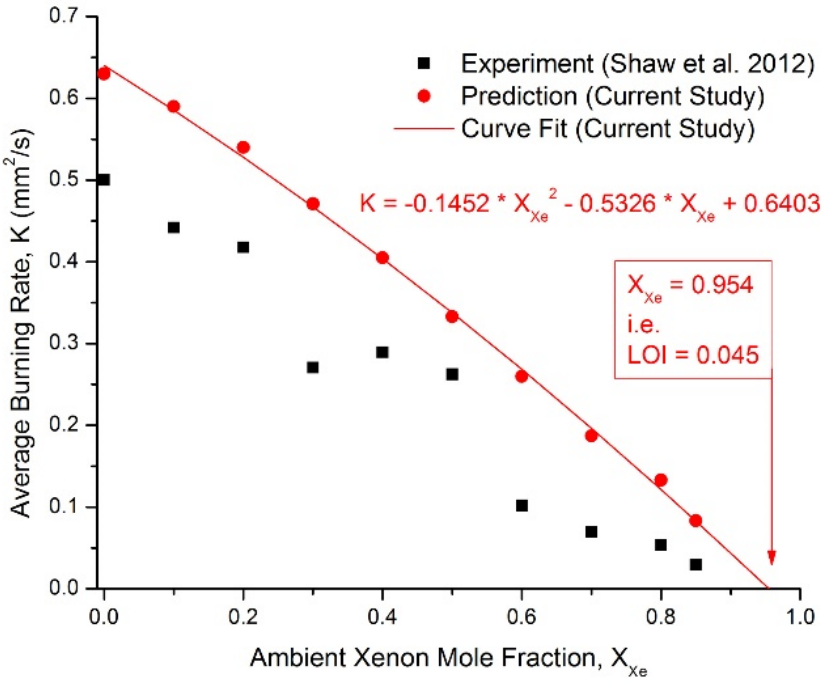

Figure 3.11 Droplet combustion model comparison against average burning rate data from Shaw et al [1]. (D_o = 1.0 mm, varying O_2/Xe ambient with balance N_2. Ambient condition: P = 1 atm and T = 298 K).

Comparative analysis: The numerical results are qualitatively in congruence with Shaw et al. (2012) while showing consistently higher value than experimental observations. Using a second order polynomial fit, it was found that the limiting oxygen index (LOI) was ~ 4.5%.

The causes of this difference between these two studies are difficult to determine as the experimental work did not explicitly point out the possible sources and/or magnitudes of uncertainties associated with the experimental data. As a benchmark check, for X_{Xe}=0% (i.e. pure air), our predicted results are in excellent agreement with previous studies [4, 14, 22].

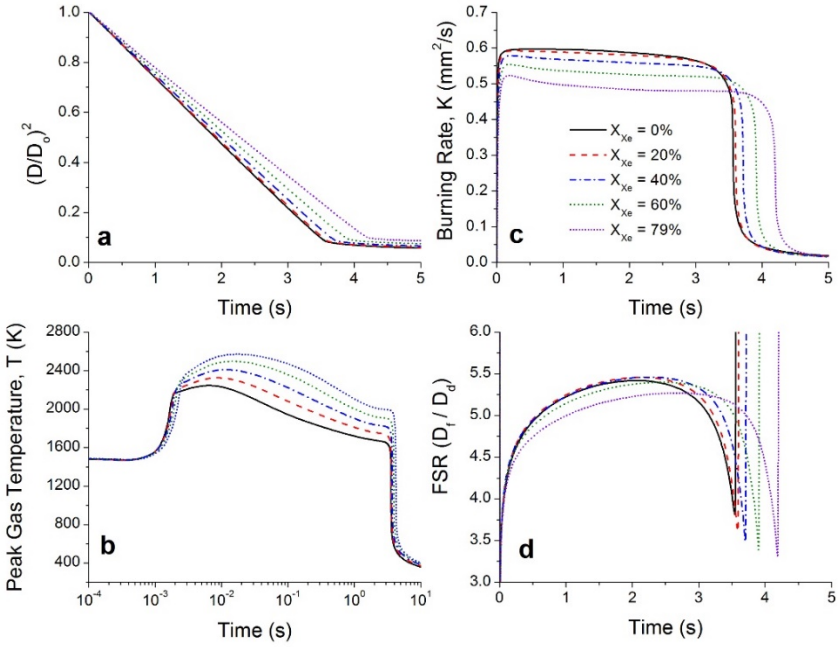

Figure 3.12 Computational analysis of diluent exchange (N_2/Xe) effect on methanol droplet combustion: (a) droplet diameter regression (b) peak gas temperature (c) instantaneous burning rate and (d) FSR evolution (D_o = 1.5 mm, X_{O2} = 21%, atmospheric pressure).

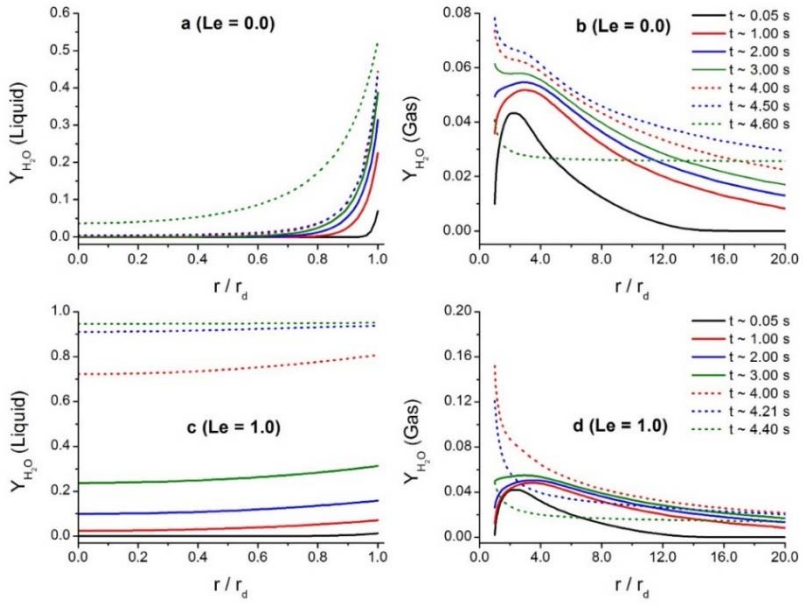

Figure 3.13 Effect of liquid phase internal circulation on accumulated water mass fraction for xenon filled ambient (D_o = 1.5 mm, X_{O2} = 21%, 1 atm). (a) liquid phase without internal circulation, (b) gas phase with internal circulation, (c) liquid phase with full internal circulation, and (d) gas phase with full internal circulation.

3.6 REFERENCES

[1] B. Shaw, J. Wei, Combustion of Methanol Droplets in Air-Diluent Environments with Reduced and Normal Gravity, Journal of Combustion, 2012 (2012) 8.

[2] M.Y. Choi, F.L. Dryer, Microgravity Combustion: Fire in Free Fall (in *Microgravity Droplet Combustion*), in: H.D. Ross (Ed.), Academic Press, 2001, pp. 183-297.

[3] M.Y. Choi, F.L. Dryer, J.B.J. Haggard, M.H. Brace, The Burning Behavior of Methanol Droplets in Humid Air, in: Eastern States Fall Technical Meeting of the Combustion Institute, Clearwater Beach, FL, December 1988, 1988.

[4] T.I. Farouk, F.L. Dryer, On the extinction characteristics of alcohol droplet combustion under microgravity conditions – A numerical study, Combust. Flame, 159 (2012) 3208-3223.

[5] M.Y. Choi, Droplet combustion characteristics under microgravity and normal-gravity conditions, in: Mechanical & Aerospace, Princeton University, NJ, USA, 1992.

[6] A. Lee, C.K. Law, An Experimental Investigation On the Vaporization and Combustion of Methanol and Ethanol Droplets, Combustion Science and Technology, 86 (1992) 253-265.

[7] A.J. Marchese, F.L. Dryer, The effect of liquid mass transport on the combustion and extinction of bicomponent droplets of methanol and water, Combustion and Flame, 105 (1996) 104-122.

[8] H.A. Dwyer, I. Aharon, B.D. Shaw, H. Niamand, Surface tension influences on methanol droplet vaproiation in the presence of water, Symposium (International) on Combustion, 26 (1996) 1613-1619.

[9] A. Kazakov, J. Conley, F.L. Dryer, Detailed modeling of an isolated, ethanol droplet combustion under microgravity conditions, Combustion and Flame, 134 (2003) 301-314.

[10] S.Y. Cho, M.Y. Choi, F.L. Dryer, Extinction of a free methanol droplet in microgravity, Symposium (International) on Combustion, 23 (1991) 1611-1617.

[11] J.C. Yang, G.S. Jackson, C.T. Avedisian, Combustion of unsupported methanol/dodecanol mixture droplets at low gravity, Symposium (International) on Combustion, 23 (1991) 1619-1625.

[12] C. Chauveau, I. Gökalp, D. Segawa, T. Kadota, H. Enomoto, Effects of reduced gravity on methanol droplet combustion at high pressures, Proceedings of the Combustion Institute, 28 (2000) 1071-1077.

[13] K. Okai, O. Moriue, M. Araki, M. Tsue, M. Kono, J. Sato, D.L. Dietrich, F.A. Williams, Pressure effects on combustion of methanol and methanol/dodecanol single droplets and droplet pairs in microgravity, Combustion and Flame, 121 (2000) 501-512.

[14] A.J. Marchese, F.L. Dryer, The Effect of Non-Luminous Thermal Radiation in Microgravity Droplet Combustion, Combustion Science and Technology, 124 (1997) 371-402.

[15] B.H. Chao, C.K. Law, J.S. T'Ien, Structure and extinction of diffusion flames with flame radiation, Symposium (International) on Combustion, 23 (1991) 523-531.

[16] B.L. Zhang, J.M. Card, F.A. Williams, Application of rate-ratio asymptotics to the prediction of extinction for methanol droplet combustion, Combustion and Flame, 105 (1996) 267-290.

[17] M.C. Hicks, V. Nayagam, F.A. Williams, Methanol droplet extinction in carbon-dioxide-enriched environments in microgravity, Combustion and Flame, 157 (2010) 1439-1445.

[18] H.A. Dwyer, B.D. Shaw, Marangoni and Stability Studies on Fiber-Supported Methanol Droplets Evaporating in Reduced Gravity, Combustion Science and Technology, 162 (2001) 331-346.

[19] V. Raghavan, V. Babu, T. Sundararajan, R. Natarajan, Flame shapes and burning rates of spherical fuel particles in a mixed convective environment, International Journal of Heat and Mass Transfer, 48 (2005) 5354-5370.

[20] V. Raghavan, D.N. Pope, D. Howard, G. Gogos, Surface tension effects during low-Reynolds-number methanol droplet combustion, Combustion and Flame, 145 (2006) 791-807.

[21] T. Farouk, F.L. Dryer, Tethered methanol droplet combustion in carbon-dioxide enriched environment under microgravity conditions, Combustion and Flame, 159 (2012) 200-209.

[22] I. Awasthi, G. Gogos, T. Sundararajan, Effects of size on combustion of isolated methanol droplets, Combustion and Flame, 160 (2013) 1789-1802.

[23] J.B. Wei, B.D. Shaw, Reduced Gravity Combustion of Propanol Droplets in Oxygen-Inert Environments, Combustion Science and Technology, 181 (2009) 1480-1494.

[24] B.D. Shaw, J.B. Wei, Influence of Gravity and Ambient Pressure on Combustion and Flammability of n-Heptane and 1-Propanol Droplets in Air-Diluent Environments, Combustion Science and Technology, 183 (2011) 969-983.

[25] S. Nakaya, K. Fujishima, M. Tsue, M. Kono, D. Segawa, Effects of droplet diameter on instantaneous burning rate of isolated fuel droplets in argon-rich or carbon dioxide-rich ambiences under microgravity, Proceedings of the Combustion Institute, 34 (2013) 1601-1608.

[26] Y. Jin, B.D. Shaw, Computational modeling of n-heptane droplet combustion in air–diluent environments under reduced-gravity, International Journal of Heat and Mass Transfer, 53 (2010) 5782-5791.

[27] A.J. Marchese, F.L. Dryer, R.O. Colantonio, Radiative effects in space-based methanol/water droplet combustion experiments, Symposium (International) on Combustion, 27 (1998) 2627-2634.

[28] T. Farouk, F.L. Dryer, Microgravity droplet combustion: effect of tethering fiber on burning rate and flame structure, Combust. Theory Modell., 15 (2011) 487-515.

[29] J. Li, Z. Zhao, A. Kazakov, M. Chaos, F.L. Dryer, J.J. Scire, A comprehensive kinetic mechanism for CO, CH2O, and CH3OH combustion, International Journal of Chemical Kinetics, 39 (2007) 109-136.

[30] M.P. Burke, M. Chaos, Y. Ju, F.L. Dryer, S.J. Klippenstein, Comprehensive H2/O2 kinetic model for high-pressure combustion, International Journal of Chemical Kinetics, 44 (2012) 444-474.

[31] T.E. Daubert, R.P. Danner, H. Sibul, C. Stebbins, Physical and thermodynamic properties of pure chemicals: data compilation, (1989).

[32] D.L. Dietrich, V. Nayagam, M.C. Hicks, P.V. Ferkul, F.L. Dryer, T. Farouk, B.D. Shaw, H.K. Suh, M.Y. Choi, Y. Liu, C.T. Avedisian, F.A. Williams, Droplet Combustion

Experiments Aboard the International Space Station, Microgravity Sci. Technol., (2014) 1-12.

[33] T.I. Farouk, Y.C. Liu, A.J. Savas, C.T. Avedisian, F.L. Dryer, Sub-millimeter sized methyl butanoate droplet combustion: Microgravity experiments and detailed numerical modeling, Proc. Combust. Inst., 34 (2013) 1609-1616.

[34] D.L. Dietrich, J.B. Haggard Jr, F.L. Dryer, V. Nayagam, B.D. Shaw, F.A. Williams, Droplet combustion experiments in spacelab, Symposium (International) on Combustion, 26 (1996) 1201-1207.

[35] B.E. Poling, J.M. Prausnitz, J.P. O'Connell, The Properties of Gases and Liquids, McGraw-Hill Education, USA, 2000.

[36] V. Nayagam, Activation energy asymptotics for methanol droplet extinction in microgravity, Combustion and Flame, 160 (2013) 2638-2640.

CHAPTER 4

N-BUTANOL (n-C_4H_9OH) DROPLET COMBUSTION: NUMERICAL MODELING AND REDUCED GRAVITY EXPERIMENTS

4.1 ABSTRACT

Recent interest in alternative and bio-derived fuels has emphasized butanol over ethanol as a result of its higher energy density, lower vapor pressure, and more favorable gasoline blending properties. Numerous efforts have examined the combustion of butanol from the perspective of low dimensional gas-phase transport configurations that facilitate modeling and validation of combustion kinetics. However, fewer studies have focused on multiphase butanol combustion, and none have appeared so far on the isolated droplet combustion that couples experiment with robust modeling of the droplet burning process. This chapter presents such an experimental/numerical modeling study of isolated droplet burning characteristics of n-Butanol. The experiments are conducted in an environment that simplifies the transport process to one that is nearly one dimensional as promoted by burning in a reduced gravity environment. Measurements of the evolution of droplet diameter (D_o = 0.56–0.57 mm), flame standoff ratio (FSR ≡ D_f / D) and burning rate (K) are made in the standard atmosphere under reduced gravity and the data are compared against numerical simulation. The detailed results are based on comprehensive time-dependent, sphero-symmetric droplet combustion simulation that includes spectrally resolved radiative heat transfer, multi-component diffusive transport, temperature dependent thermal property variations and detailed chemical kinetics. The simulations are carried out using both a large order kinetic model (284 species, 1892 reactions) and a reduced order model (44 species, 177 reactions). The results show that the predicted burning history and flame standoff ratios are in good agreement with the measurements for

both the large and reduced order models. Additional simulations are conducted for varying oxygen (O_2) concentration to determine the limiting oxygen index and to elucidate the kinetic processes that dictate the extinction of the flame at these low oxygen concentrations.

4.2 INTRODUCTION

The growing interest in normal butanol (n-C_4H_9OH, boiling point of 390.8 K [1]) as a nonpetroleum fuel for internal combustion engines, either as a gasoline surrogate or an additive to increase performance of both gasoline and diesel fuels due to its favorable properties relative to ethanol [2-4], has stimulated fundamental research to understand its combustion kinetics. The experimental configurations used for this purpose typically incorporate a zero or one-dimensional transport dynamic (i.e., in shock tubes [5-7]), constant volume combustion chambers [8], jet stirred reactors [9-15] and opposed flow diffusion flames [16] with pre-vaporized butanol to facilitate ab initio modeling of the flow and combustion dynamics involved.

Few studies of n-Butanol combustion have been carried out to evaluate kinetic models derived from spray or droplet dynamics, and none have done so incorporating detailed kinetic scheme. The work of Wang et al. [17] is noteworthy for using the environment of a direct injection diesel engine fueled with a mixture of diesel fuel and n-Butanol to validate a reduced kinetic model using the KIVA-3v code [18], which requires certain spray model constants to be calibrated and adjusted to make the liquid and vapor penetrations match experimental measurement of these quantities, as well as sub-model

inputs for turbulence, gas jet/collision for spray, spray/droplet breakup, and droplet evaporation and wall collision dynamics.

The simplest configuration for a liquid fuel that is amenable to detailed simulation is an isolated droplet burning in an environment in which streamlines of the flow are radial and the mass and energy transport are one-dimensional due to the evaporation process. As simple as the one-dimensional droplet flame may appear, it is relevant to the complex environment of a spray through elements that carry over to the spray environment [19]. These include moving boundary effects, unsteady heat conduction and mass diffusion in the droplet and surrounding gas, variable gas phase properties (dependent on temperature and composition), phase equilibrium at the interface, radiation dynamics, and a detailed kinetic model for the combustion process. Computer simulations based on assuming spherical symmetry recently been applied to a range of fuels including alkane, alcohol and methyl ester [20-23].

In this paper, we present a comprehensive numerical simulation of the combustion of isolated n-Butanol droplets that assumes spherical symmetry. The intent is to examine the potential of the combustion kinetics previously developed for butanol using targets from low dimensional gaseous configurations as noted previously, to predict multiphase droplet combustion targets. These include the evolutions of droplet and flame diameters (D and D_f, respectively), and the burning rate $K = \left|\frac{dD^2}{dt}\right|$.The initial droplet diameters (D_o) are essentially constant in this study (between 0.56 mm and 0.57 mm) and the combustion process is examined at standard atmosphere. The simulations presented here employ a detailed kinetic model for n-Butanol that incorporates 284 species and 1892 reactions [24].

The results are compared to experimental data as well as to predictions that employed a reduced order kinetic model [17] consisting of 44 species and 177 reactions.

4.3 EXPERIMENTAL SETUP AND PROCEDURE

Reduced gravity droplet combustion experiments of n-Butanol droplets were conducted in Cornell University drop tower facility. Individual n-Butanol droplets are formed, deployed, and ignited under conditions that achieve nearly spherically symmetric burning. Prior studies using the same facility (e.g., [23, 25, 26]) demonstrated the establishment of nearly spherical flames by burning the test fuel droplets under free-fall conditions. Figure 4.1 illustrates the experimental procedures for the present study.

A piezoelectric droplet generator [27] propels fuel droplets (D_o on the order of between 0.5 mm and 0.6 mm) onto the intersection of two 14 μm Silicone carbide (SiC) fibers crossed at approximately 60^o [25, 28]. The fuel droplet is then ignited 320 ms after the initiation of free-fall by symmetric spark discharge across two electrode pairs positioned on opposite sides of the droplet. The sparks remain activated for about 800 μs (or ~1% of the nominal burning time of the droplets examined in this study) and then the electrodes are rapidly retracted away from the combustion zone after the burning commences.

Since the test droplet is anchored by fibers while it burns in the current investigation, the potential for an influence of the supporting fiber on burning was examined by comparing free-floating and fiber-supported burning histories of droplets with nominally the same initial diameters. The evolutions of D and D_f for free and supported droplets were found to be well correlated [28, 29].

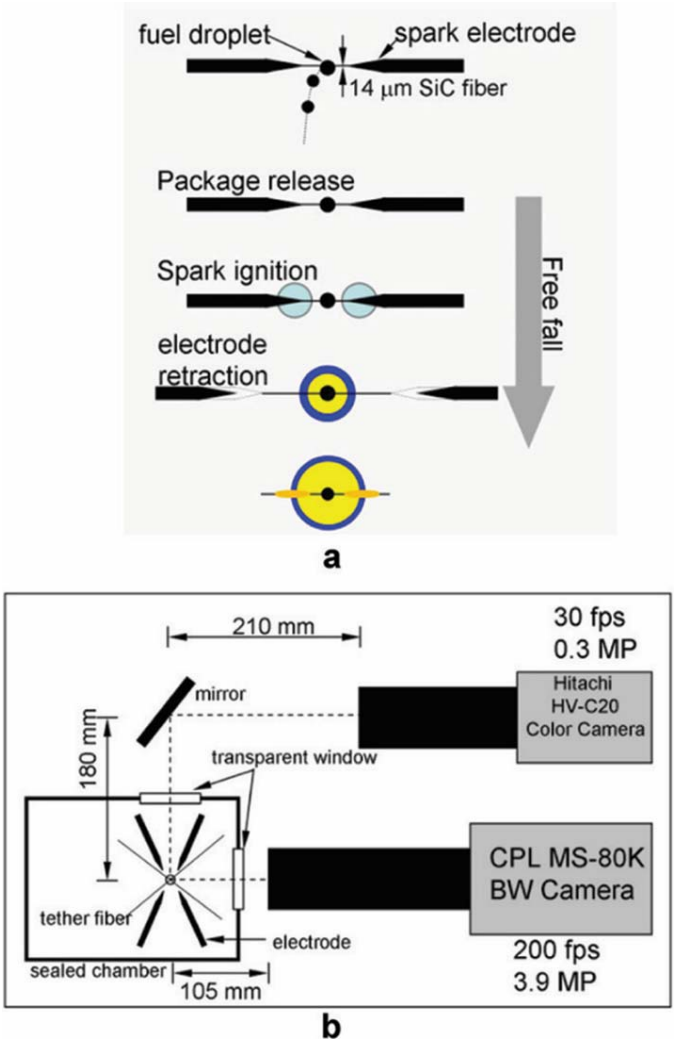

Figure 4.1 (a) Schematic diagram of experimental procedure to deploy droplets onto SiC fiber, (b) experimental setup of Cornell University drop tower facility (dimensions in millimeters, not to the scale). Courtesy- Professor C.T. Avedisian, Cornell University, NY, USA.

Video imaging is the main diagnostic that provides a record of the burning history from which quantitative measurements are extracted. The droplet burning process is simultaneously recorded by individual cameras from two orthogonal views (Figure 4.1 (b)). A color video camera (Hitachi HV-C20 (0.3 MP per frame) operated at 30 fps with a Nikkor 135 mm f/2.0 lens and two Kenko 36 mm extension tubes) documented self-illuminated flame images. A high-speed high-resolution black and white (BW) digital camera (3.9 MP per frame Canadian Photonics Labs (CPL), Inc. MS-80K, operated at 200

fps, and fitted with an Olympus Zuiko 90 mm f/2.0 lens, an Olympus OM Telescopic Extension Tube 65–116 mm (fixed at 100 mm), and a Vivitar MC 2X teleconverter) recorded the backlit droplet images during the burn. Backlighting was provided by a 1-Watt LED lamp (Black Diamond Equip, LTD). Three separate repetitions having identical initial conditions were performed to examine experimental repeatability.

Quantitative data are obtained from the BW digital video records of the droplet burning histories through a frame-by-frame analysis using a MATLAB (https://www.mathworks.com/) based algorithm [30], which was periodically cross-checked with manual measurements using image processing tool Image-Pro Plus v6.3 (http://www.mediacy.com/imageproplus). Flame diameters are determined from the color images using CorelDraw 9 software (http://www.coreldraw.com/en/), in which a digital ellipse is manually positioned around the outer luminous zone of the flame to yield an equivalent flame diameter.

4.4 NUMERICAL MODELING

The experimental results are compared against computational predictions using recently developed spherically symmetric droplet combustion model, the details of which appear in chapter 2 of this thesis. As stated earlier, the model features detailed gas phase kinetics, here being for n-Butanol, spectrally resolved radiative heat transfer, multi-component transport and heat transfer perturbations due to the presence of the tether fibers. The data correlations of Daubert and Danner [31] were used to calculate the liquid phase properties of n-Butanol.

Two different chemical kinetic models are employed for simulating the isolated droplet combustion of n-Butanol. These models are adopted from Sarathy et al. [24] and Wang et al. [17] and enumerated hereafter as 'detailed' and 'reduced' models respectively. The detailed model of Sarathy et al encompasses 431 species undergoing 2336 elementary reactions while its counterpart 'reduced' model of Wang et al. contains 47 species and 189 elementary reactions. It should be noted that the models employed here are strictly valid for high-temperature oxidation of n-Butanol essentially excluding any of the low-to-intermediate temperature reaction pathways. Experimental study of gas phase n-Butanol oxidation under shock tube configuration [32] demonstrates that the exhibition of low and intermediate temperature kinetic behavior (inclusive of NTC) are prevailing only at high-pressure range. Typical simulation time for 350 grid points on a stand-alone eight core Linux workstation comprising 2.4 GHz processor speed and 20 GB RAM took ~68 CPU hours for the detailed kinetic model, whereas the calculations with the reduced model were completed in ~0.34 CPU hours. Additionally, we also endeavored to use the kinetic model of Harper et al. [33] but were unable to obtain any converged solutions.

In the simulations, the Dirichlet condition of fixed ambient composition (21% O_2 and 79% N_2) and temperature (298 K) are prescribed surrounding the droplet and also at the far-field as Dirichlet boundary condition. A trapezoidal initial temperature profile at the time, t=0, similar to described in chapter 2, having a peak temperature of 2000 K and ignition energy of ~0.08 J was used to simulate the spark ignition source of the experiments [23]. Thus, the initial ignition energy is provided by the energy density ($m * Cp * \Delta T$) of the specified temperature profile integrated over the prescribed volume. The results of the simulations are compared with the experimental data in the next section and then used to

simulate additional conditions to provide insights into the n-Butanol droplet burning process.

4.5 RESULTS AND DISCUSSIONS

Figure 4.2 shows an exemplary set of photographs of the n-Butanol droplet burning history as obtained from the digital video records. Some initial asymmetry of the flame structure exists due to gas motions induced by spark ignition and electrode retractions, though the flame shapes were largely spherical throughout the burning process. As is evident from this figure, no soot formation is observed for n-Butanol droplet combustion (i.e., no soot shell). The sequences of color images show a faint blue luminosity indicative of CH emissions, and no luminosity characteristic of soot formation.

Figure 4.3 illustrates the quantitative measurements of the evolution of droplet diameter and FSR of three individual experimental runs in the coordinates of the classical D^2 law [34] with nominally the same initial diameters. Both the figures indicate that the experiments are highly repeatable with little scattering in the data, especially for the droplet diameter. It is apparent from the droplet diameter regression that no flame extinction is observed.

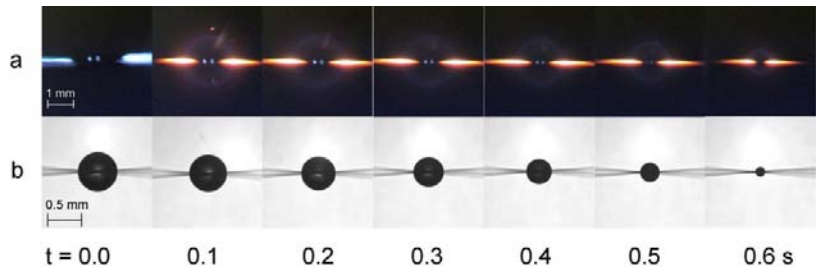

Figure 4.2 (a) Selection of color images of droplet showing flame structure (glow is due to flame/fiber interaction). (b) Selection of BW images for a burning n-Butanol droplet in atmospheric air.

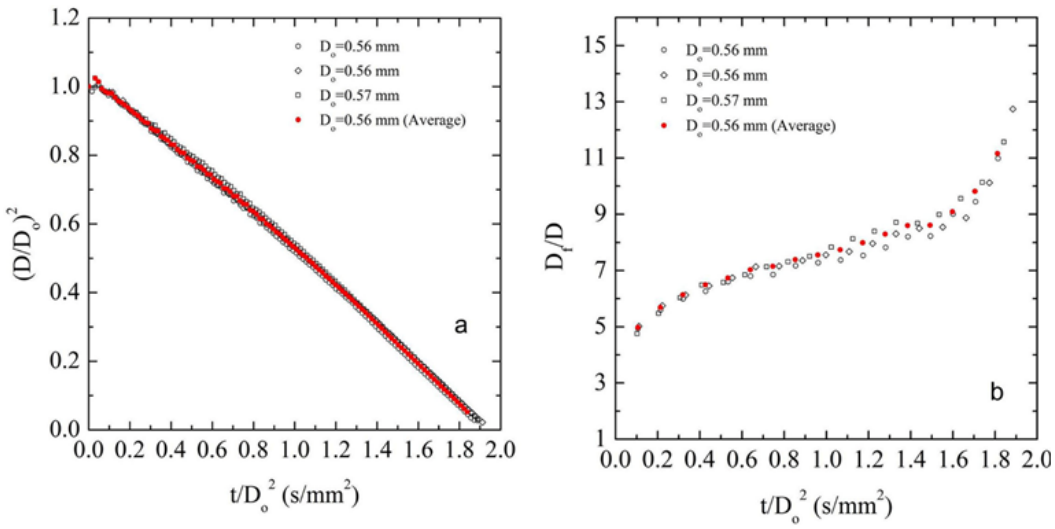

Figure 4.3 Evolution of n-Butanol droplet (a) burning history (b) flame stand-off ratio for three individual runs (1 atm, 21% O_2/balance N_2).

The evolution of flame diameter as extracted from the color images is shown in Figure 4.3 (b), is presented in term of the relative position of the flame boundary to the droplet boundary, FSR. The trends are significantly different from the classical theory that predicts D_f/D to be constant. Due to the lower resolution of the color camera and greater difficulty of identifying the flame boundary (taken as the outer luminous zone as discerned manually), there are fewer flame diameter data, and with larger uncertainty, compared to the droplet diameter measurements.

Figure 4.4 compares the simulated evolution of droplet diameter and FSR against experimental values for both detailed and reduced kinetic schemes. Predictions from both the detailed and reduced model are also summarized. The standard deviations pertaining to each averaged data point are calculated from the data for the three individual experiments. The predicted droplet diameter regressions from both the models show good qualitative trends in comparison to the experimental data Up to approximately 50% of the burn, predictions from the model are almost identical and are in very good agreement with the

measured data. However, beyond 50% of the burn-time slight deviation between the predictions and measurements start to exist. The discrepancy with the measurements increases when the reduced kinetic model is employed compared to the detailed kinetic model, as expected since reduced kinetic models removed possibly finer kinetic aspects during the process of reduction. However, the variation between the two models for the droplet diameter regression is not significant. The overall increase in deviation for the predicted and experimental values during the latter stages of burning (i.e. with smaller droplet diameter, viz at smaller Damköhler numbers) may be attributed to droplet- fiber interactions or possibly limitation of the combustion kinetics.

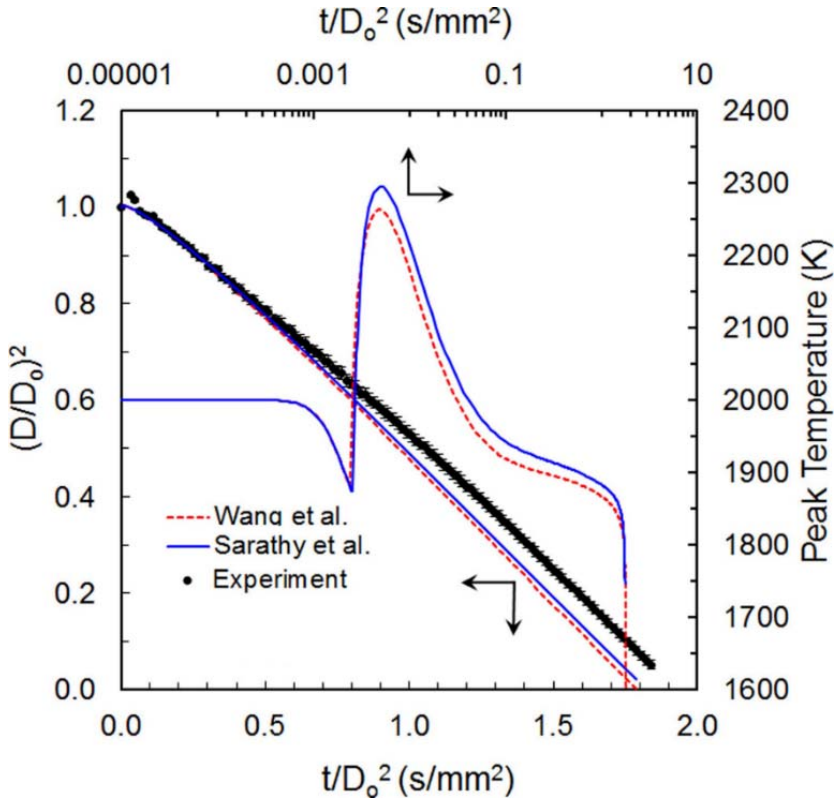

Figure 4.4 Predicted evolution of droplet diameter and peak gas temperature profiles for n-Butanol droplet (D_o = 0.56 mm, 1 atm, 21% O_2/balance N_2). The secondary axes (upper logarithmic X-axis and right side Y-axis) correspond to temperature evolution.

The evolution of predicted peak gas temperature (T_{max}) is also shown in Figure 4.4 with the temporal scale (i.e. t/D_o^2) being presented in a logarithmic format to provide more detailed insight into the earlier transient evolution of T_{max}. It can be seen that there are negligible differences between the two kinetic models in the T_{max} predictions, and the ignition delay time between both models is indistinguishable with temperature ramping rates (i.e. dT_{max}/dt) being identical. The peak temperature decreases before ignition resulting from endothermic reactions and droplet heat sinking effect, which is also almost identical for the two models.

The difference in peak temperature predicted by the two kinetic models is ~40 K and ~30 K during maximum temperature difference and quasi-steady condition, respectively. The variation in the peak gas temperature is due to the additional reaction pathways that are considered in the detailed model. Due to these additional reaction pathways, the net of endothermic and exothermic reaction processes leads to a higher sensible enthalpy within the flame zone. It is interesting to the note that even though the reduced model predicts lower flame temperature during the quasi-steady burn, K_{avg} is slightly higher.

Figure 4.5 compares predicted droplet burning of n-Butanol droplet burning against two other prominent oxygenated fuels (methanol & ethanol) under same initial diameters, ambient and ignition conditions is shown in Figure 4.5. The reaction scheme for the methanol is adapted from Li et al. [35] with the H_2/O_2 updates from Burke et al. [36]. For the ethanol, we employed the kinetic model of Haas and coworkers [37]. n-Butanol is found to have the slowest average burning rate [K_{C4H9OH} (0.583 mm^2/s) < K_{C2H5OH} (0.613 mm^2/s) < K_{CH3OH} (0.667 mm^2/s)] (Figure 4.5 (a)). In addition, as droplet burning proceeds both

methanol and ethanol undergo extinction at finite diameters mainly due to a water dissolution effect whereas n-Butanol burns to completion. In general, the average burning rates (K_{avg}) for the detailed model predictions were found to be slightly lower in comparison to the reduced model. The average burning rate computed from the detailed and reduced reaction model differed by ~3%, 0.583 mm^2/s for the detailed model and 0.602 mm^2/s for the reduced model. Both kinetic models predict complete burning without any flame extinction, as also observed experimentally. It is also observed that among the three oxygenated fuels, n-Butanol flames out latest compared to other two fuels.

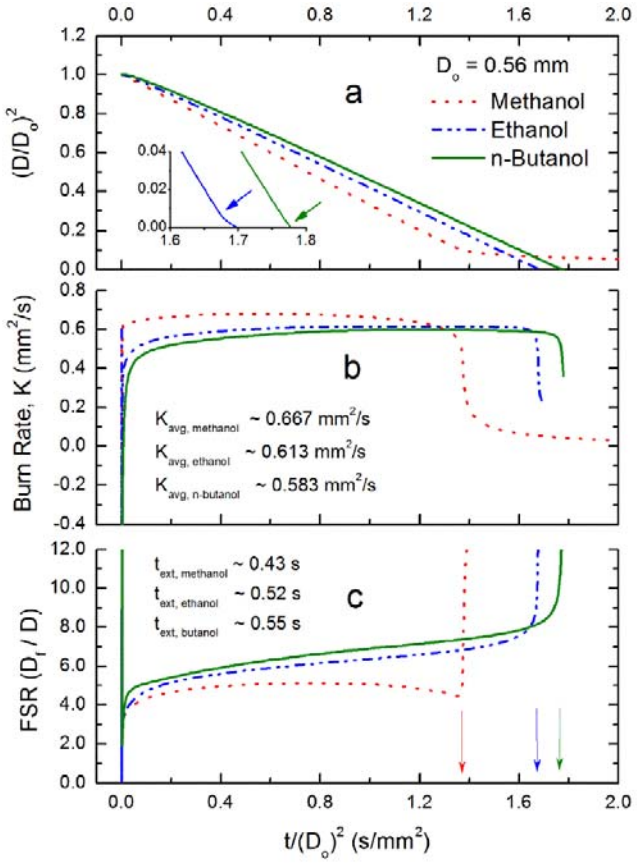

Figure 4.5 Numerical prediction comparison for methanol, ethanol, and n-Butanol droplet combustion: (a) burning history with an enlarged view of ethanol & n-Butanol burning prior to extinction (blue arrow: ethanol slope change indicator, green arrow: n-Butanol full depletion indicator), (b) burning rate, (c) FSR. D_o = 0.56 mm, 21% O_2/balance N_2, 1 atm. Kinetic models: methanol [35], ethanol [37] and n-butanol [16].

Figure 4.6 compares predicted and measured FSR data averaged over the three individual experimental runs where the numerically computed flame position was based on the location of T_{max} [21] and the location of maximum heat release rate (HRR_{max}). Error bars are indicated (mean and standard deviation). The results from both kinetic models capture the qualitative trends of the experiments quite well. The analysis indicates that the HRR_{max} option is more favorable compared to T_{max} in predicting the flame location. The FSR of n-Butanol increases throughout the droplet lifetime due to thermal buffering of the far field that leads to decreased loss of heat from the flame structure and an ever-increasing FSR as burning progress. The thermal buffering of the far field is typically observed for sub-millimeter sized droplets. Even though it is found that the reduced model has a slightly higher burning rate (Figure 4.4), counter-intuitively it predicts a slightly smaller FSR indicating the flame to be located closer to the droplet. It is due to this fact that even with slightly lower flame temperature the reduced model predicts a higher burning rate.

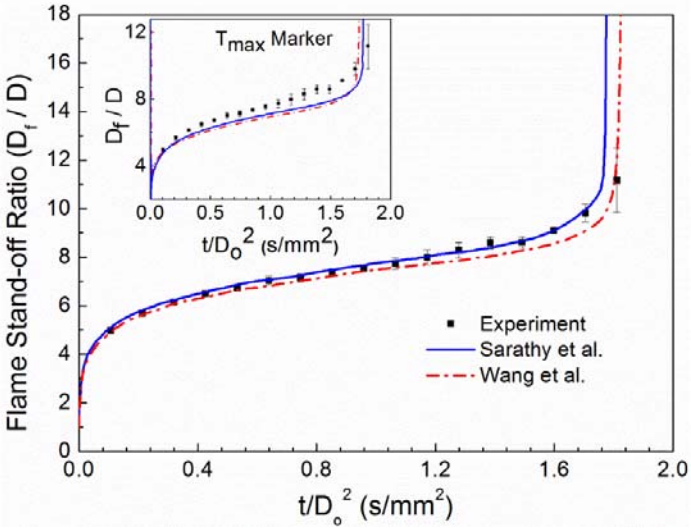

Figure 4.6 Comparison between measured and predicted FSR for n-Butanol droplet (D_o = 0.56 mm, 1 atm, 21% O_2/balance N_2. HRR_{max} marker: central figure; T_{max} marker: inset figure.

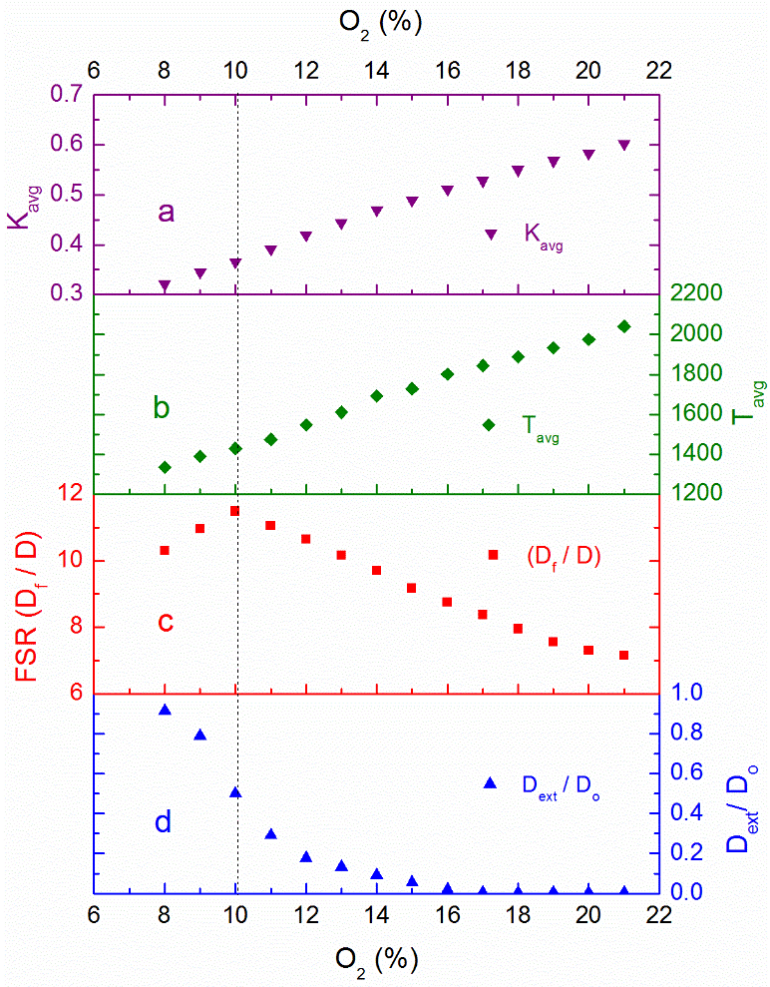

Figure 4.7 Predicted (a) average burning rate, K_{avg} (b) average gas temperature, T_{avg} (c) FSR_{avg} and (d) normalized extinction diameter (D_{ext}/D_o) as a function of X_{O2} for n-Butanol droplet using detailed kinetics [16] (D_o = 0.56 mm, 1 atm). The dashed line marks the location of limiting oxygen index (LOI) condition.

To further elucidate the flame structure and kinetic effects of n-Butanol, computations were performed for a broad range of ambient oxygen concentrations ($0.08 \leq X_{O2} \leq 0.21$). Figure 4.7 presents predicted K_{avg}, T_{avg}, FSR_{avg} and the normalized extinction diameter (D_{ext}/Do) as a function of oxygen concentration, X_{O2}. The numerical data are obtained by time averaging the predicted values over the range $0.10 < t_b < 0.95$. In general, these average quantities provide insight into the quasi-steady combustion characteristics. As the figure illustrates, increasing X_{O2} increases the burning rate by increasing the flame

temperature. Both K_{avg} and T_{avg} show an almost linear variation as a function of X_{O2}. By contrast, the FSR_{avg} decreases with increasing X_{O2}, as stoichiometric conditions are achieved nearer the droplet surface.

As the limiting oxygen index (LOI) is approached (i.e. decrease in O_2), a sharp decrease in the FSR_{avg} is observed. This decrease is due to an inability to achieve quasi-steady burning conditions. Based on the variation of the FSR_{avg} the LOI for these sub-millimeter sized n-Butanol droplets is found to be 0.10 atmospheric pressure. Extinction starts occurring at X_{O2} = 0.16 with sharp increases in extinction diameter as LOI is approached. Unlike other C_1–C_3 alcohols (i.e. methanol, ethanol, and propanol) n-Butanol does not absorb water; therefore, flame extinction in these small-sized droplets is not due to water dissolution rather kinetic effects.

The evolutions of peak mass fraction (PMFs) for some selected species are presented in Figure 4.8 and Figure 4.9 for X_{O2} = 13% and 21% respectively. In this high-temperature droplet combustion, the n-Butanol is predominantly decomposed by H abstraction/alkyl/radical beta scission reactions [24]. The hydrogen atom is the principle abstractor, consuming the majority of the fuel. Among the intermediates, C_2H_4 is the most prominent species for both the cases, which is followed by C_2H_2 and C_3H_6. Ethylene in n-Butanol combustion has been reported either through H-abstraction in a-position, producing ethyl radicals, which subsequently forms C_2H_4 through b-scission [11, 15] or via x-Hydrogen abstraction producing C_2H_4 as a direct β-scission product (nC_4H_9OH ➔ C_4H_8OH-4 ➔ C_2H_4 + pC_2H_4OH) [14]. The large amounts of C_2H_4 also promote the formation of vinyl radicals (C_2H_3). The consumption pathways of the C_2H_3 result in the

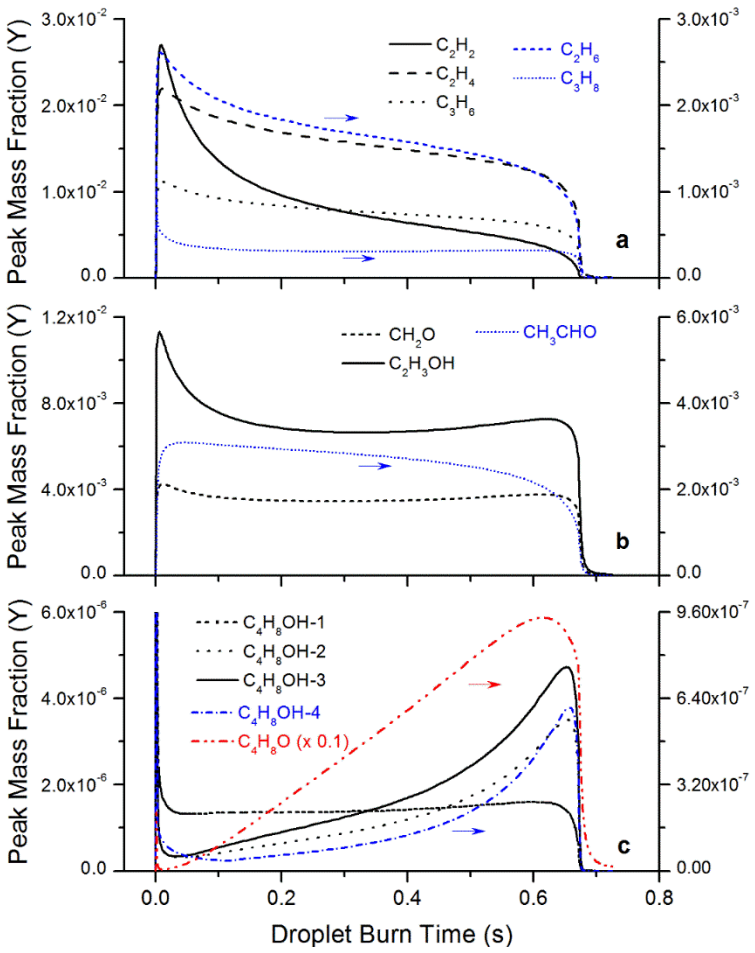

Figure 4.8 Predicted temporal evolution of peak mass fraction of selective species for n-Butanol droplet combustion (D_o = 0.56 mm, 13% O_2/balance N_2, 1 atm).

formation of C_2H_2 (C_2H_3+H ➔ C_2H_2+H_2). However, in comparison, C_2H_6 and C_3H_8 are found to be lower by an order of magnitude, which is qualitatively in congruence with ref [38]. Recombination of methyl and ethyl radicals, along with H-abstraction from formaldehyde by n-propyl radicals contribute to the C_3H_8 formation [33]. All these species are formed in the fuel-rich side of the diffusion flame structure [21]. At lower Damköhler numbers (i.e. X_{O2} = 13%), all the smaller C-H species PMF profiles remains nearly same except C_2H_2, which reduces by a factor ~2.2 indicating that n-Butanol is less susceptible to soot formation even in lower O_2 environments. On the other hand, for C_3H_6, the

significant formation channel are: (i) $C_4H_8OH\text{-}3 = C_3H_6 + CH_2OH$ where $C_4H_8OH\text{-}3$ is directly formed from parent fuel via H abstraction [33] and (ii) C_4H_8 (1-Butene) + H = $C_3H_6 + CH_3$ and $n\text{-}C_3H_7 = C_3H_6 + H$ [39].

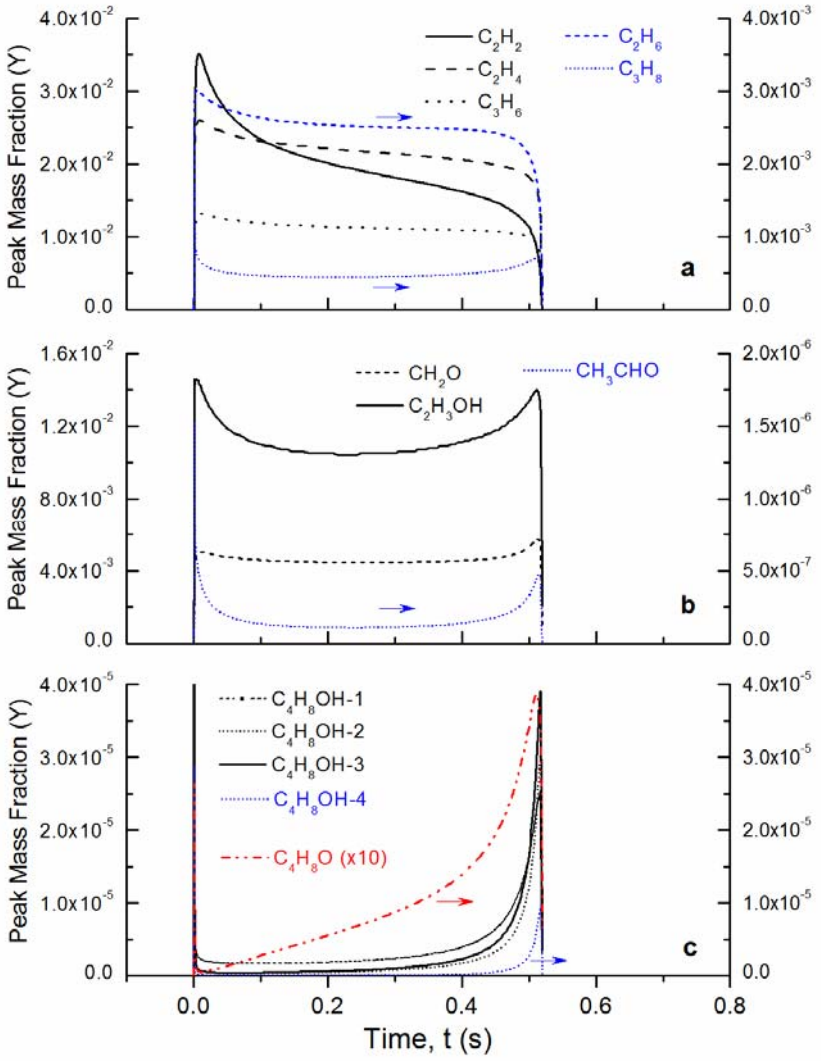

Figure 4.9 Predicted temporal evolution of peak mass fraction of selective species for n-Butanol droplet combustion (D_o = 0.56 mm, 21% O_2/balance N_2, 1 atm).

Ethenol and ethanal are two important isomers of C_2H_4O where ethanal is tautomerized from ethenol. In contrast to the experimental evidence [38] and similar to kinetic modeling observations reported in ref [24], peak concentration of ethenol

(C_2H_3OH) was found to be consistently higher than ethanal throughout the combustion for both the O_2 cases, which implies a lack of characterization of ethenol consumption and/or overestimation of overall flux balance of H-atom abstraction to αcarbon (Figure 4.8 and Figure 4.9).

C_2H_3OH is formed via two major channels $C_4H_8OH\text{-}1 = C_2H_3OH + C_2H_5$ and $pC_2H_4OH = C_2H_3OH + H$, where C_4H_8OH-1 is formed by H-abstraction of n-Butanol and pC_2H_4OH is majorly formed by the decomposition of C_4H_8OH-4. And, the predicted peak mass fraction of CH_3CHO is seen to be significantly lower for X_{O2} = 21%. However, for X_{O2} = 13%, the concentration of ethenol is reduced by ~40% probably because of the slower burning rate at X_{O2} = 13% condition decreases the fuel evaporation rate, which leads to a decrease in C_4H_8OH concentration. Formaldehyde is believed to form primarily through two main pathways: (i) 'H-abstraction' following β-scission of C_4H_9O (directed from fuel) [24, 26]; (ii) from n-butoxy radical [14]. As the droplet shrinks (for a given X_{O2}) or with the change in O_2 concentration, the CH_2O profiles remain unaltered suggesting the lower probability of the first type of reaction pathway for sphero-symmetric droplet combustion environment.

C_4H_8OH is formed by H-abstraction of parent fuel molecule by H-atom and methyl radical, which subsequently decomposes to C_4H_8O and other species [33]. It was reported that β-scission of 1-hydroxybutyl radical is the exclusive route to butanal [14, 15], while Sarathy et al. [24] advocate β-scission of n-butoxy radical as the important route. Harper et al. [33] found that assisted elimination reaction of 1-hydroxybutyl by atomic O is important for butanal formation. Alternately, Sarathy et al. also proposed butanal/butanone production via $C_4H_8OH\text{-}1 + O_2 = n\text{-}C_3H_7CHO + HO_2$, at relatively low temperature

conditions and higher O_2 concentration [38]. Comparing Figure 4.8 (c) and Figure 4.9 (c) it can be seen that the peak C_4H_8O (butanal) increases by a factor of ~2.4 (~ 9.6/4.0) when the droplet burns in a lower O_2 condition which is a consequence of the low flame temperature. The peak butanal concentration is also observed to increase steadily and almost linearly during the entire burn process at low oxygen concentration. These trends of butanal species concentration at low Damköhler numbers are similar to that observed in opposed flow diffusion flame configuration.

4.6 CONCLUDING REMARKS

Spherically symmetric, isolated n-Butanol droplet combustion has been studied experimentally and numerically. The n-Butanol data are compared against predictions from a comprehensive numerical model of droplet combustion, employing both a detailed and reduced kinetic model. The experiments show no presence of a soot shell during the combustion process and droplets are observed to burn to completion unlike other smaller C_1–C_3 alcohols. Predictions from the numerical model are in favorable agreement with the experimental measurements for both models showing complete combustion and no flame extinction. Additionally, it was found that the detailed and reduced kinetic models have minimal differences in predictions for their high-temperature kinetic reaction schemes; ~3% variation in the average burning rate and ~40 K difference in the peak gas temperature.

To further elucidate the flame structure and kinetic effects, simulations are conducted over a broad range of oxygen concentration to identify the limiting oxygen index and variation of the droplet extinction diameter. The numerical analysis predicts that for sub-millimeter sized n-Butanol droplets, the limiting oxygen index is as low as 10%

suggesting that flame extinction for n-Butanol is unlikely in practical applications. Analysis of the kinetics within the droplet flame structure shows that n-Butanol produces significant amounts of C_2, C_3 stable intermediates as well as comparable amounts of formaldehyde, acetaldehyde and vinyl alcohol. The peak acetylene concentration is found higher only during the early stages of the burn and drastically reduces as the quasi-steady burning is achieved – thereby reducing the possibility of any soot or soot shell structure formation. For cases where extinction of the flame occurs, a steady buildup of the large fuel fragments (i.e. C_4H_8OH-3, C_4H_8OH-2, and C_4H_8OH-4) are observed.

4.7 REFERENCES

[1] B.E. Poling, J.M. Prausnitz, J.P. O'Connell, The properties of gases and liquids, McGraw Hill Company, 2001.

[2] B.G. Harvey, H.A. Meylemans, The role of butanol in the development of sustainable fuel technologies, Journal of Chemical Technology & Biotechnology, 86 (2011) 2-9.

[3] C. Jin, M. Yao, H. Liu, C.-f.F. Lee, J. Ji, Progress in the production and application of n-butanol as a biofuel, Renewable and Sustainable Energy Reviews, 15 (2011) 4080-4106.

[4] C.K. Law, Fuel Options for Next-Generation Chemical Propulsion, AIAA Journal, 50 (2012) 19-36.

[5] D. Healy, H.J. Curran, J.M. Simmie, D.M. Kalitan, C.M. Zinner, A.B. Barrett, E.L. Petersen, G. Bourque, Methane/ethane/propane mixture oxidation at high pressures and at high, intermediate and low temperatures, Combustion and Flame, 155 (2008) 441-448.

[6] T. Lu, C.K. Law, On the applicability of directed relation graphs to the reduction of reaction mechanisms, Combustion and Flame, 146 (2006) 472-483.

[7] E.R. Ritter, J.W. Bozzelli, THERM: Thermodynamic property estimation for gas phase radicals and molecules, International Journal of Chemical Kinetics, 23 (1991) 767-778.

[8] X. Gu, Z. Huang, Q. Li, C. Tang, Measurements of Laminar Burning Velocities and Markstein Lengths of n-Butanol−Air Premixed Mixtures at Elevated Temperatures and Pressures, Energy & Fuels, 23 (2009) 4900-4907.

[9] P. Dagaut, C. Togbé, Oxidation kinetics of butanol–gasoline surrogate mixtures in a jet-stirred reactor: Experimental and modeling study, Fuel, 87 (2008) 3313-3321.

[10] P. Dagaut, C. Togbé, Experimental and Modeling Study of the Kinetics of Oxidation of Butanol−n-Heptane Mixtures in a Jet-stirred Reactor, Energy & Fuels, 23 (2009) 3527-3535.

[11] P. Dagaut, S.M. Sarathy, M.J. Thomson, A chemical kinetic study of n-butanol oxidation at elevated pressure in a jet stirred reactor, Proceedings of the Combustion Institute, 32 (2009) 229-237.

[12] S.M. Sarathy, M.J. Thomson, C. Togbé, P. Dagaut, F. Halter, C. Mounaim-Rousselle, An experimental and kinetic modeling study of n-butanol combustion, Combustion and Flame, 156 (2009) 852-864.

[13] P. Dagaut, C. Togbé, Experimental and modeling study of the kinetics of oxidation of ethanol-n-heptane mixtures in a jet-stirred reactor, Fuel, 89 (2010) 280-286.

[14] G. Black, H.J. Curran, S. Pichon, J.M. Simmie, V. Zhukov, Bio-butanol: Combustion properties and detailed chemical kinetic model, Combustion and Flame, 157 (2010) 363-373.

[15] J.T. Moss, A.M. Berkowitz, M.A. Oehlschlaeger, J. Biet, V. Warth, P.-A. Glaude, F. Battin-Leclerc, An Experimental and Kinetic Modeling Study of the Oxidation of the Four Isomers of Butanol, The Journal of Physical Chemistry A, 112 (2008) 10843-10855.

[16] S.M. Sarathy, M.J. Thomson, W.J. Pitz, T. Lu, An experimental and kinetic modeling study of methyl decanoate combustion, Proceedings of the Combustion Institute, 33 (2011) 399-405.

[17] H. Wang, R. Deneys Reitz, M. Yao, B. Yang, Q. Jiao, L. Qiu, Development of an n-heptane-n-butanol-PAH mechanism and its application for combustion and soot prediction, Combustion and Flame, 160 (2013) 504-519.

[18] A.A. Amsden, KIVA-3V: A block-structured KIVA program for engines with vertical or canted valves, in, Los Alamos National Lab., NM (United States), 1997.

[19] W.A. Sirignano, Fluid dynamics and transport of droplets and sprays, Cambridge University Press, 2010.

[20] A. Cuoci, M. Mehl, G. Buzzi-Ferraris, T. Faravelli, D. Manca, E. Ranzi, Autoignition and burning rates of fuel droplets under microgravity, Combustion and Flame, 143 (2005) 211-226.

[21] T. Farouk, F.L. Dryer, Microgravity droplet combustion: effect of tethering fiber on burning rate and flame structure, Combustion Theory and Modelling, 15 (2011) 487-515.

[22] T. Farouk, F.L. Dryer, Tethered methanol droplet combustion in carbon-dioxide enriched environment under microgravity conditions, Combustion and Flame, 159 (2012) 200-209.

[23] T.I. Farouk, Y.C. Liu, A.J. Savas, C.T. Avedisian, F.L. Dryer, Sub-millimeter sized methyl butanoate droplet combustion: Microgravity experiments and detailed numerical modeling, Proceedings of the Combustion Institute, 34 (2013) 1609-1616.

[24] S.M. Sarathy, S. Vranckx, K. Yasunaga, M. Mehl, P. Oßwald, W.K. Metcalfe, C.K. Westbrook, W.J. Pitz, K. Kohse-Höinghaus, R.X. Fernandes, H.J. Curran, A comprehensive chemical kinetic combustion model for the four butanol isomers, Combustion and Flame, 159 (2012) 2028-2055.

[25] Y.C. Liu, C.T. Avedisian, A comparison of the spherical flame characteristics of sub-millimeter droplets of binary mixtures of n-heptane/iso-octane and n-heptane/toluene with a commercial unleaded gasoline, Combustion and Flame, 159 (2012) 770-783.

[26] S. Nakaya, K. Fujishima, M. Tsue, M. Kono, D. Segawa, Effects of droplet diameter on instantaneous burning rate of isolated fuel droplets in argon-rich or carbon dioxide-rich ambiences under microgravity, Proceedings of the Combustion Institute, 34 (2013) 1601-1608.

[27] C.T. Avedisian, J.C. Yang, C.H. Wang, On Low-Gravity Droplet Combustion, Proceedings of the Royal Society of London. A. Mathematical and Physical Sciences, 420 (1988) 183-200.

[28] C.T. Avedisian, B.J. Callahan, Experimental study of nonane/hexanol mixture droplet combustion without natural or forced convection, Proceedings of the Combustion Institute, 28 (2000) 991-997.

[29] Y.-C. Liu, Droplet Combustion Of Surrogate And Real Fuel Systems In A Low Convection Condition: Ground-Based And Space-Based Experiments, in, 2013.

[30] C.L. Dembia, Y.C. Liu, C.T. Avedisian, AUTOMATED DATA ANALYSIS FOR CONSECUTIVE IMAGES FROM DROPLET COMBUSTION EXPERIMENTS, Image Analysis & Stereology; Vol 31, No 3 (2012), (2012).

[31] T.E. Daubert, R.P. Danner, Physical and Thermodynamic Properties of Pure Chemicals: Supplement 4, Hemisphere Publishing Corporation, 1994.

[32] S. Vranckx, K.A. Heufer, C. Lee, H. Olivier, L. Schill, W.A. Kopp, K. Leonhard, C.A. Taatjes, R.X. Fernandes, Role of peroxy chemistry in the high-pressure ignition of n-butanol – Experiments and detailed kinetic modelling, Combustion and Flame, 158 (2011) 1444-1455.

[33] M.R. Harper, K.M. Van Geem, S.P. Pyl, G.B. Marin, W.H. Green, Comprehensive reaction mechanism for n-butanol pyrolysis and combustion, Combustion and Flame, 158 (2011) 16-41.

[34] S.R. Turns, An Introduction to Combustion: Concepts and Applications, McGraw Hill Higher Education, Singapore, 2006.

[35] J. Li, Z. Zhao, A. Kazakov, M. Chaos, F.L. Dryer, J.J. Scire, A comprehensive kinetic mechanism for CO, CH2O, and CH3OH combustion, International Journal of Chemical Kinetics, 39 (2007) 109-136.

[36] M.P. Burke, M. Chaos, Y. Ju, F.L. Dryer, S.J. Klippenstein, Comprehensive H2/O2 kinetic model for high-pressure combustion, International Journal of Chemical Kinetics, 44 (2012) 444-474.

[37] F.M. Haas, M. Chaos, F.L. Dryer, Low and intermediate temperature oxidation of ethanol and ethanol–PRF blends: An experimental and modeling study, Combustion and Flame, 156 (2009) 2346-2350.

[38] N. Hansen, M.R. Harper, W.H. Green, High-temperature oxidation chemistry of n-butanol - experiments in low-pressure premixed flames and detailed kinetic modeling, Physical Chemistry Chemical Physics, 13 (2011) 20262-20274.

[39] J. Cai, L. Zhang, F. Zhang, Z. Wang, Z. Cheng, W. Yuan, F. Qi, Experimental and Kinetic Modeling Study of n-Butanol Pyrolysis and Combustion, Energy & Fuels, 26 (2012) 5550-5568.

CHAPTER 5

COMBUSTION CHARACTERISTICS OF BUTANOL ISOMERS IN MULTIPHASE DROPLET CONFIGURATIONS

5.1 ABSTRACT

This chapter reports the results of experiments on the isolated droplet burning characteristics of butanol isomers (n-, iso-, sec-, and tert-) under standard atmosphere conditions in an environment that promotes spherical combustion. The data are compared with predictions from a detailed numerical model (DNM) that incorporates complex combustion chemistry, radiative heat transfer, temperature dependent variable fluid properties, and unsteady gas and liquid transport. Computational predictions are generated using the high-temperature kinetic models of Sarathy et al. (2012) and Merchant et al. (2013). The experiments are performed in a free-fall facility to reduce the effects of buoyancy and produce spherical droplet flames. The motion of single droplets with diameters ranged from 0.52 mm to 0.56 mm was eliminated by tethering them to two small-diameter SiC filaments (d ~14 μm diameter). In all the experiments, minimal sooting is observed, offering the opportunity for direct comparison of the experimental measurements with DNM predictions that neglect soot kinetics. The experimental data showed that the burning rates of iso- and sec-butanol are very close to that of n-butanol, differing only in flame structure. The flame stand-off ratios (FSR) for n-butanol flames are smaller than those for the isomers, while tert-butanol flames exhibited the largest FSR. DNM predictions based on the kinetic model of Sarathy et al. over-predict the droplet burning rates and FSRs of all the isomers except n -butanol. Predictions using a kinetic model based on the work of Merchant et al. agree much better with the experimental data, though relatively higher discrepancies are evident for tert-butanol

simulation results. Further analyses of the predictions using the two kinetic models and their differences are discussed. It is found that the disparity in transport coefficients for isomer specific species for Sarathy et al. model fosters deviation in computational predictions against these newly acquired droplet combustion data presented in this study.

5.2 INTRODUCTION

Liquid fuels have been widely used to power aerospace and ground transportation vehicles. Despite projected decreases in petroleum resources in the future, forecasts suggest that demand for liquid transportation fuel will continue to grow. Liquid fuels are preferred over other forms due to their high energy content, matured engine technologies that utilize them, and fuel manufacturing/distribution infrastructure [1]. In particular, sustainable liquid fuels derived from biomass (biofuels) have demonstrated potential to be used to augment petroleum-derived resources through blending. Creating a self-sustaining, profitable biofuels industry that does not compete with agricultural food supply is a challenge recognized by government mandates in the U.S. and the European Union.

Butanol (C_4H_9OH), as an emerging biofuel, has been identified because of the readiness and continuous development of conversion processes for biomass feedstocks [2]. Selected properties of butanol isomers are shown in Table 5.1 [3-5]. Butanol isomers have comparatively superior fuel properties, e.g., higher energy density, lower vapor pressure, less corrosive compared to ethanol [5] and also have been considered for use in commercial compression ignition (CI) engines due to their relatively high cetane number [6, 7].

Table 5.1 Selected fuel properties of butanol isomers (M.W. = 78.123 g/mole [7])

	n-butanol	iso-butanol	sec-butanol	tert-butanol
Molecular structure				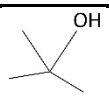
Liquid density (kg/m^3), ρ at 298 K[a]	0.81	0.802	0.807	0.787
Liquid viscosity (mPa-s), μ at 298 K[b]	2.544	4.312	3.096	-[d]
Boiling point, T_b (K) [a]	390.9	381	372.7	355.6
Freezing point T_{fr} (K) [a]	183.9	165.2	158.5	298.8
Critical pressure, P_c (atm) [a]	43.6	42.4	41.4	39.2
Research octane number [b]	96	113	101	105
Motor octane number[b]	78	94	32	89
Enthalpy of vaporization, H_f (kJ/kg)	582	566	551	527
Heat of combustion, $H_{c,liq}$ (kJ/kg) [c]	-36087	-36001	-35895	-35669

[a][4] [b][5] [c] values converted from [3] [d]tert-butanol is solid at 298 K.

The interests in butanol have attracted much effort towards engine studies. The performance and emission behaviors of both spark ignition (SI) and compression ignition (CI) engines fueled by blends of petroleum fuels and n-butanol have been extensively reported [8-14]. The addition of n -butanol was found to increase the brake specific fuel consumption (bsfc) and brake thermal efficiency [10] and slightly reduce CO and NO_x emissions [9] of diesel engines except for turbo-charged operations [13, 14]. In a direct injection SI engines, n-butanol/gasoline blends promote better anti-knock behaviors and reduction of CO, NO_x and unburned hydrocarbons (UHC) [8]. Pure n-butanol combustion has been reported in some homogeneous charged CI (HCCI) engine studies [15] and it could increase CO and unburnt hydrocarbon (UHC) emissions compared to gasoline in SI

engine operations [11]. Regalbuto et al. [12] reported that among butanol isomers, n-butanol exhibits the highest NO_x, iso-butanol the highest CO, and sec-butanol the highest UHC in SI engine experiments.

Oxidation kinetics of butanol isomers have received attention since about a decade ago [16, 17]. Development of combustion chemistry of butanol isomers includes a direct comparison with combustion properties measured in configurations that are amenable to detailed numerical modeling (DNM). Currently, such modeling has been widely performed for configurations in which the fuel is pre-vaporized (e.g., jet-stirred reactor (JSR) [18-20], shock tubes [21-24], rapid compression machines/facility (RCM/RCF) [25, 26], opposed diffusion flame burner [27-29], flow reactors [29, 30] and pyrolysis reactor and premixed flame probed by a molecular beam mass spectroscopy (MBMS) [17, 30-33]. Recently, Sarathy et al. [34] utilized experimental results from MBMS, shock tube, RCM, and JSR configurations to validate a comprehensive oxidation kinetics model for butanol isomers that cover high and low-temperature ranges. Van Geem and coworkers [35], Harper et al. [36] and Merchant et al. [37] validated the mechanisms for n-, sec-, iso- and tert-butanol pyrolysis and/or oxidation with combustion properties from JSR, opposed flame, laminar flame velocity, and shock tube configurations. This kinetic model has been used in simulating the combustion in more practical systems like a homogeneous charge compression ignition (HCCI) engine [38].

Non-premixed liquid pool ignition experiments [39] of n-butanol and iso-butanol have been modeled using a reduced version [40] of n-butanol oxidation scheme by Sarathy et al. [19] coupled with phase equilibrium parameters. Soot prediction from n-heptane/n-butanol/PAH mechanisms has also been pursued [41]. However, the

performance of the kinetic models developed has not yet been assessed in detailed numerical models of multi-phase combustion configurations that, at the least, may be considered to provide a bridge to spray combustion.

An important attribute of combustion properties obtained from the experimental configurations mentioned above for validating detailed kinetic mechanisms is that those configurations promote a zero or one-dimensional transport process because doing so significantly reduces computational overhead for modeling while incorporating detail chemistry. However, none of them includes some of the unique multiphase features found in a spray, including fuel vaporization, coupled liquid and vapor transport, moving boundary effects, or the sub-grid spray configuration of droplets. Currently, the only combustion configuration that is amenable to detailed numerical modeling which does incorporate such elements is a single isolate droplet burning with spherical symmetry [42-48] such that the droplet and flame are concentric and gas transport is radially symmetric. This chapter discusses the modeling capability to combustion of butanol isomer droplets under conditions that promote such spherical symmetry.

Experimental studies are noted on butanol isomer droplets at standard [47] and elevated pressures [42, 49, 50] as well as under various ambient temperatures [51]. Pure evaporation of n-butanol droplets has also been studied [52]. The present study is motivated by the dearth of data for butanol isomers droplet combustion specifically under conditions that promote spherical droplet flames to simplify the transport processes involved as well as representing a multi-phase combustion system. The predicted combustion properties using DNM (described in chapter 2) are compared with measurements. Building upon the prior work on n-butanol [47], the present study shows

both experimental and numerical comparison of droplet burning of all four butanol isomers.

5.3 KINETIC MODELS

The present study adopts the thermodynamic parameters, chemical kinetic mechanisms, and transport properties from two separate kinetic sources: 1) Sarathy et al. [34]: abbreviated here as 'LLNL (Lawrence Livermore National Lab)' model; 2) Merchant et al. [37]: the MIT model developed and timely updated by Green and coworkers. The LLNL model used in this paper includes 284 combustion species and 1892 reactions (the high-temperature scheme). The MIT model employed here is the Chemkin-II compatible version of Merchant et al. [37] obtained through Green's group at MIT that includes 337 species and 7121 reactions (other than the 373 species and 8723 reactions originally claimed in Ref. [37]).

For the simulation, the innermost liquid node is centered at the origin, providing the required no-flux condition. The liquid and gas phase mesh size for all the simulations for LLNL and MIT model are respectively 40 and 30, and 120 and 80. The hardware resources deployed for these simulations are Intel 16 CPU cores (2.4 GHz) with 96 GB of memory allocation. Typical simulation runtime of converged solution for LLNL and MIT model is respectively 50–53 CPU hours and 160–167 CPU hours. The gas phase domain is set as 200 times larger than the initial droplet size and the applied spark ignition energy input in the model is around 1 J, which is the lowest possible energy that numerically triggered a series of combustion reactions for both the models.

5.4 RESULTS AND DISCUSSION

5.4.1 DROPLET COMBUSTION FLAME IMAGING

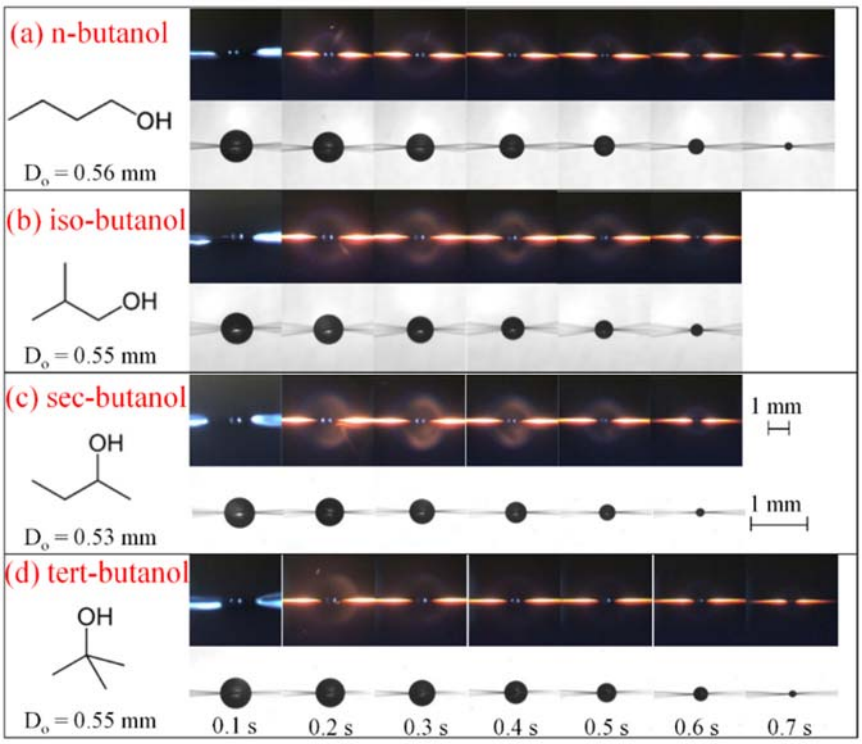

Figure 5.1 Flame and droplet images obtained from droplet burning experiments for (a) n-butanol [47], (b) iso-butanol, (c) sec-butanol, (d) tert-butanol. Courtesy- Professor C. T. Avesidian, Cornell University, NY, USA.

Representative images from the droplet burning histories of different butanol isomers are shown in Figure 5.1. The upper row in each box shows self-illuminated flame images that highlight the flame structure while the second rows are backlit images of the droplet boundary. Droplet flame of n-butanol (cf. Figure 5.1 (a)) maintained bluish flame almost all the time with the yellow glows caused by the fiber. The iso-butanol and sec-butanol droplet flame (cf. Figure 5.1 (b) and (c)) appear to produce a brighter yellow core among the four isomers that are enclosed by a pure blue zone. The flame produced by tert -butanol droplet (cf. Figure 5.1d) is as bright as those produced by iso- and sec-butanol

but that yellow core quickly dies out after 0.4 s. Though soot aggregates (i.e., a soot 'shell') were not visibly seen in the black and white (BW) images, the yellow core could nonetheless suggest possible soot related intermediates that are consumed in-situ after they are being produced. The following discussion compares experimental data of droplet and flame diameters with DNM predictions.

5.4.2 DROP TOWER EXPERIMENTAL RESULTS OF BUTANOL ISOMERS

Figure 5.2 includes the droplet burning histories (D^2 vs. time, t; both scaled by the square of initial droplet diameter D_o^2) obtained from three individual experiments for each of the four butanol isomers. Four different colors, i.e. red, black, blue and green are used in Figure 5.2 and all the figures hereafter (except for the modeling results in Figure 5.4) to represent different isomers. It is suggested in Figure 5.2 that the experimental data are evidently very reproducible. Averaged data for each isomer are shown in Figure 5.2 (b). The slopes of the data represent the droplet burning rate $K_b = -d\left(\frac{D}{D_o}\right)^2 \Big/ d\left(\frac{t}{D_o{}^2}\right)$. The evolutions of droplet diameter for n-, iso-, and sec-butanol are almost identical. The burning rate of tert-butanol is lower, which is believed not to be the result of the slightly smaller initial droplet diameter of tert-butanol compared to the other isomer droplets. The relative burning rates qualitatively correspond to the heat of combustion of the isomers (cf. Table 5.1): tert-butanol has the lowest heat of combustion (and lowest burning rates) among all isomers while the other three isomers have closer heat of combustion.

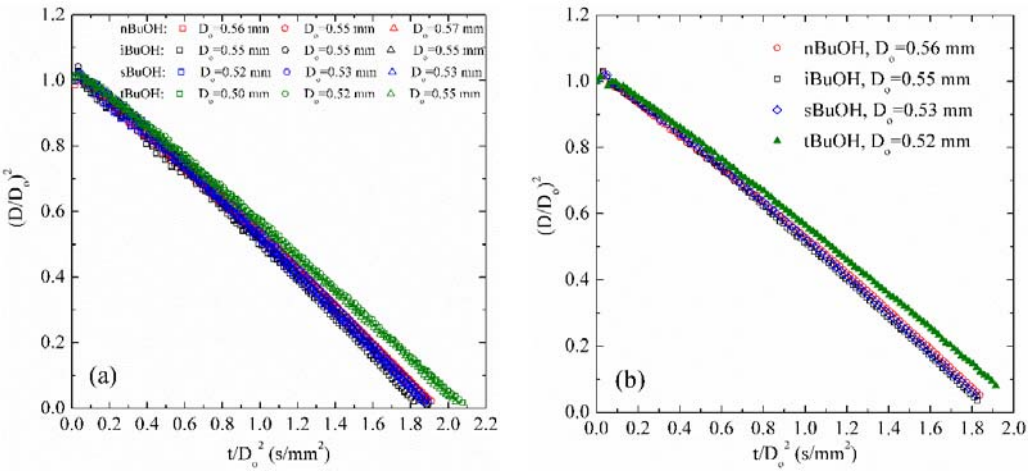

Figure 5.2 Experimental droplet diameter regression data for n-butanol [47], iso-butanol, sec-butanol, and tert-butanol droplets. Subplot (a): three individual runs for each butanol isomers; (b) the average data from (a) for each isomer.

5.4.3 NUMERICAL PREDICTIONS OF DROPLET REGRESSION

Figure 5.3 compares the evolution of D^2 from DNM predictions of the LLNL (dashed lines) and MIT (solid lines) kinetic models for all four isomers. The LLNL mechanism gives significantly higher burning rates (i.e., slopes of the lines in Figure 5.3) for iso-, sec-, and tert-butanol compared to the MIT kinetics, while the MIT mechanism produces D^2 data that are more adjacent to each other. On the other hand, the D^2 evolution of n-butanol predicted by the LLNL and MIT kinetic models agree rather well with each other. The general trend of predicted burning rates seems to be similar for both kinetics, i.e. $K_{tert} > K_{sec} > K_{iso} > K_n$. In this order, the predicted burning rate of tert-butanol is in the opposite trend of the experimental observation (cf. Figure 5.2 (b)): the data show that the burning rate of tert-butanol is significantly lower than that of the other isomers, while the predicted tert-butanol burning rate (Figure 5.3) is higher. From perspective of the D^2-law, it has been previously suggested that the burning rate (K_b) is proportional to a parameter $\xi = k_g/(\rho_l * C_{p,g})$ [53] where k_g is the thermal conductivity

of gas, ρ_l is the liquid density, $C_{p,g}$ is the specific heat of gas. It is found that $C_{p,g}$ of tert-butanol is noticeably higher than those of other isomers from various sources including the thermal property data of the MIT model [37] and Ref. [4] in the range of 1200 - 1700 K, and therefore speculated to be a factor of tert-butanol's lowest burning rate. Note that the thermal property data appended to the LLNL model [34] produce almost the same values of $C_{p,g}$ for all four isomers. Therefore care should be exercised using the D^2-law and physical properties to provide estimate of burning rates, especially for isomeric comparisons where values of physical properties are relatively close and slight variation from the model may lead to a different direction of discussions.

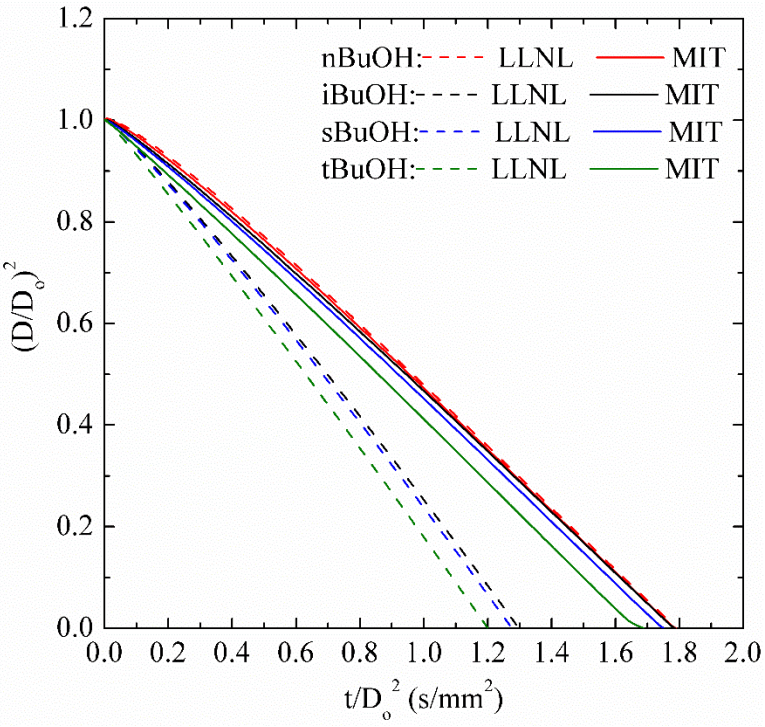

Figure 5.3 Numerical prediction of droplet diameter regression for four butanol isomers using Sarathy et al. [34] (dashed line) and Merchant et al. [37] (solid line) kinetic models. Initial droplet diameter: n-butanol (0.56 mm), iso-butanol (0.55 mm), sec-butanol (0.53 mm), and tert-butanol (0.52 mm). Ambient condition: P = 1 atm, T = 298 K.

5.4.4 COMPARISON OF DROPLET COMBUSTION EXPERIMENTS AND PREDICTIONS

To provide clear comparisons with the experimental results, Figure 4 (a)-(d) compares the predicted droplet diameters with measured values (cf. Figure 2 (b)) using the LLNL (dash red lines) and MIT (solid black lines) kinetic models. The experimental data shown in these plots include the error bars showing the standard deviations computed from three individual experiments (cf. Figure 2 (a)). For n-butanol (Figure 4 (a)), the D^2 predictions using both models yielded similar burning curves with the absolute $(D/D_o)^2$ values slightly smaller than the experimental values. Though the absolute droplet diameter values from DNM are below the error bars, the slope (burning rates) near the end are very similar to experimental results. This would suggest that the slight discrepancy may stem from the earlier stage of the combustion process (i.e. $t/D_o^2 < 0.8$ s/mm^2).

Figure 5.4 (b) and (c) suggest that the MIT model better predicts the iso- and sec-butanol data compared to the LLNL model, which reflects the extensive validation of the MIT model with gas phase sec- and iso-butanol combustion properties. It is clear that the droplet diameters predicted using the LLNL model are significantly smaller than the measurements for iso-, sec- and tert-butanol while predictions from the MIT model are relatively better matched with the data (Figure 5.4 (b)-(d)). Furthermore, burning rates (slope of the data) predicted from the MIT kinetic model are in reasonable agreement with the experimental results for iso- and sec-butanol.

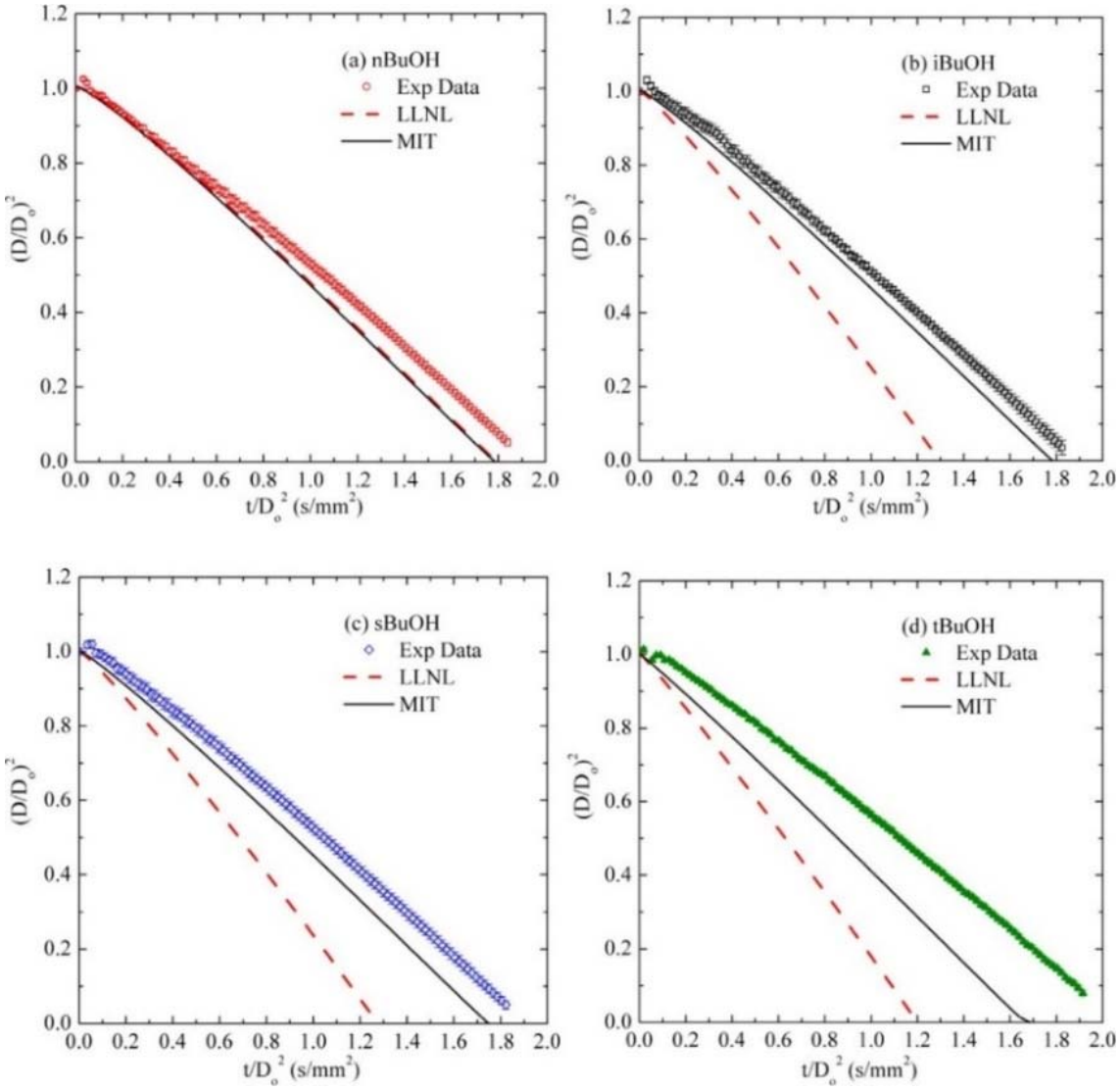

Figure 5.4 Comparison of experimental data and numerical modeling results of droplet diameter regression for (a) n-butanol, (b) iso-butanol, (c) sec-butanol, and (d) tert-butanol. Initial droplet diameter: n-butanol (0.56 mm), iso-butanol (0.55 mm), sec-butanol (0.53 mm), and tert-butanol (0.52 mm). Ambient condition for simulation: P = 1 atm, T = 298 K.

The numerical predictions for tert-butanol from both models (Figure 5.4 (d)) do not agree well with the data, though the MIT model is much closer to the measurements. Even considering validations of these kinetic models against premixed experimental combustion targets, both the LLNL and MIT models were found to not be in especially good agreement [16, 17]. This suggests that there are possible limitations in the kinetic

schemes due to limited insight into the mechanistic pathways associated with combustion of tert-butanol. Notably, from here onwards, the primary objective of this study will be to extensively investigate sec-, iso - and tert-butanol droplet combustion. Therefore subsequent discourse is mainly directed towards these isomers essentially precluding the already studied n -butanol [47].

The numerical predictions of instantaneous burning rate and peak gas temperature profiles for sec-, iso- and tert-butanol deploying both the chemical kinetic models are presented in Figure 5.5. In addition, the droplet burning rate calculated from the experimental dataset, delineated by solid symbol, is juxtaposed in respective subplots (Figure 5.5 (a)–(c)). As shown in the figure, predictions from Sarathy et al. (i.e., LLNL model) has a consistently higher burning rate for all the isomers compared to Merchant et al. (i.e., MIT model) predictions. Interestingly, opposite to the experimental observation, there is no 'quasi-steady state' burning period for the LLNL model. Instead, irrespective of the isomers, the model exhibits continuously increasing burning rate trend. All three isomers behave in a near-identical fashion with a sudden dip in the burning rate at the end indicating flame-out due to fuel depletion. In contrast, predictions from MIT model qualitatively regenerate the experimental profile and quantitatively reproduce the experimental observation, especially for sec- and iso-butanol though discrepancy is discernible for tert-butanol indicating faster burning rate. This also suggests that there is room for model refinement for the tert-butanol. A closer look at the tert-butanol burning rate also reveals that Merchant et al. predicts a flame extinction at the very last stage of the burn period.

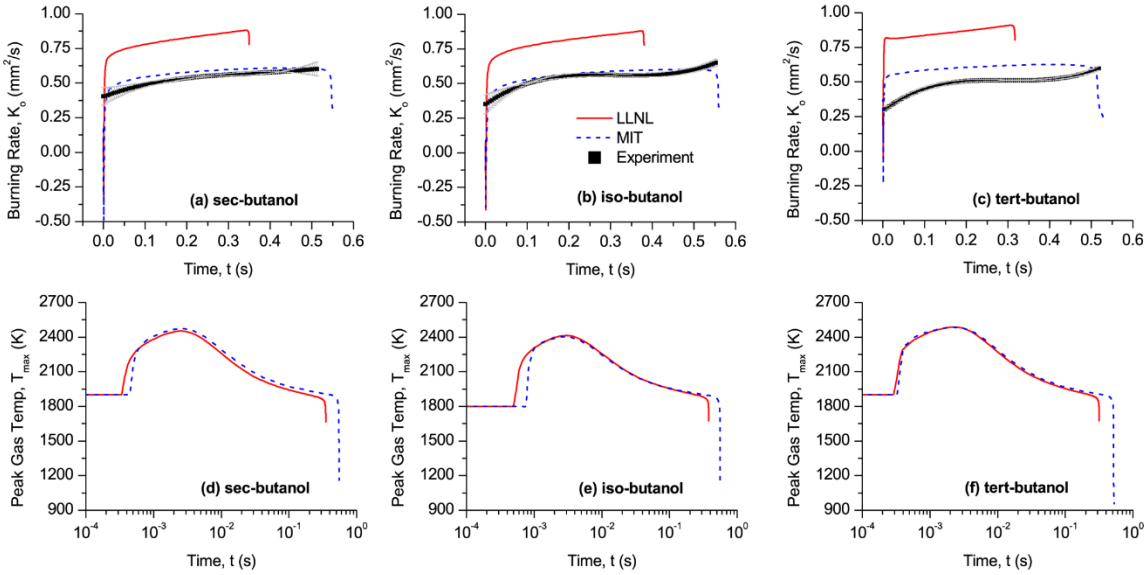

Figure 5.5 Comparison of instantaneous burning rate (top row) and peak gas temperature (bottom row) comparison for Sarathy et al. [34] (solid red) and Merchant et al. [37] (dashed blue) kinetic models for different butanol isomers. Subplot (a) and (d): sec-butanol, subplot (b) and (e): iso-butanol, and subplot (c) and (f) tert-butanol. The symbol in the top row (black square) represents experiment data with associated error bars (gray). Initial droplet diameter: n-butanol (0.56 mm), iso-butanol (0.55 mm), sec-butanol (0.53 mm), and tert-butanol (0.52 mm). Ambient condition for simulation: P = 1 atm, T = 298 K.

In the same figure, subplots (d–f) in Figure 5.5 illustrates a direct comparison of the temporal evolution of peak gas temperature for both these models for three different isomers. Notably, for an individual isomer, respective simulations are performed under the same level of initial ignition energy. It is perceptible from the figure that the LLNL model ignition chemistry for each of the isomers is more sensitive than its counterpart model. Therefore, the rise in temperature for LLNL model is consistently earlier than that of MIT model. Surprisingly, immediately after the ignition transient, both the model approaches to the same maximum temperature throughout the lifetime of the burning droplet (i.e., at least till LLNL model predicted lifetime), both profiles remain almost the same except the flame-out phase. Given that the LLNL model prediction for the average burning rate is approximately 50% higher than the MIT prediction while both the models

simulated the same peak gas temperature profile (until flame-out dynamics commences), possibly suggesting that the LLNL flame location is positioned more outward radial position than MIT prediction. Thus, as a logical consequence, the following section includes the discussion on flame stand-off ratio (D_f / D_d). As the MIT model is found to be a more accurate representation of butanol isomer kinetics against droplet combustion experiments, by implying comparison-it is discernible that all the butanol isomers produce near identical peak gas temperature profile indicative of similar flame/reaction zone temperature for the high-temperature kinetic regime.

5.4.5 ANALYSIS OF FLAME EVOLUTION

Figure 5.6 (a) and (b) shows the evolution of FSR for butanol isomers where Figure 5.6 (a) showing the data from all individual experiments and Figure 5.6 (b) the averaged data. It is noticed from Figure 5.6 (a) that the n-butanol data are more scattered after t/D_o^2 = 1.0 s/mm^2 because it was slightly more difficult to pinpoint the flame boundary of the small bluish flame, especially in a dark background. In general, the data in Figure 5.6 (a) suggest that the FSR values from experiments are also very repeatable for each fuel. More clear trends of FSR can be found from the averaged data in Figure 5.6 (b). It is evident that n-butanol has the lowest FSR along the combustion history. With the FSR of sec-butanol slightly higher than that of iso-butanol, tert-butanol exhibits the largest FSR among all four isomers. This ordering seems to remain throughout the droplet burning history. The general trend of continuously increasing FSR during the quasi-steady burn is primarily related to the far-field thermal buffering effect [54].

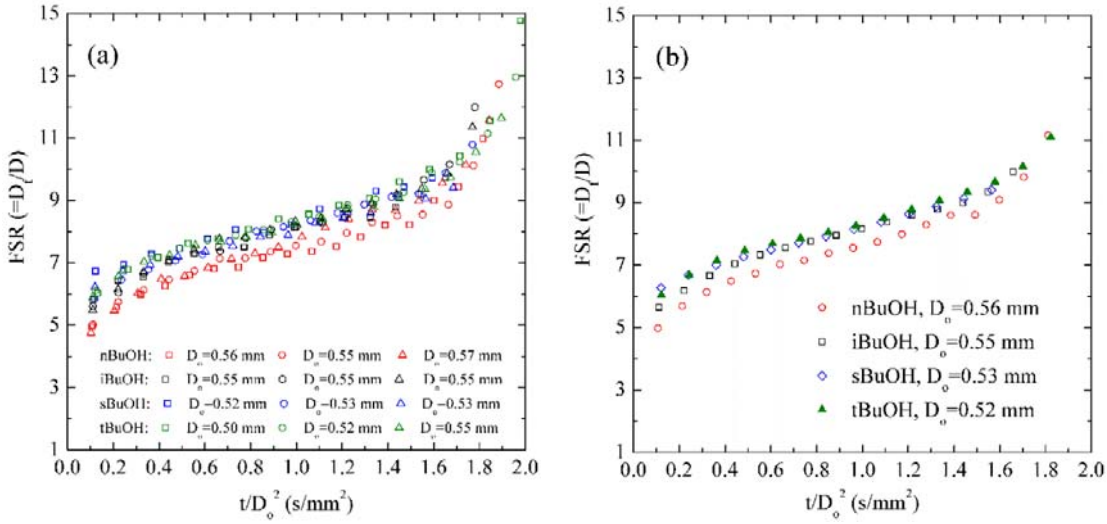

Figure 5.6 Experimental measurement of flame stand-off ratio (FSR) with time for four different butanol isomers. Data for n-butanol are excerpted from external reference [47]. (a) three individual experiments for each butanol isomers and (b) the average from (a) for each isomer.

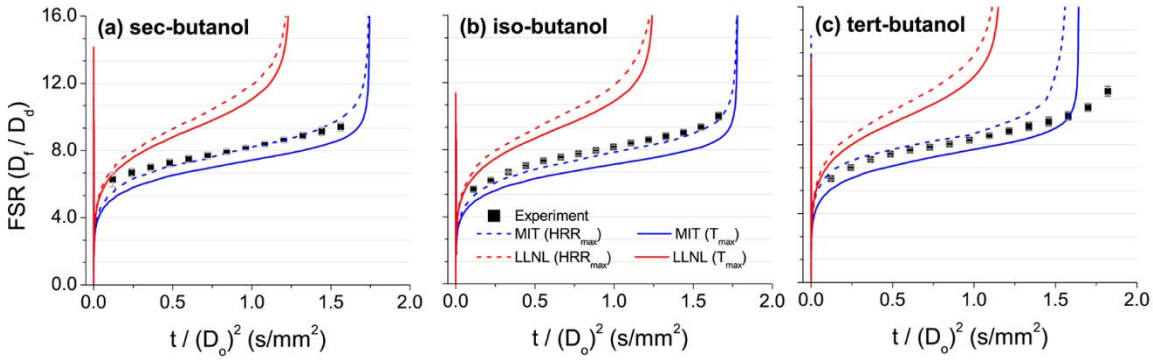

Figure 5.7 Comparison of experimental and computational flame stand-off ratio (FSR = D_f / D) for Sarathy et al. [34] (red lines) and Merchant et al. [37] (blue lines) kinetic models. Solid lines: flame diameter based on the location of peak gas temperature prediction. Dashed line: flame diameter based on the location of maximum heat release rate. Initial droplet diameter: sec-butanol (0.53 mm), iso-butanol (0.55 mm) and tert-butanol (0.52 mm). Ambient condition for simulation: P = 1 atm, T = 298 K.

Figure 5.7 compares the FSR obtained from experiments and DNM predictions using both the LLNL and MIT models for sec-, iso- and tert-butanol. Two different approaches have been adopted for each model in defining the flame kernel position –(i)

location of the peak gas-phase temperature (T_{max}), and (ii) location of the maximum heat release rate (HRR_{max}). The rationale in selecting these two quantities as FSR marker has already been substantiated elsewhere [47, 54]. The experimental data are shown with an error bar representing the standard deviation from individual experiments. These error bars represents an uncertainty that is larger than the uncertainty from flame size measurements (8%) mentioned previously. It is seen from the figure that irrespective of the butanol isomers, all of them show a similar trend in term of FSR evolution. By ignoring the initial ignition transient and flame-out dynamics, their overall values evolve in between ~5.0 and 9.0. Considering that the isomers are of similar initial diameters (0.54 ±0.02 mm) and their FSR evolutions also remain same during the quasi-steady burning (inclusive of slope), it could be inferred that the flame experiences the same level of heat loss and reactant (fuel and/or pyrolyzed fuel fragments) gain from the flame location. Initially, the droplet diameter (D) regresses linearly until (sec-/ iso-/ tert- ~ 44%/ 44%/ 47% of burn time) it starts to regress in nonlinear fashion. Part of this non-linear behavior is spurring from tether fiber additional thermal interaction, especially when the droplet is approaching the fiber diameter size [55]. Simultaneously, for the flame (not shown explicitly in the corresponding figure), it initially grows outwardly, reaches maximum and remains approximately fixed at around that location until the droplet enters the non-linear diameter regression time zone, and then the flame responds back to the shrinking droplet and decreases, albeit at a slower rate (i.e. slope) than the droplet [54]. This two coupled effect of droplet and flame causes the FSR to have an ever so slightly increasing pattern for all the isomers for such sub-millimeter size droplets. For sec-, iso- and tert-butanol isomers, the MIT model correctly simulated the FSR evolution,

especially with HRR_{max} approach. Although the model's prediction capability is laudable for sec- and iso-butanol, disagreement for tert-butanol at the latter part of the burn time is noticeable. Surprisingly, for all the isomers reported here, LLNL model consistently over-predicts the FSR evolution from initial burn time with similar FSR trend throughout its burning period and ultimately exhibiting almost the same extinction/flame-out temporal location ($t/(D_o)^2 \sim 1.20\text{-}1.25$ s/mm^2).

5.4.6 ANALYSIS OF KINETIC MODEL PREDICTION DISCREPANCY

The disparity in LLNL model predictions for FSR renders careful reexamination of the model itself. Both the FSR makers manifest that the flame repositions itself at a farther distance from the initial get-go. Intuitively, two possible explanation could be sought for –(i) inappropriate gas phase kinetics (i.e. rate constants) for isomer specific reactions, and/or (ii) faster transport coefficient. The inappropriate rate constant may possibly lead to excessive fuel decomposition that in turn may enhance excessive heat and temperature evolution. The excessive heat feedback drives the flame to reposition at a farther location which possibly explains the higher FSR. On the other hand, faster transport may disperse the reactive species (pure or decomposed fuel, intermediates, and products) to the far field and also the reaction zone, resulting in higher FSR. In order to better comprehend the influence of the aforementioned two possibilities, spatial-temporal analysis of important parameters (temperature, species mass fraction etc.) are performed in the following section. Finally, in a later part of this chapter, individual influence of thermodynamic properties, transport parameters and kinetic rate coefficients of isomer specific species for LLNL model are benchmarked against MIT counterpart model.

The spatial-temporal evolution of key species and temperature are illustrated in Figures 5.8 and 5.9 for tert-butanol. It should be noted that the location of the flame (i.e. reaction zone) based on maximum temperature is delineated by the white dashed line in these plots. For the sake of direct comparison between the two models, predicted results are exhibited up to 0.3 s. It is clear from the figure that irrespective of the model, the fuel undergoes decomposition from the near-surface location of the droplet. However, the radial zone over which the fuel decomposes (and subsequently disperses) as time progresses varies for the individual model. According to the MIT model, the fuel mass fraction completely vanishes to zero at approximately half the radial distance that is predicted by the LLNL model. The extension of this analysis can be drawn towards the gas phase temperature and final products like carbon monoxide (CO) and carbon dioxide (CO_2). In congruence with earlier analysis, the temperature magnitude of both these models is almost the same including peak gas temperature (subplot Figure 5.8 (b) and (d)). However, the radial distribution significantly differs for both these model predictions. According to the LLNL model, the higher temperature field is diffused outward with time resulting in higher FSR whilst for the MIT model the high-temperature section approaching a near-plateau after ~0.1 s, thus enabling FSR to increase ever so slightly compared to the LLNL model. A similar observation is rendered for final products like CO and CO_2. Although the qualitative agreement is observable for the mass fraction prediction for both these models, the radial spread of each of these species clearly demarcates the underlying differences between these two models. Spatial-temporal analysis for sec- and iso-butanol with similar conclusive observations are also found from our numerical analyses.

The above description clearly highlights the difference between the two models when coupled with multiphase droplet combustion simulation. Intuitively, the disparity between the model predictions may stem from the variations in (i) elementary kinetic reactions and rate coefficients, (ii) thermodynamic property formulations and (iii) transport parameters. It is noteworthy that while the prime objective of the present study is to focus on the butanol isomer droplet combustion, the large prediction discrepancies between these two adopted models also require careful attention for the possible causes of deviation, notably for the LLNL model. The proceeding discussion attempts to explore the contribution of three possible sources of deviation for the LLNL model.

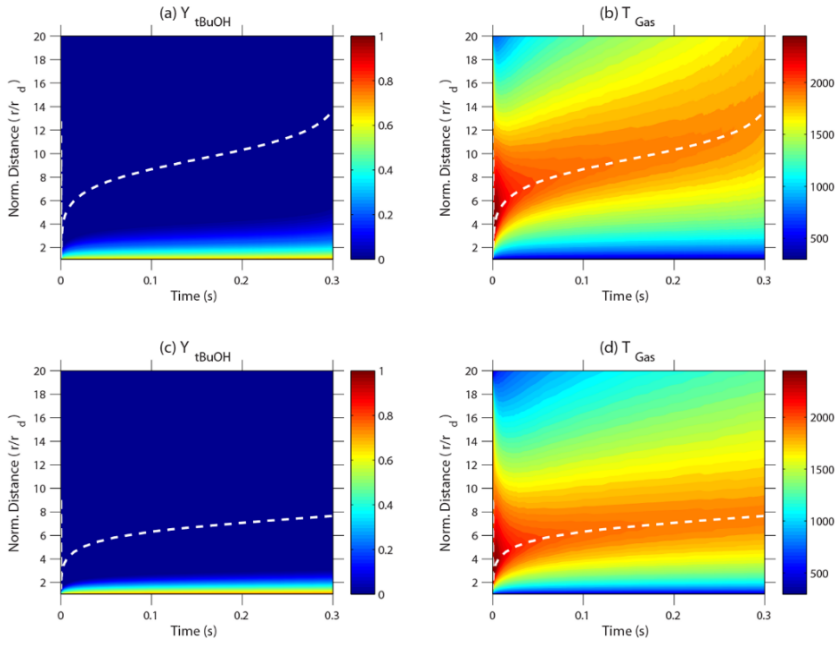

Figure 5.8 Predicted spatiotemporal evolution of fuel mass fraction and gas phase temperature for tert-butanol droplet combustion. Top row: Sarathy et al. (LLNL) [34] and bottom row: Merchant et al. (MIT) [37] kinetic model. The dashed white line is computationally evaluated flame location based on maximum temperature location. Results are reported up to 0.3 s for common comparison. Initial droplet diameter for tert-butanol is 0.52 mm. Ambient condition for simulation: P = 1 atm, T = 298 K.

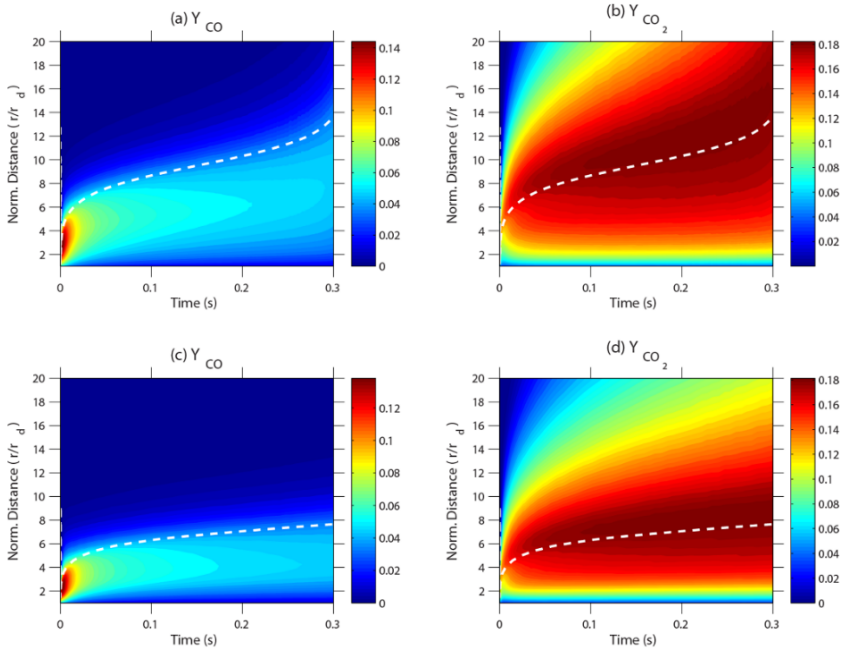

Figure 5.9 Predicted spatiotemporal evolution of carbon monoxide (CO) and carbon dioxide (CO_2) for tert-butanol droplet combustion. Top row: Sarathy et al. [34] (LLNL) and bottom row: Merchant et al. (MIT) [37] kinetic model. The dashed white line is computationally evaluated flame location based on maximum temperature location. Results are reported up to 0.3 s for common comparison. Initial droplet diameter for tert-butanol is 0.52 mm. Ambient condition for simulation: P = 1 atm, T = 298 K.

In this exercise, the previous simulation outcome of MIT model is considered as the base 'result' due to its better predictive capability against drop tower experiments. In actuality, both the models have a different number of species and elementary reactions including the difference in the fuel specific sub-model (e.g. bimolecular reactions for isomer decomposition). To check whether the prediction difference is occurring from thermodynamic or transport property variation, isomer specific common species of LLNL is exchanged with MIT model data. Similarly, common reactions (isomer specific) are interchanged with the MIT model. It should be noted that other species and reactions are not modified in accordance with MIT model. As the main skeletal of both the LLNL and MIT models comprise the n-butanol reaction kinetics, and both models exhibit good

predictions for n-butanol droplet combustion [47], therefore other species and reactions are not interchanged. Subsequently, three individual runs are performed and reported in Figure 5.10 along with experimental measurement only for tert-butanol droplet combustion. As evident in Figure 5.10, reaction kinetics and thermodynamic expression exchange do not contribute to distinguishable difference than its base run reported earlier (cf. Figures 5.4, 5.5 and 5.7). However, for the case of transport property data exchange, the LLNL model prediction reproduces the model prediction of MIT model. This also explains the wider dispersion of species and temperature field as illustrated in Figure 5.8 and even though the peak gas temperature is found to be near-identical (cf. Figure 5.5).

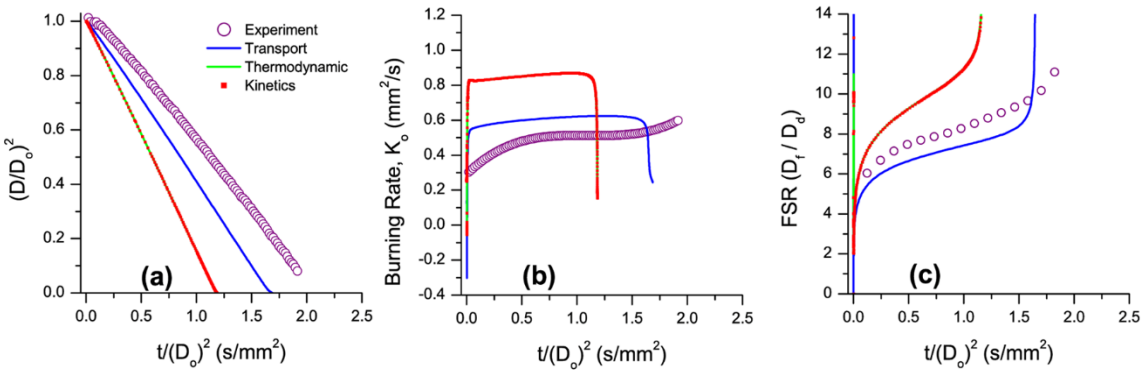

Figure 5.10 Effects of isomer-specific transport parameters, thermodynamic property formulations and elementary kinetic reactions exchange for Sarathy et al. kinetic model [34] for tert-butanol droplet combustion (D_o = 0.52 mm). (a) droplet regression, (b) burning rate, and (c) flame stand-off ratio. Blue lines: isomer specific species transport data exchanged with Merchant et al. [37] (MIT) model. Green lines: isomer specific species thermodynamic data exchanged with MIT model. Red square (small) symbol: isomer specific elementary reactions exchanged with MIT model.

5.4.7 SOOTING PROPENSITY ANALYSIS OF SEC- AND ISO-BUTANOL

Finally, the experimental flame imaging, as illustrated in Figure 5.1, provides a vital lead in investigating the sooting tendency of butanol isomer droplets at atmospheric pressure. It is evident that with the exception of n-butanol flame, iso-, sec- and tert-

butanol flame exhibited visibly prominent yellow luminosity between the outer flame boundary (pale bluish) and the inner droplet surface. The luminosity for tert-butanol monotonically vanishes as the droplet regresses, whereas it continues to be observed for sec- and iso-butanol until the droplet reaches its flame-out phase. Interestingly, even though the yellow flame is a classical 'observatory' marker for soot, no subsequent soot shell (and/or soot fragment) was experimentally ever noticed which indirectly suggests that the mechanism leading to soot oxidation is also competitive to soot production. This speculation is further explored by invoking spatial-temporal analysis of key soot precursors like acetylene (C_2H_2) and ethylene (C_2H_4). The analysis is limited to sec- and iso-butanol for the simulations involving MIT model only. As the current droplet modeling platform model does not include a comprehensive soot modeling module, the forth-coming discourse should be parsed carefully as a 'qualitative' analysis to comprehend the gross features as observed in the experiments.

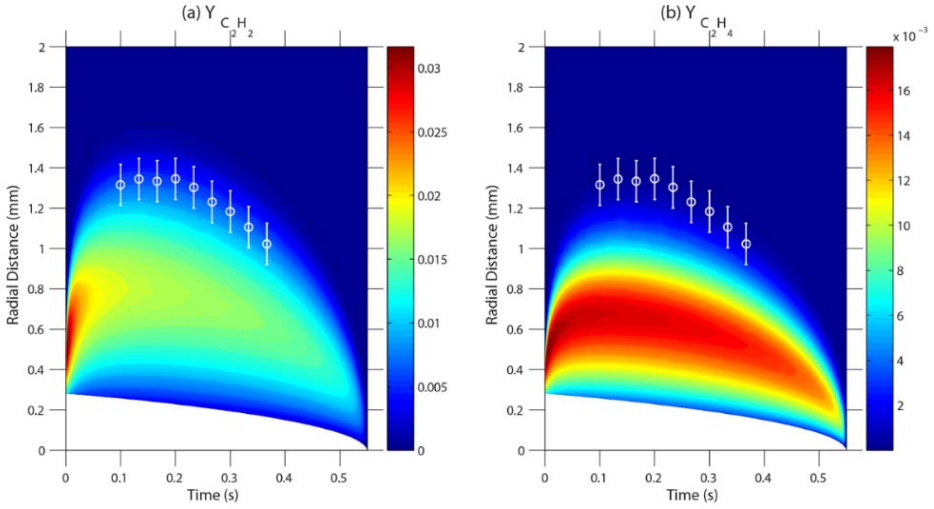

Figure 5.11 Predicted spatiotemporal evolution of mass fraction for selective species of sec-butanol droplet combustion deploying Merchant et al. kinetic model [37]. (a) Acetylene, C_2H_2 (b) Ethylene, C_2H_4. Symbol: experimentally measured flame radii (with time) and associated uncertainties. Initial droplet diameter is 0.53 mm. Atmospheric condition for simulation: P = 1 atm, T = 298 K.

The mass fraction of soot precursors, i.e. Y_{C2H2} and Y_{C2H4}, are plotted in space-time coordinates for sec- and iso-butanol in Figure 5.11 and Figure 5.12 respectively. Experimental evolution of the outer flame edge radii (with time) along with associated experimental uncertainties is collocated in the figures for visual reference of the flame position. Similar to the experimental observation for the 'yellow luminosity', computational predictions of mass fractions for C_2H_2 and C_2H_4 (for both the butanol isomers) also evolved within the experimentally measured outer flame radius. Moreover, the mass fraction concentration peaks in between the droplet surface and the outer flame region. And subsequently, both Y_{C2H2} and Y_{C2H4} reduce to zero near the experimentally measured flame location which qualitatively manifests the hypothesis of soot oxidation within the physical flame boundary. This observation indirectly ratifies the robustness of the MIT model, even though no soot modeling was directly coupled with the existing computational modeling.

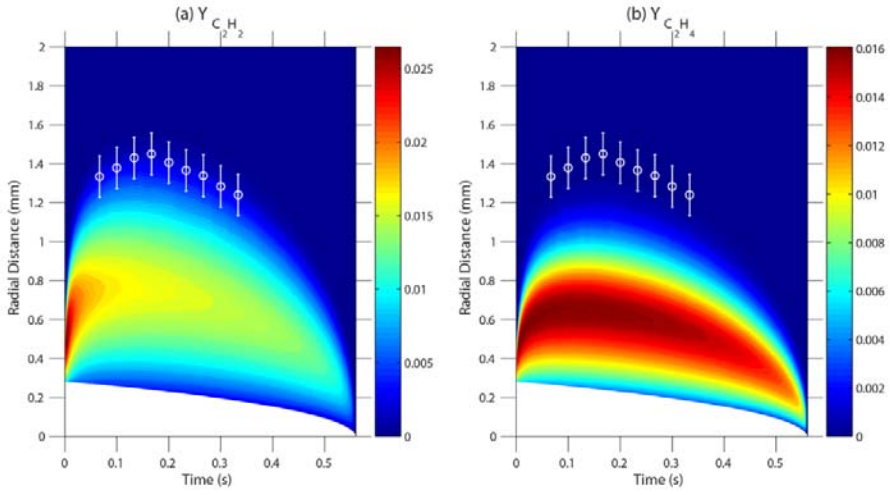

Figure 5.12 Predicted spatiotemporal evolution of mass fraction for selective species of iso-butanol droplet combustion deploying Merchant et al. kinetic model [37]. (a) Acetylene, C_2H_2 (b) Ethylene, C_2H_4. Symbol: experimentally measured flame radii (with time) and associated uncertainties. Initial droplet diameter is 0.55 mm. Atmospheric condition for simulation: P = 1 atm, T = 298 K.

5.5 CONCLUDING REMARKS

Experimental results of droplet burning under reduced gravity (O~10^{-4} g) show that D^2 histories of n-, iso-, and sec- butanol are almost identical while tert-butanol has noticeably lower burning rates. FSR results suggest that n-butanol has the smallest FSR with the other three butanol isomers having FSRs close to each other.

Numerical simulation using detailed combustion chemistries reported by LLNL and MIT. The LLNL model does a good job predicting the D^2 and FSR of n -butanol, but it overshoots the burning rates and FSRs of the other three isomers. The MIT model best predicts the evolution of droplet diameter for iso-butanol and provides acceptable predictions for the other isomers. The predictions for tert-butanol from either LLNL or MIT model are not as aligned with the data as for the other isomers which suggest room for improvement in the future.

Finally, the influence of chemical kinetics, thermodynamic and transport properties of Sarathy et al model (LLNL) for droplet combustion is individually analyzed. The rigorous computational analysis highlights that the difference in transport property coefficients of isomer specific species for LLNL model is responsible for the deviations observed for droplet combustion experiments. A reexamination of updated transport parameters for the LLNL model is thus suggested.

5.6 REFERENCES

[1] National Research Council, Transforming Combustion Research through Cyberinfrastructure, The National Academies Press, Washington, DC, 2011.

[2] P.S. Nigam, A. Singh, Production of liquid biofuels from renewable resources, Progress in Energy and Combustion Science, 37 (2011) 52-68.

[3] H.A. Skinner, A. Snelson, The heats of combustion of the four isomeric butyl alcohols, Transactions of the Faraday Society, 56 (1960) 1776-1783.

[4] B.E. Poling, J.M. Prausnitz, J.P. O'Connell, The Properties of Gases and Liquids, McGraw-Hill Education, USA, 2000.

[5] C. Jin, M. Yao, H. Liu, C.-f.F. Lee, J. Ji, Progress in the production and application of n-butanol as a biofuel, Renewable and Sustainable Energy Reviews, 15 (2011) 4080-4106.

[6] T. Wallner, R. Frazee, Study of Regulated and Non-Regulated Emissions from Combustion of Gasoline, Alcohol Fuels and their Blends in a DI-SI Engine, in, SAE International, 2010.

[7] B.G. Harvey, H.A. Meylemans, The role of butanol in the development of sustainable fuel technologies, Journal of Chemical Technology & Biotechnology, 86 (2011) 2-9.

[8] T. Wallner, S.A. Miers, S. McConnell, A Comparison of Ethanol and Butanol as Oxygenates Using a Direct-Injection, Spark-Ignition Engine, Journal of Engineering for Gas Turbines and Power, 131 (2009) 032802-032802-032809.

[9] D.C. Rakopoulos, C.D. Rakopoulos, E.G. Giakoumis, A.M. Dimaratos, D.C. Kyritsis, Effects of butanol–diesel fuel blends on the performance and emissions of a high-speed DI diesel engine, Energy Conversion and Management, 51 (2010) 1989-1997.

[10] O. Doğan, The influence of n-butanol/diesel fuel blends utilization on a small diesel engine performance and emissions, Fuel, 90 (2011) 2467-2472.

[11] X. Gu, Z. Huang, J. Cai, J. Gong, X. Wu, C.-f. Lee, Emission characteristics of a spark-ignition engine fuelled with gasoline-n-butanol blends in combination with EGR, Fuel, 93 (2012) 611-617.

[12] C. Regalbuto, M. Pennisi, B. Wigg, D. Kyritsis, Experimental Investigation of Butanol Isomer Combustion in Spark Ignition Engines, in, SAE International, 2012.

[13] L. Siwale, L. Kristóf, T. Adam, A. Bereczky, M. Mbarawa, A. Penninger, A. Kolesnikov, Combustion and emission characteristics of n-butanol/diesel fuel blend in a turbo-charged compression ignition engine, Fuel, 107 (2013) 409-418.

[14] Z. Chen, Z. Wu, J. Liu, C. Lee, Combustion and emissions characteristics of high n-butanol/diesel ratio blend in a heavy-duty diesel engine and EGR impact, Energy Conversion and Management, 78 (2014) 787-795.

[15] M. Zheng, X. Han, U. Asad, J. Wang, Investigation of butanol-fuelled HCCI combustion on a high efficiency diesel engine, Energy Conversion and Management, 98 (2015) 215-224.

[16] C.S. McEnally, L.D. Pfefferle, Fuel decomposition and hydrocarbon growth processes for oxygenated hydrocarbons: butyl alcohols, Proceedings of the Combustion Institute, 30 (2005) 1363-1370.

[17] B. Yang, P. Oßwald, Y. Li, J. Wang, L. Wei, Z. Tian, F. Qi, K. Kohse-Höinghaus, Identification of combustion intermediates in isomeric fuel-rich premixed butanol–oxygen flames at low pressure, Combustion and Flame, 148 (2007) 198-209.

[18] P. Dagaut, C. Togbé, Experimental and Modeling Study of the Kinetics of Oxidation of Butanol−n-Heptane Mixtures in a Jet-stirred Reactor, Energy & Fuels, 23 (2009) 3527-3535.

[19] S.M. Sarathy, M.J. Thomson, C. Togbé, P. Dagaut, F. Halter, C. Mounaim-Rousselle, An experimental and kinetic modeling study of n-butanol combustion, Combustion and Flame, 156 (2009) 852-864.

[20] A. Frassoldati, R. Grana, T. Faravelli, E. Ranzi, P. Oßwald, K. Kohse-Höinghaus, Detailed kinetic modeling of the combustion of the four butanol isomers in premixed low-pressure flames, Combustion and Flame, 159 (2012) 2295-2311.

[21] J.T. Moss, A.M. Berkowitz, M.A. Oehlschlaeger, J. Biet, V. Warth, P.-A. Glaude, F. Battin-Leclerc, An Experimental and Kinetic Modeling Study of the Oxidation of the Four Isomers of Butanol, The Journal of Physical Chemistry A, 112 (2008) 10843-10855.

[22] G. Black, H.J. Curran, S. Pichon, J.M. Simmie, V. Zhukov, Bio-butanol: Combustion properties and detailed chemical kinetic model, Combustion and Flame, 157 (2010) 363-373.

[23] I. Stranic, D.P. Chase, J.T. Harmon, S. Yang, D.F. Davidson, R.K. Hanson, Shock tube measurements of ignition delay times for the butanol isomers, Combustion and Flame, 159 (2012) 516-527.

[24] I. Stranic, S.H. Pyun, D.F. Davidson, R.K. Hanson, Multi-species measurements in 2-butanol and i-butanol pyrolysis behind reflected shock waves, Combustion and Flame, 160 (2013) 1012-1019.

[25] D.M.A. Karwat, S.W. Wagnon, P.D. Teini, M.S. Wooldridge, On the Chemical Kinetics of n-Butanol: Ignition and Speciation Studies, The Journal of Physical Chemistry A, 115 (2011) 4909-4921.

[26] B.W. Weber, K. Kumar, Y. Zhang, C.-J. Sung, Autoignition of n-butanol at elevated pressure and low-to-intermediate temperature, Combustion and Flame, 158 (2011) 809-819.

[27] R. Grana, A. Frassoldati, T. Faravelli, U. Niemann, E. Ranzi, R. Seiser, R. Cattolica, K. Seshadri, An experimental and kinetic modeling study of combustion of isomers of butanol, Combustion and Flame, 157 (2010) 2137-2154.

[28] P.S. Veloo, F.N. Egolfopoulos, Flame propagation of butanol isomers/air mixtures, Proceedings of the Combustion Institute, 33 (2011) 987-993.

[29] J.K. Lefkowitz, J.S. Heyne, S.H. Won, S. Dooley, H.H. Kim, F.M. Haas, S. Jahangirian, F.L. Dryer, Y. Ju, A chemical kinetic study of tertiary-butanol in a flow reactor and a counterflow diffusion flame, Combustion and Flame, 159 (2012) 968-978.

[30] T.S. Norton, F.L. Dryer, The flow reactor oxidation of C1−C4 alcohols and MTBE, Symposium (International) on Combustion, 23 (1991) 179-185.

[31] P. Oßwald, H. Güldenberg, K. Kohse-Höinghaus, B. Yang, T. Yuan, F. Qi, Combustion of butanol isomers – A detailed molecular beam mass spectrometry investigation of their flame chemistry, Combustion and Flame, 158 (2011) 2-15.

[32] J. Cai, L. Zhang, F. Zhang, Z. Wang, Z. Cheng, W. Yuan, F. Qi, Experimental and Kinetic Modeling Study of n-Butanol Pyrolysis and Combustion, Energy & Fuels, 26 (2012) 5550-5568.

[33] O. Welz, J.D. Savee, A.J. Eskola, L. Sheps, D.L. Osborn, C.A. Taatjes, Low-temperature combustion chemistry of biofuels: Pathways in the low-temperature (550–700K) oxidation chemistry of isobutanol and tert-butanol, Proceedings of the Combustion Institute, 34 (2013) 493-500.

[34] S.M. Sarathy, S. Vranckx, K. Yasunaga, M. Mehl, P. Oßwald, W.K. Metcalfe, C.K. Westbrook, W.J. Pitz, K. Kohse-Höinghaus, R.X. Fernandes, H.J. Curran, A comprehensive chemical kinetic combustion model for the four butanol isomers, Combustion and Flame, 159 (2012) 2028-2055.

[35] K.M. Van Geem, S.P. Pyl, G.B. Marin, M.R. Harper, W.H. Green, Accurate High-Temperature Reaction Networks for Alternative Fuels: Butanol Isomers, Industrial & Engineering Chemistry Research, 49 (2010) 10399-10420.

[36] M.R. Harper, K.M. Van Geem, S.P. Pyl, G.B. Marin, W.H. Green, Comprehensive reaction mechanism for n-butanol pyrolysis and combustion, Combustion and Flame, 158 (2011) 16-41.

[37] S.S. Merchant, E.F. Zanoelo, R.L. Speth, M.R. Harper, K.M. Van Geem, W.H. Green, Combustion and pyrolysis of iso-butanol: Experimental and chemical kinetic modeling study, Combustion and Flame, 160 (2013) 1907-1929.

[38] M.E. Baumgardner, S.M. Sarathy, A.J. Marchese, Autoignition Characterization of Primary Reference Fuels and n-Heptane/n-Butanol Mixtures in a Constant Volume Combustion Device and Homogeneous Charge Compression Ignition Engine, Energy & Fuels, 27 (2013) 7778-7789.

[39] W. Liu, A.P. Kelley, C.K. Law, Non-premixed ignition, laminar flame propagation, and mechanism reduction of n-butanol, iso-butanol, and methyl butanoate, Proceedings of the Combustion Institute, 33 (2011) 995-1002.

[40] T. Lu, C.K. Law, Toward accommodating realistic fuel chemistry in large-scale computations, Progress in Energy and Combustion Science, 35 (2009) 192-215.

[41] H. Wang, R. Deneys Reitz, M. Yao, B. Yang, Q. Jiao, L. Qiu, Development of an n-heptane-n-butanol-PAH mechanism and its application for combustion and soot prediction, Combustion and Flame, 160 (2013) 504-519.

[42] G.A. Agoston, Influence of Pressure on the Combustion of Liquid Spheres, Journal of Jet Propulsion, 28 (1958) 181-188.

[43] T.I. Farouk, Y.C. Liu, A.J. Savas, C.T. Avedisian, F.L. Dryer, Sub-millimeter sized methyl butanoate droplet combustion: Microgravity experiments and detailed numerical modeling, Proceedings of the Combustion Institute, 34 (2013) 1609-1616.

[44] Y.C. Liu, T. Farouk, A.J. Savas, F.L. Dryer, C. Thomas Avedisian, On the spherically symmetrical combustion of methyl decanoate droplets and comparisons with detailed numerical modeling, Combustion and Flame, 160 (2013) 641-655.

[45] Y.C. Liu, A.J. Savas, C.T. Avedisian, The spherically symmetric droplet burning characteristics of Jet-A and biofuels derived from camelina and tallow, Fuel, 108 (2013) 824-832.

[46] K.-L. Pan, M.-C. Chiu, Droplet combustion of blended fuels with alcohol and biodiesel/diesel in microgravity condition, Fuel, 113 (2013) 757-765.

[47] F.E. Alam, Y.C. Liu, C.T. Avedisian, F.L. Dryer, T.I. Farouk, n-Butanol droplet combustion: Numerical modeling and reduced gravity experiments, Proceedings of the Combustion Institute, 35 (2015) 1693-1700.

[48] Y. Xu, C.T. Avedisian, Combustion of n-Butanol, Gasoline, and n-Butanol/Gasoline Mixture Droplets, Energy & Fuels, 29 (2015) 3467-3475.

[49] C.H. Wang, C.K. Law, Microexplosion of fuel droplets under high pressure, Combustion and Flame, 59 (1985) 53-62.

[50] Y. Ogami, S. Sakurai, S. Hasegawa, M. Jangi, H. Nakamura, K. Yoshinaga, H. Kobayashi, Microgravity experiments of single droplet combustion in oscillatory flow at elevated pressure, Proceedings of the Combustion Institute, 32 (2009) 2171-2178.

[51] S. Nakaya, K. Fujishima, M. Tsue, M. Kono, D. Segawa, Effects of droplet diameter on instantaneous burning rate of isolated fuel droplets in argon-rich or carbon dioxide-rich ambiences under microgravity, Proceedings of the Combustion Institute, 34 (2013) 1601-1608.

[52] C.K. Law, T.Y. Xiong, C. Wang, Alcohol droplet vaporization in humid air, International Journal of Heat and Mass Transfer, 30 (1987) 1435-1443.

[53] Y.C. Liu, C.T. Avedisian, A comparison of the spherical flame characteristics of sub-millimeter droplets of binary mixtures of n-heptane/iso-octane and n-heptane/toluene with a commercial unleaded gasoline, Combustion and Flame, 159 (2012) 770-783.

[54] T. Farouk, F.L. Dryer, Microgravity droplet combustion: effect of tethering fiber on burning rate and flame structure, Combustion Theory and Modelling, 15 (2011) 487-515.

[55] T.I. Farouk, F.L. Dryer, On the extinction characteristics of alcohol droplet combustion under microgravity conditions – A numerical study, Combustion and Flame, 159 (2012) 3208-3223.

CHAPTER 6

OZONE ASSISTED COOL FLAME COMBUSTION OF SUB-MILLIMETER SIZED N-ALKANE DROPLETS

6.1 ABSTRACT

Cool flame combustion of individual and isolated sub-millimeter sized *n*-heptane (*n*-C_7H_{16}) and *n*-decane (*n*-$C_{10}H_{22}$) droplets are computationally investigated for atmospheric and higher operating pressure (25 atm) conditions with varying levels of ozone (O_3) mole fractions in the surroundings. A sphero-symmetric, one-dimensional, transient, droplet combustion model is utilized, employing reduced versions of detailed chemical kinetic models for the fuel species and an appended ozone reaction subset. Comprehensive parametric computations show that the regime of the cool flame burning mode and the transition from cool to hot flames are sensitive to the changes of O_3 loading, pressure, diluent variation, the strength of initiation source, and the influence of fuel vapor pressure at the ambient condition. For both fuels and over a range of O_3 concentrations in the ambient, sustained cool flame burning can be directly produced, even for sub-millimeter sized droplets. Over some range of O_3 concentrations, operating pressure, and drop diameter, a self-sustaining, continuous cool flame burn can be produced without incurring a hot flame transition. For sufficiently high O_3 concentrations, combustion initiation is always followed by a hot flame transition. Fuel volatility is also shown to be important for initiation and transition to cool flame and hot flame initiation. For fuels having a flash point lower than the ambient temperature (e.g. *n*-heptane), atomic O radicals formed by O_3 decomposition react with the partially premixed, flammable gas phase near the droplet surface, leading to OH radicals, water production, and heat that auto-thermally accelerates

the combustion initiation process. For fuels with flashpoints higher than the ambient temperature (e.g. *n*-decane), the reaction progress is limited by the local fuel vapor concentration and the necessity to heat the droplet surface to sufficiently high temperatures to produce locally flammable conditions. As a result, the initial transient for establishing either cool flame or hot flame transition is significantly longer for high flash point fuels. The transition of locally partially premixed reaction to diffusive burning conditions is more evident for high flash point conditions.

6.2 INTRODUCTION

Observations of long-duration cool flame burning of isolated *n*-alkane droplets with a large initial diameter (D_o) under microgravity conditions [1-5] demonstrate an interesting venue for the study of diffusive cool flame burning. The term, "cool flame" has been historically associated with observations involving homogenously premixed conditions [6, 7]. The cool flame diffusive burning mode of an isolated droplet is governed by a strong coupling between the low-temperature chemistry and diffusive transport that is significantly different than for premixed cool flame, static reactor or flow reactor conditions.

For hot flame isolated droplet combustion, three types of classical hot flame phenomena are observed; 1) radiative extinction; 2) diffusive extinction, or 3) complete consumption of the liquid droplet. The extinction phenomena occur at some finite liquid droplet size as the rate of heat loss to the surroundings exceeding the reaction zone heat generation. Radiative extinction occurs at larger droplet sizes as the flame radius expands upon initiation towards what would be its hypothetical stoichiometric location, to undergo

extinction as the ratio of radiative heat loss to heat generation exceeds unity. For fuels that have sufficiently active low and intermediate temperature kinetic activity, the radiative extinction behavior can transition to cool flame diffusive burning. For example, in experiments aboard the International Space Station (ISS), large *n*-heptane (*n*-C_7H_{16}) droplets (D_o > ~ 4 mm) ignited in the air at atmospheric pressure the hot flame phenomena occurring initially radiatively transitions to a cool flame diffusive burning mode [2]. For smaller *n*-heptane droplets that do not have an overwhelming radiative loss from the flame, only hot flame burning is observed, leading to diffusive extinction or complete liquid phase consumption. Hence, cool flame diffusive burning appeared to a phenomenon that could only be studied through first invoking significant radiative losses.

However, in more recent ISS experiments using *n*-decane (*n*-$C_{10}H_{22}$) droplets (D_o ~ 4 mm) [5], cool flame behavior was able to be achieved directly by controlling the hot wire initiation energy– current amplitude and duration. Numerical analyses reveal that as a result of the high flashpoint of *n*-decane (319.3 K [8]), modulation of the initiation energy can be utilized to control the formation rate of partially premixed flammable fuel/air mixtures near the drop surface, and hence, control the heat release associated with vapor phase reaction. By controlling the initiation energy deposition, both direct cool flame and hot flame burning modes are achievable. The flashpoint of *n*-C_7H_{16} (269.3 K [9]) is lower than the ambient air temperature in ISS experiments (298 K), and significant volumes of flammable fuel/air vapor mixture are readily formed during the droplet growth and deployment phase prior to application of hot wire initiation energy. The total ignition energy available is strongly influenced by the available partially premixed flammable mixture near the drop surface, and thus controlling hot wire initiation energy is ineffective

in controlling the applied ignition energy. The overall ignition energy dependence on fuel flash point relative to ambient temperature is also influenced by the initial droplet size, but cool flame droplet burning continues to be much more easily observed under ISS conditions and droplet sizes that result in the radiative extinction of large droplets.

The question remains as to whether other means might exist to control initiation energy deposition rate parameters so as to establish cool flame burning directly for small initial droplet sizes. Should this be achievable, cool flame droplet burning phenomena might not only be observed on ISS over a larger range of initial droplet sizes but perhaps even in ground-based facilities such as drop towers [10] or isolated, freely falling droplet experiments [11]. In fact, ground-based experiments might enable the use of multiple diagnostic and chemical analytical methods not possible to be implemented on ISS.

In counterflow, pre-vaporized, laminar diffusion flame configurations, the addition of ozone to the oxidizer flow stream has been demonstrated as a mean of achieving stabilized cool flame burning conditions [12-14]. The rapid decomposition of O_3 produces active atomic oxygen (O), that substantially reduces the induction timescale for initiating low temperature, exothermic fuel oxidation chemistry, leading to flame initiation and quasi-stable cool flame diffusive burning at intermediate reaction temperatures characteristic of the negative temperature kinetic regime. Adoption of a similar O_3 addition approach to isolated droplet combustion configurations might achieve the goal of observing the cool flame droplet burning mode with smaller droplet size.

The primary objective of this study is to computationally evaluate the potential of O_3 addition to directly induce cool flame burning for sub-millimeter sized low and high flash point fuels, i.e. for *n*-C_7H_{16} and *n*-$C_{10}H_{22}$ droplets, respectively. Below, we investigate

two initial droplet diameters (D_o = 0.1 and 0.5 mm) and two ambient air pressures (1 and 30 atm) seeded with different levels of O_3. The role of fuel flash point, vapor pressure, and liquid phase thermodynamic and transport properties on cool flame initiation and burning characteristics are elucidated, including the time-dependent evolutions of the surrounding gas temperature and intermediate/product species fields. For such small droplets, over the entire combustion event leading to self-sustaining hot flame or cool flame burning, radiative heat loss transfer effects are negligible.

6.3. NUMERICAL MODELING

This computational study is performed using a sphero-symmetric multi-component droplet combustion model developed previously, the details of which can be found elsewhere [10, 15-18]. Important attributes of the model lie in its capability of incorporating detailed gas phase kinetics, multi-component transport formulation, spectrally resolved radiative heat transfer and heat transfer perturbation effect from the presence of tethering fibers.

The simulations are performed using numerically-reduced kinetic models for *n*-C_7H_{16} [19] and *n*-$C_{10}H_{22}$ [20] combustion developed previously. The *n*-C_7H_{16} and *n*-$C_{10}H_{22}$ models consist of 128 species undergoing 565 elementary reactions and 233 species undergoing 1266 elementary reactions respectively. Both models were obtained from a detailed kinetic construct for straight chain *n*-alkane combustion kinetics for carbon numbers from 7 to 16 [21, 22]. The data correlations reported in Daubert and Danner [23] are used in evaluating liquid phase properties.

The coupled set of partial differential and algebraic equations are discretized in two steps- first in space and then integrated temporally as a set of coupled ordinary differential-algebraic equations. A node-centered finite volume approach with 2nd order accuracy is employed for spatial discretization. The interface between the gas and liquid phases outlines the volume boundaries. The inner zone corresponds to the liquid phase fuel while the outer zone represents the gas phase ambient including the far-field which is defined as two hundred times the initial droplet diameter. Prescribed fixed ambient composition and temperature are constrained in the far-field as typical Dirichlet boundary conditions. The innermost liquid node serves as the center of origin imposing the no-flux condition. In order to avoid oscillatory solutions, the discretized mass flux is calculated on the cell faces instead of cell centers. The final set of discretized equations are then numerically integrated using a variable higher order backward differencing scheme (up to 5th order) with adaptive time step utilizing implicit multipoint interpolation. All the reported simulation results are obtained using 50 (liquid) x 150 (gas) nodes. Test results that confirm grid-independency of the solution are separately annexed in the supplementary material as Supplementary Figure 6.12.

To investigate the sensitivity of predictions to the chosen ozone kinetics, two different kinetic model sources [24] and [25] were separately appended to the hydrocarbon reduced models. The kinetics appearing in reference [25] are based upon the rate parameters proposed in reference [26]. The predicted behaviors were found to be only weakly dependent on the chosen source of O_3 chemistry. An exemplary illustration of peak gas temperature for a 0.5 mm initial diameter *n*-C_7H_{16} droplet comparing predictions using these two different ozone model sources at two different O_3 seeding conditions is presented

in Supplementary Figure 6.13. The kinetic model based on the work of Ombrello et al. [25] was used in all of the work subsequently reported here.

6.4 RESULTS AND DISCUSSION

6.4.1 COOL FLAME COMBUSTION CHARACTERISTICS OF A LOW FLASH POINT TEMPERATURE FUEL – N-HEPTANE

Initiation dynamics and stabilization of cool flame of an n-heptane droplet at 298 K

The potential for direct initiation of cool flame burning for a sub-millimeter size *n*-C_7H_{16} droplet with O_3 addition is first explored conceptually by employing two different initiation energy deposition approaches. In the first, the entire ambient temperature field is raised at time zero-from 298 K to 425 K (hot ambient approach). The second approach imposes a predefined trapezoidal shaped high-temperature ambient profile (prescribed thermal ignition energy source approach) surrounding the droplet at time zero.

The first approach conceptually addresses the immersion of a room temperature droplet into a high-temperature ambient environment created by a movable "furnace" to surround the droplet, as has been applied in experimental studies previously [27, 28]. The second approach is identical to that used in our prior papers for simulating hot wire and spark discharge initiation energy application to isolated droplets in drop towers and space experiments [1, 2, 29]. It has been shown earlier [29] that by controlling the ignition energy deposition, initial transients in the burning behavior are better resolved numerically, an important aspect for considering fuels of disparate flash points relative to ambient temperature.

In each approach, the initial droplet is assumed to have been previously deployed at 298 K, and a fuel vapor phase/ambient air layer is numerically computed (without chemical reaction terms) to develop through vaporization. The spherical divergence of this computation results in a partially premixed vapor/air layer for which far-field conditions are reached within a few diameters of the droplet for the fuels studied here. This procedure is an ideal approximation of the droplet growth and deployment into the surrounding ambiance at the same far-field temperature prior to initiating experimental combustion protocols by application of the initiation energy approaches. This approximation is more realistic for the modeling of high flash point fuels than modeling of the ensuing behaviors of low flash point fuels.

Figure 6.1 illustrates the peak gas phase temperature profiles predicted for *n*-C_7H_{16} droplet D_o = 0.5 mm at 1 atm pressure for the two different ignition approaches. A wide range of O_3 seeding levels was parametrically investigated and only two sets of results pertaining to 3% and 7% O_3 loading (by mole fraction) are shown here for simplicity. Regardless of the ignition approaches, the hot flame burning mode is established with 7% O_3, whereas direct formation of the cool flame burning mode is observed for 3% O_3 loading. Although there are considerable differences in time delays to form a sustained cool flame burning between the two ignition approaches, it is evident that the O_3 loading determines the overall flame configuration between cool and hot flames, consistent with the previous results from counterflow burner experiments [12-14]. Regardless of ignition approaches, O_3 loading can initiate cool flame droplet combustion, however, the prescribed ignition energy approach (Figure 6.1) reveals faster initiation and stabilization of the cool

flame. Therefore, for the remainder of this article, all results and discussions are based on the prescribed thermal ignition source.

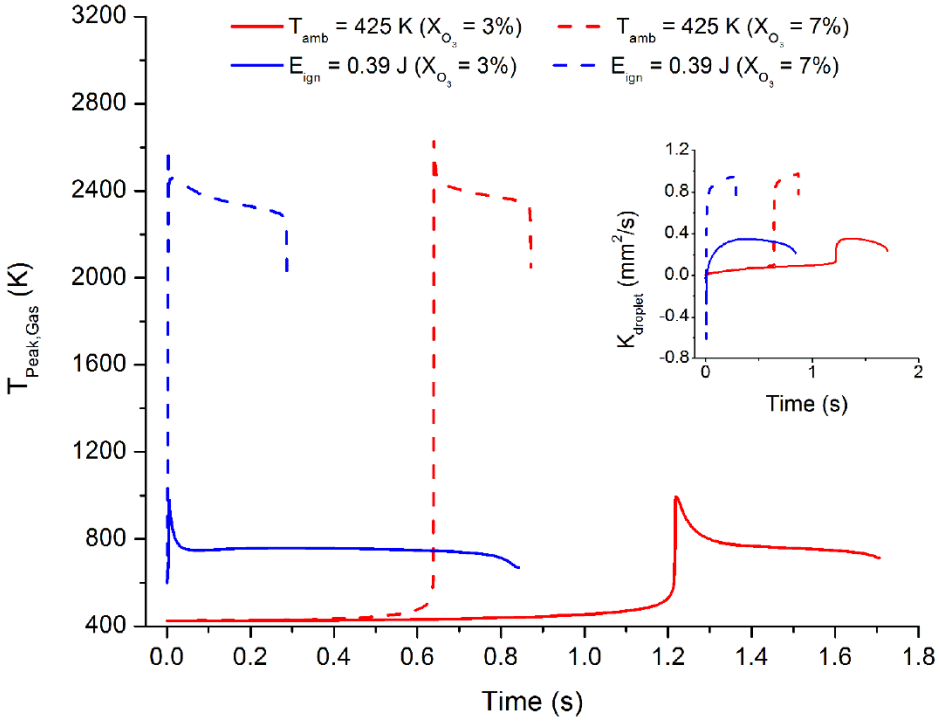

Figure 6.1 Temporal evolution of peak gas temperature and droplet burning rate (inset figure) for two different ignition approaches. Simulated case: *n*- C_7H_{16} droplet, D_o = 0.5 mm, X_{O2} = 21%, X_{O3} = 3% (solid lines) or X_{O3} = 7% (dashed lines) with balance N_2. Ambient condition: P = 1 atm, T = 298 K (prescribed thermal ignition energy source, blue lines) and T = 425 K (immersion of droplet into a high-temperature ambient, red line). Ignition energy of 0.39 J is the minimal energy requirement for the successful initiation of cool flame burning mode under the investigated conditions.

Figure 6.2 highlights the initial transient reaction dynamics predicted for a 0.5 mm *n*-C_7H_{16} droplet by applying a thermal ignition source at an ozone seeding level of X_{O3} = 3% (by mole) in ambient air at atmospheric pressure. The predicted heat transfer through gas phase conduction, diffusion velocity, and radiation, as well as fuel mole fraction spatial-temporal variations, are shown in Supplementary Figure 6.14. Since the fuel flash point of *n*- C_7H_{16} (269.3 K) is significantly lower than the ambient temperature, the

deposited initiation energy interacts with the initial stratified layer of fuel vapor and ambient gases surrounding the droplet, which upon chemical reaction, significantly contributes to the auto-thermal acceleration of the oxidation rates near the drop surface. The predicted spatial-temporal evolutions of mole fraction for select gas phase species (ozone (O_3), atomic oxygen (O) and ketohydroperoxides ($C_7H_{14}O_3$)) and gas phase temperature are illustrated in Figure 6.2. The black dashed line in Figure 6.2 (b) indicates the location of peak gas temperature (defined here as the "flame stand-off" ratio, FSR). The observed dynamics are discussed in terms of four sequential time frames from the onset of initiation energy deposition to the establishment of quasi-steady, cool flame droplet burning; **Period I**: initiation energy dissipation ($0 < t < \sim 5$ ms), **Period II**: initiation and auto-thermally accelerating chemical reaction of the partially premixed gas phase region surrounding the droplet ($\sim 5 < t < \sim 17$ ms), **Period III**: transition of partially premixed to diffusive burning supported by droplet vaporization, ($\sim 17 < t < \sim 30$ ms), and **Period IV**: quasi-steady cool flame droplet burning to extinction or complete fuel consumption ($t > \sim 30$ ms).

In **Period I**, local initiation energy applied as an instantaneous temperature profile distribution near the surface transiently decays, primarily by diffusive heat transfer to the droplet surface and far field (Figure 6.2 (b)). The imposed peak gas temperature decreases during this time. The applied initiation energy distribution stimulates the decomposition of ozone near the drop surface and as behavior transitions to **Period II**, the resulting production of O radicals (cf. subplot a and c), react with fuel vapor producing oxygenated hydrocarbon intermediates, OH radicals, and subsequent production of water. The process yields significant chemical energy release primarily through the production of water from

OH radical reactions with *n*- C_7H_{16} vapor, leading to an auto-thermal acceleration of the local chemical reaction rates. The near-surface gas temperature increases from 300 K to ~ 700 K (subplot b). Auto-thermal acceleration of the local chemical reactions rate continues, and, over a period of ~ 20 ms of transient behavior, the rate of generation and subsequent reactions of ketohydroperoxides ($C_7H_{14}O_3$ occurs (subplot (d)), with local ozone concentrations also being fully consumed (subplot a). The reactions within the partially premixed, stratified reactive layer surrounding the drop lead to localized reaction at temperatures well above that characteristic of oxygen addition/isomerization and subsequent decomposition processes characteristic of low temperature degenerate branching reaction of cool flame droplet burning (note the complete depletion of $C_7H_{14}O_3$ in subplot (d)).

Subsequent evolution to either sustained hot or cool flame droplet burning is dependent upon the reaction initiation energy, and the ozone-seeded stimulation of auto-thermally accelerating the chemical reaction of the initially present and evolving combustion of fuel vapor/air mixture near the drop surface. Both initiation energy and subsequent partially premixed chemical reaction processes contribute to what is generally termed, the applied "ignition energy". In the present case, the initiation source energy is low and the heat release upon reaction initiation is significant and proportional to the volume of partially premixed mixtures surrounding the drop. Clearly, initial droplet temperature, ambient temperature/pressure, and droplet growth/deployment time prior to application of initiation energy all affect the volume of reactive mixture surrounding the droplet and hence the significance of chemical reaction contributions to defining the ignition energy that was applied.

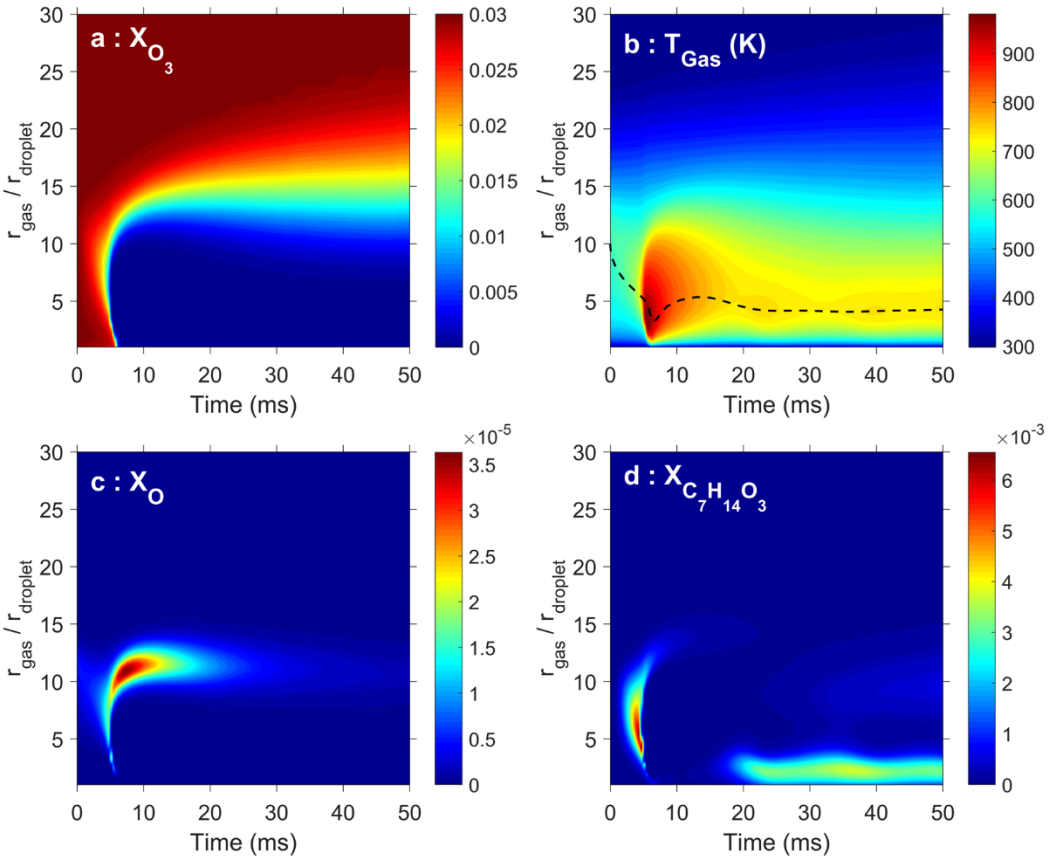

Figure 6.2 Spatiotemporal evolution of gas phase (a) O_3 mole fraction, (b) gas phase temperature, T_{Gas}, (c) atomic 'O' mole fraction and (d) $C_7H_{14}O_3$ mole fraction of *n*-C_7H_{16} droplet combustion. Simulated case: D_o = 0.5 mm, X_{O2} = 21%, / X_{O3} = 3% and balance N_2. Ambient condition: P = 1 atm and T = 298 K. Subplot b: dashed black line denotes peak gas temperature location.

Even as the reactive heat generation rate from the initial partially premixed reacting gases decreases, heat transport to the droplet liquid surface must provide sufficient fuel vapor production to transition to and sustain diffusive droplet burning. Under the present conditions, the predicted transition (**Period III)** leads to evolving local reaction temperatures that are below those that define sufficiently short characteristic decomposition times of hydrogen peroxide that would promote the transition to hot flame ignition [21, 30], characteristic of the negative temperature coefficient (NTC) kinetic behavior. Cool flame droplet burning phenomena are characterized by the balance of heat loss/heat generation in the region surrounding the droplet with maximum rate of reaction

achievable from low temperature oxidation and local temperatures that lie between the NTC degenerate branching (turnover temperature) and the "hot ignition" temperature, characterized by sufficiently rapid peroxide decomposition [3].

Period III (~17 ms < t < ~ 30 ms) can be discerned from the spatial/temporal evolutions of the $C_7H_{14}O_3$ fraction (from initial appearance to depletion) and the fuel vapor mole fraction (Supplementary Figure 6.14). Thermal energy generation, local storage, and far-field loss dynamics associated with regenerating fuel vapor, gas conduction/diffusion and reaction zone structure all relate to the system advancing to quasi-steady (diffusive) cool flame droplet burning after ~ 30 ms in **Period IV**. As time progresses, diffusive heat loss to the far field becomes dominant in the outer radial region, whereas conductive heat transport is significant in both the inner and outer zones demarcated by the location of the highest temperature within the evolving cool flame structure. Subsequently, the evolving balance results in a maximum spatial temperature of ~765 K near the droplet surface (r/r_d ~ 4) and cool flame chemistry is reflected by the reappearance of $C_7H_{14}O_3$ (subplot d). The dashed line in subplot 'b' illustrates the location of peak gas temperature, the numerical definition of the "flame location" for subsequent cool droplet burning (t > ~ 30 ms).

6.4.2 TEMPORAL AND SPATIAL ANALYSIS OF SELECTED SPECIES EVOLUTION OF N-HEPTANE DROPLETS

The dynamics of sustained cool flame droplet combustion are controlled by the *in-situ* balance of heat generation and the continuing heat transport to the far field surrounding the droplet [3]. The heat generation is produced by oxidative kinetics relevant to NTC behavior. The spatial-temporal analyses of species profiles provide insights into those

reactions controlling droplet combustion initiation and quasi-steady state (QSS) burning. The spatial distribution of key species and gas phase temperature for two different reaction times characteristic of ignition and quasi-steady behaviors are presented in Figs. 6.3 and 6.4 respectively. The subplot (a) of each illustrates the radial distributions of *n*-C_7H_{16}, H_2O, O_3 and O_2 mole fractions, whereas subplot (b) highlights the predicted mole fraction distributions of CO, CO_2, CH_2O, C_2H_4, and $C_7H_{14}O_3$. The gas phase temperature predictions for the very early transients (i.e., t ~ 0.005 s) are shown in Figure 6.3 (a), whereas the same parameters are presented in Figure 6.4 (c) for a representative QSS condition (i.e. t ~ 0.274 s).

During the initial transient stage, as initiation energy dissipation evolves, regions where gas temperatures exceed ~ 440 K lead to rapid dissociation of O_3 (solid black line, Figure 6.3(a)). No ozone is observed in regions where gas phase temperature exceeds 960 K. The key role of ozone in accelerating chemical reactions is through production of O atoms by decomposition, followed by H atom abstraction from the fuel, i.e. (*n*-C_7H_{16} + O = *n*-C_7H_{15} + OH and subsequent H atom abstraction by *n*-C_7H_{16} + OH = *n*-C_7H_{15} + H_2O), producing heat and *n*-heptyl radicals. The addition of molecular O_2 to *n*-heptyl radicals, followed by isomerization of the adduct and subsequent oxygen addition reactions leads to degenerate chain branching and the formation of cyclic ethers, ketones, aldehydes, and ketohydroperoxides (cf. solid blue line, Figure 6.3 (b)) [21, 22, 31]. Significant production of C_1-C_5 intermediates (not shown) are also predicted, inclusive of large amounts of C_2H_4 (Figure 6.3 (b)).

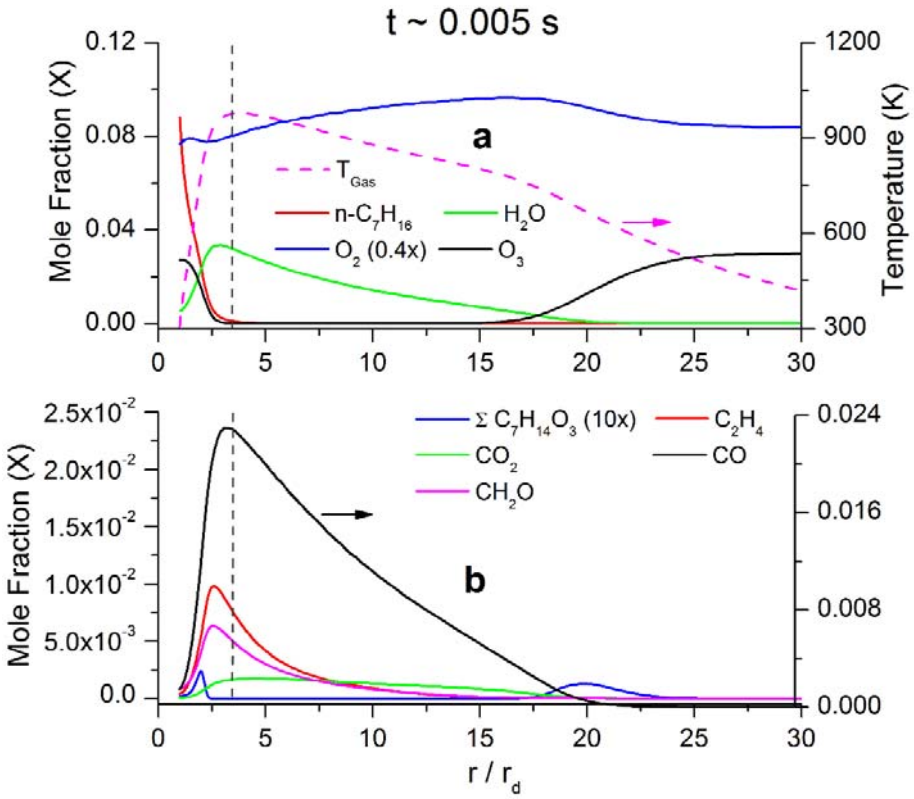

Figure 6.3 Spatial mole fraction distribution of selective key species and gas phase temperature at representative early ignition time, t ~ 0.005 s. Simulated case: D_o = 0.5 mm, X_{O2} = 21%, X_{O3} = 3% and balance N_2, *n*-C_7H_{16} fuel droplet. Ambient condition: P = 1 atm, T = 298 K. Ketohydroperoxide ($C_7H_{14}O_3$) profile (subplot b, 10x magnification) represents the summation of all the isomers. Gray dashed vertical line at r/r_d ~ 3.5 (both subplots) indicates the location of maximum.

Figure 6.4 presents species and temperature distributions at a later combustion time, t ~ 0.274 s. Two distinct spatial $C_7H_{14}O_3$ mole fraction peaks are noted - one in the fuel rich inner zone and the other in the outer oxygen-rich zone appearing near ~ 650 K and ~ 620 K, respectively (Figure 6.4 (b) and (c)). Oxygen addition/isomerization processes are most rapid near these temperatures, and oxygen mole fraction is prevalent throughout the entire reaction zone. Oxygen addition to *n*-heptyl radicals and isomerization is key to the production of ketohydroperoxides through further molecular oxygen addition, and their decomposition is essential to chemical kinetic degenerate chain branching [21, 31]. At higher temperatures, the rate of decomposition of the *n*-heptyl radical- molecular oxygen

adduct exceeds its formation rate (and as a result ketohydroperoxide formation also slows), resulting in the peak in the fuel rich zone. In the outer zone, the depletion of *n*-heptane leads to curtailment of peroxy heptyl radicals even as the lower temperatures emphasize formation or decomposition rates, and hence the lower peak in comparison to that in the fuel rich zone. These kinetic behaviors as a result of the temperature, fuel, and oxygen distribution also result in the radial locations for the maximum rates of increase and decrease of the total peroxy heptyl radical ($\Sigma C_7H_{15}O_2$) mole fraction. Similar non-monotonicity in the ketohydroperoxide profile was observed in our prior work [3] and later by Paczko et al. [32] in analyzing the cool flame behavior of large-sized *n*-heptane droplets. Unlike the large diameter droplets, where the extinction is dictated by the buildup of ketohydroperoxide towards the later stage, these sub-millimeter droplets do not undergo any extinction; rather they burn to completion.

The temporal evolution of peak mole fraction (X) profiles of selected species for the 0.5 mm droplet combustion case seeded with X_{O3} = 3% at atmospheric pressure condition are illustrated in Figure 6.5. Far-field accumulation of carbon monoxide (CO) is observed, a key oxidation characteristic of low and intermediate temperature kinetics and the presence of larger amounts of hydrocarbon intermediate species that compete for any OH radicals that would otherwise react with CO to produce CO_2 [2, 33]. Figure 6.5 (b) summarizes the peak mole fraction profiles for some key intermediates: CH_4, C_2H_2, C_2H_6, and C_2H_4 (inset figure). The predicted profiles are qualitatively similar to those found in earlier work on larger diameter cool flame droplet burning without ozone seeding [3, 4]. Large fractions of these species are observed with little or no acetylene (C_2H_2) formation or the formation of other soot precursor species, as reaction temperatures are so low. The

time-resolved evolution of the most reactive radicals characteristic of high-temperature reactivity (inset figure: H, O, and OH; observed during hot droplet burning) and those found in low-temperature chemistry (HO_2, $C_7H_{15}O_2$, and $C_7H_{14}O$) are presented in Figure 6.5 (c), clearly displaying the premixed/diffusive reaction transition to sustained cool flame droplet burning.

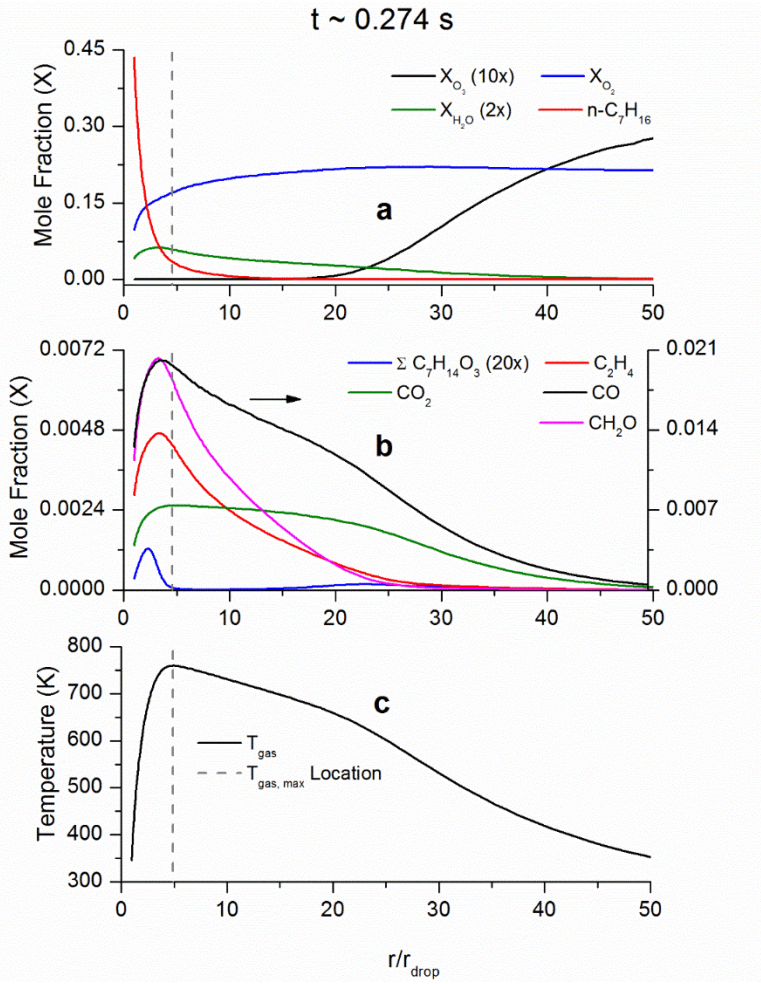

Figure 6.4 Spatial mole fraction distribution of selective key species and gas phase temperature profiles at representative quasi-steady state time, t ~ 0.274 s. Simulated case: D_o = 0.5 mm, X_{O2} = 21%, X_{O3} = 3% and balance N_2, *n*-C_7H_{16} fuel droplet. Ambient condition: P = 1 atm, T = 298 K. Ketohydroperoxide ($C_7H_{14}O_3$) profile (subplot b, 20x magnification) represents the summation of all the isomers. Gray dashed vertical line at r/r_d ~ 5 (all subplots) indicates the location of maximum temperature.

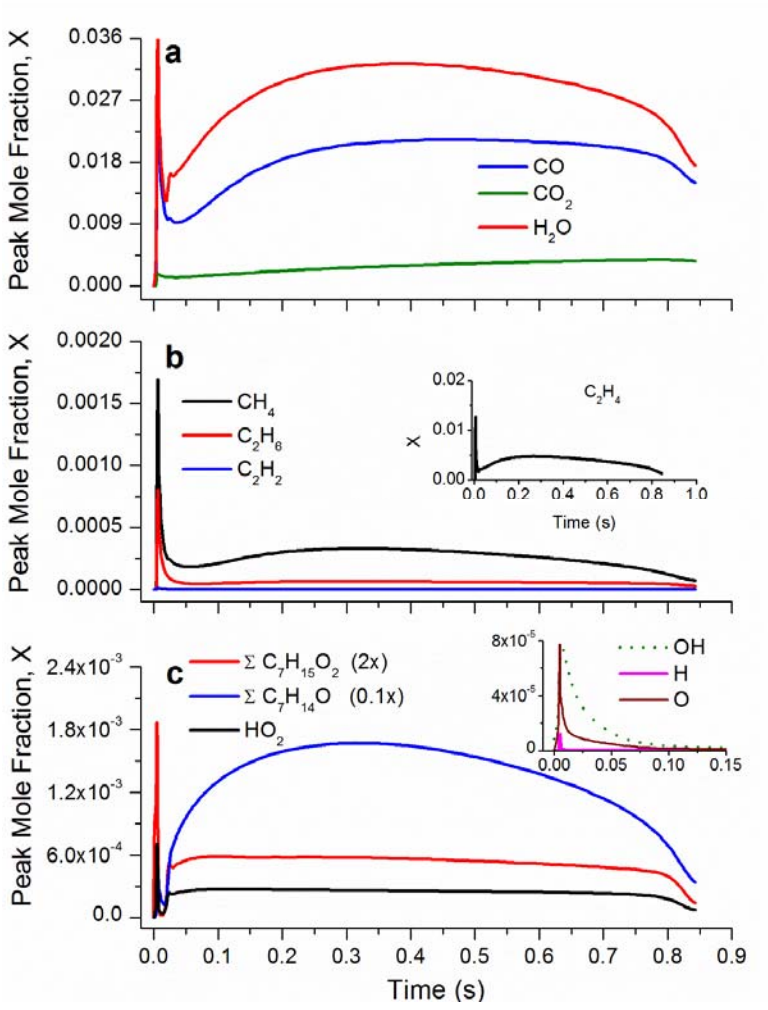

Figure 6.5 Temporal evolution of peak mole fraction profiles of select key species. Simulated case: *n*-C_7H_{16} fuel droplet D_o = 0.5 mm, X_{O2} = 21%, X_{O3} = 3% and balance N_2. Ambient condition: P = 1 atm, T = 298 K.

In summary, the combined effects of initiation energy, and ozone-stimulated chemical heat release from initially present fuel vapor oxidation play key roles in establishing a sustained cool flame droplet burning behaviors for sub-millimeter sized low flash point fuels such as *n*-C_7H_{16}. While hot flame droplet burning can always be established, appropriate seeding levels of ozone and lower initiation energies can result in establishing direct cool flame droplet burning, even for fuels with flash points below droplet and ambient initial temperatures. However, in all cases, heat release from the

stimulated reaction of initially vaporized fuel near the drop surface will limit and may even preclude the ability to establish cool flame burning behavior. The next section compares the establishment of low temperature burning characteristics of fuels that have significantly different thermophysical properties.

6.4.3 COOL FLAME COMBUSTION CHARACTERISTICS OF A HIGH FLASH POINT TEMPERATURE FUEL (N-DECANE)

COMPARISON OF LOW AND HIGH FLASH POINT FUEL AT 1 ATM

Recent experiments with large diameter *n*-decane (*n*-$C_{10}H_{22}$) droplets on board the ISS demonstrated that for fuels and conditions where ambient temperatures are below the flash point, the *overall* ignition characteristics are significantly more dependent on the thermal initiation energy that is applied. For these fuels, the liquid surface temperature must be raised above the flashpoint in order to supply flammable vapor/air mixtures near the drop, and initially, there is very little vapor/air mixtures for reactions to be stimulated by ozone seeding. As a result, the initiation energy deposition characteristics control the initial rate of flammable vapor development surrounding the drop, thus offering control of the ozone seeded chemical heat release properties that can contribute to thermally driving the vapor phase autoignition and transition to vapor phase droplet burning. Varying the rate of initiation energy deposition applied to initially large droplet diameter droplets in atmospheric pressure air at 298K was shown [5] to lead to two different pathways for establishing cool flame droplet burning: (1) classical hot flame radiative extinction followed by prolonged cool flame or (2) direct establishment of a cool flame droplet burning. In contrast to conditions where the flash point of a fuel is well below the ambient

conditions, the flash point of *n*-$C_{10}H_{22}$ (319.3 K [8]) is well above ambient temperature (298K) at one atmosphere pressure. Of course, by varying pressure and oxygen index, the flashpoint of a fuel can be increased or decreased. Sufficient decreases in pressure alone can lead to behaviors for *n*-decane that are similar to those discussed above for *n*-heptane droplets at one atmosphere pressure. Here we investigate the effects of ozone seeding on the ignition/transition behavior of *n*-decane at atmospheric pressure. Simulations results of sub-millimeter sized *n*-$C_{10}H_{22}$ droplets are presented in Figs. 6-8, comparing peak gas temperature, burning rates, flame stand-off ratio, and the spatial-temporal variation of droplet temperature, gas phase temperature, the mole fraction of fuel and select species for identical *n*-C_7H_{16} and *n*-$C_{10}H_{22}$ droplet sizes. Both cases are simulated for identical initiation energies and ambient composition ($X_{O2}/X_{O3}/X_{N2}$ = 21%/5%/74%).

For *n*-$C_{10}H_{22}$, vaporization at the ambient conditions results in initial stratified fuel vapor/air mixtures surrounding the drop that are all outside the fully premixed lean flammability limit, LFL (0.8% by volume [8]). The liquid droplet surface temperature heats up to ~ 0.12 s to provide enriched vapor concentrations near the surface, cf. Figure 6.6 (a) and 7 (e). In comparison, for *n*-C_7H_{16} droplet, while the outer surface temperature approaches the saturation temperature very quickly after the ignition source is provided, the *n*-$C_{10}H_{22}$ liquid droplet slowly progresses towards attaining a similar temperature distribution but with different magnitude. The heating time of the droplet dictates the gas phase fuel vapor distribution which can be seen in Figure 6.7 (b) and (f). Figure 6.8 highlights the early ignition dynamics of *n*-$C_{10}H_{22}$ droplet leading up to the attainment of a self-sustaining cool flame burn. Immediately after the ignition energy is provided at t = 0, there is a sudden rise in the peak gas temperature which exceeds ~ 820 K (Figure 6.6 (a),

Figure 6.8 (d)). This is due to the energy release from the reactions of the fuel vapor with the atomic O (at ~ 0.005 s within a spatial location of $2.0 \leq r/r_d \leq 3.0$) resulting from the endothermic decomposition of O_3 (Figure 6.8 (f)). Even though *n*-$C_{10}H_{22}$ has a higher flash point temperature, ~ 350 ppm of fuel vapor is present in the vicinity of the droplet ($r/r_d \sim 2.0$, Figure 6.8 (f)) during this stage but is rapidly depleted reacting with the atomic O undergoing H abstraction reactions (sudden cusp in fuel mole fraction). A critical pool of OH radical distribution (< 45 ppm) is formed which in turn reacts with available fuel vapor and increases the local temperature (Figure 6.8 (h)). This initial temperature ramping contributes to the droplet heating up. In the liquid phase heating time, as the partially premixed fuel is depleted in the inward volume, the energy decays with time while propagating towards the droplet (Figure 6.6 (a)) until it attempts to re-ignite the next available fuel vapor layer under lean condition. However, this initial attempt consumes the fuel rapidly (Figure 6.8 (b), ~ 0.11 s) without establishing a steady combustion due to the lower fuel vapor availability – liquid phase temperature still not attaining a condition where a self-sustaining flammable fuel vapor is being provided (Figure 6.7 (e) and 8 (b)). Therefore, oscillatory cool flames are triggered (cf. Figure 6.6 (a), 7 (f) and 8 (d)) similar to those observed for large diameter droplets [4, 33]. By the time the second dumped cool flame reappears, liquid phase droplet surface temperature approaches ~ 400 K at which enhanced fuel evaporation is established which is sufficient to establish a steady cool flame combustion (cf. Figure 6.6 (a) and 7 (e)). In this stable mode of operation, the peak gas temperature is ~ 807 K which is higher than the *n*-C_7H_{16} case. Contrary to the *n*-C_7H_{16} droplet, *n*-$C_{10}H_{22}$ burns at an ever-increasing burning rate (Figure 6.6 (b)) with relatively slow-evolving FSR until the droplet burns to completion. In comparison, for the *n*- $C_{10}H_{22}$

droplet, the flame repositions itself initially (after a transient cool flame initiation) at a relatively closed position than *n*-C_7H_{16} as the droplet itself acts as a 'heat sink'. The *n*-$C_{10}H_{22}$ droplet has a higher heat capacity and a higher flash point, an energy that has to be provided by the flame. It is not till ~ 0.11 s when the droplet attains a temperature well beyond its flash point (cf. Figure 6.7 (e)) during which the FSR is at its smallest value. The total energy feedback (arising from higher *n*- $C_{10}H_{22}$ cool flame temperature plus liquid phase heat capacity) at the droplet surface causes a higher burning rate trend.

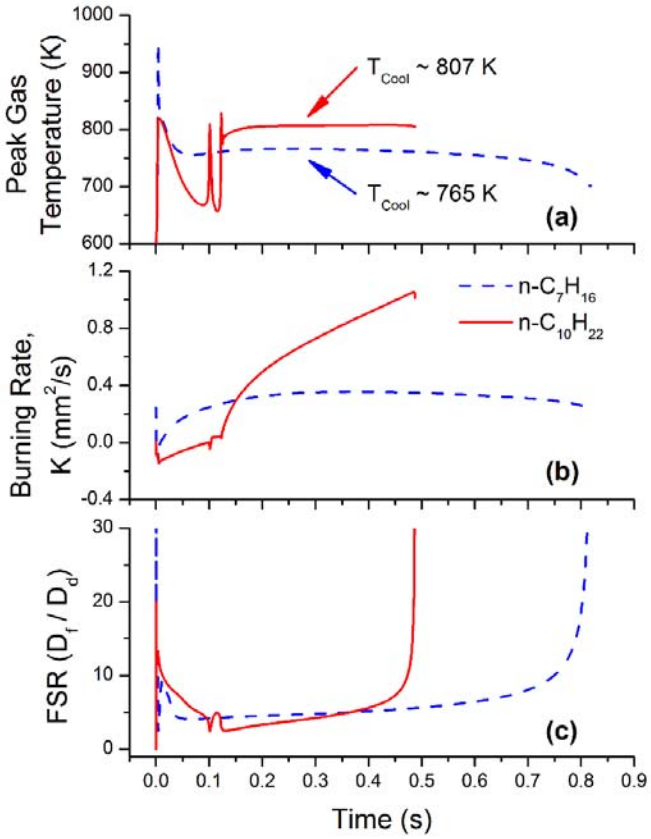

Figure 6.6 Simulated comparison of droplet combustion characteristics of *n*-C_7H_{16} and *n*-$C_{10}H_{22}$ sub-millimeter sized droplets. (a) peak gas temperature (K), (b) burning rate, K (mm^2/s) and (c) flame stand-off ratio (D_f/D_d). Simulation conditions: D_o = 0.5 mm, X_{O2} = 21%, X_{O3} = 5% and balance N_2. Ambient condition: P = 1 atm, T = 298 K. Identical trapezoidal temperature profile as ignition source having an energy deposition of ~ 0.39 J for both simulations.

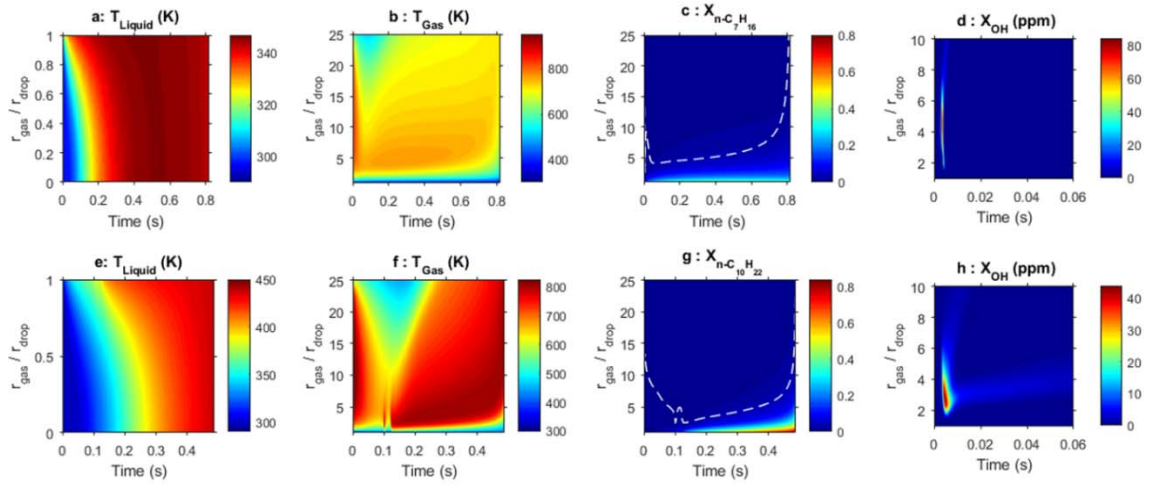

Figure 6.7 Spatiotemporal evolution of liquid phase droplet temperature (a, d), gas phase temperature (b, f), gas phase fuel mole fraction (c, g) and OH mole fraction (d, h; illustrated only up to initial transient of 0.06 s). D_o = 0.5 mm, X_{O2} = 21%, X_{O3} = 5% and balance N_2. Ambient condition: P = 1 atm, T = 298 K. Identical ignition source profile and energy deposition for both simulations. Top row: *n*-C_7H_{16}, bottom row: *n*-$C_{10}H_{22}$. The dashed line in subplots (c) and (g) denotes the flame stand-off ratio (FSR) based on maximum temperature location.

There exists a distinct difference between *n*-C_7H_{16} and *n*-$C_{10}H_{22}$ as to how the initiation and development of stable cool flame burning take place. For the case of low flash point fuel, i.e. *n*-C_7H_{16}, immediately after the ignition energy is provided, the inner atomic 'O' rich zone (resulting from O_3 decomposition) reacts with the evaporated fuel charge and thus a sudden consumption of fuel is observed (cf. Supplementary Figure 6.S4 (e) and (f)). In the vicinity of the droplet, the fuel vapor reduces from ~ 14000 ppm to ~ 5100 ppm. Atomic O participates in H abstraction reaction with the fuel forming OH radicals in this region. A net OH radical pool of ~ 80 ppm is observed to be formed which reacts with the fuel vapor participating in additional H abstraction reaction. The energy released from *n*-C_7H_{16} + OH = *n*-C_7H_{15} + H_2O reaction contributes to a sharp and almost instantaneous rise in temperature. Among the two competing 'H' abstraction reactions of the fuel with O and OH, the reaction rate of the latter is nearly 50 times higher and therefore

contributes significantly to the establishment of a stable combustion when sufficient fuel vapor is available to provide the necessary heat of reaction for sustaining the burning behavior. It should be noted that the OH chain branching should be restrictive enough so that the system does not undergo an auto-thermal acceleration to a high-temperature burn.

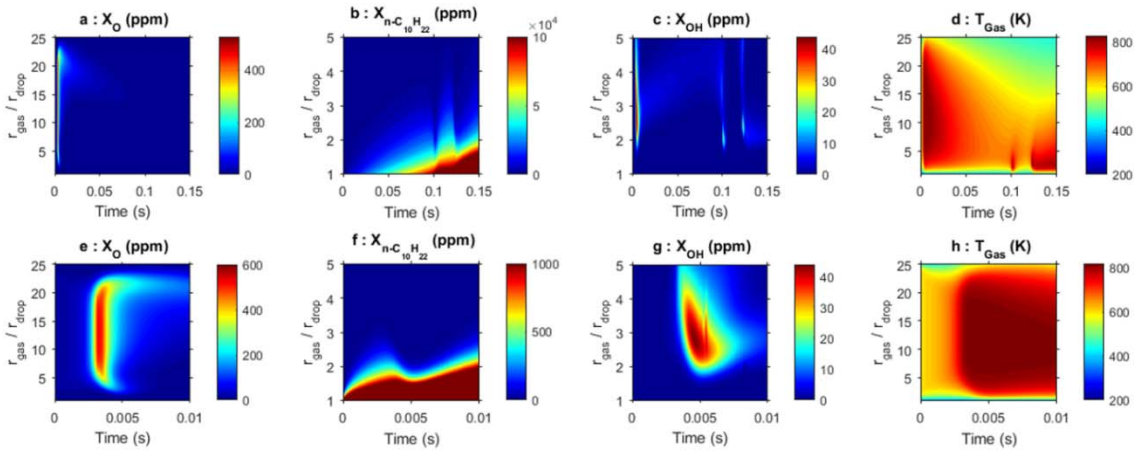

Figure 6.8 Spatiotemporal evolution of atomic O mole fraction (a, e), fuel vapor (b, f), OH mole fraction (c, g) and gas phase temperature (d, h) for *n*-$C_{10}H_{22}$ droplet. D_o = 0.5 mm, X_{O2} = 21%, X_{O3} = 5% and balance N_2. Ambient condition: P = 1 atm, T = 298 K. Top row presents the temporal range where the system has evolved to a self-sustaining cool flame burning mode (t = 0.15 s) and the bottom row presents the evolution prior to ignition (t = 0.01 s).

In contrast, for *n*-$C_{10}H_{22}$, the fuel vapor available prior to ignition is significantly lower ~ 350 ppm but still adequate to react with the atomic O (Figure 6.8 (f) and supplementary Figure 6.15) forming OH radicals via H abstraction reactions. The OH radical mole fraction prior to ignition at 0.005 seconds near the droplet surface vicinity is ~ 40 ppm (Figure 6.8 (g)) which is approximately a factor of two lower than that of the *n*-C_7H_{16} case. This initially formed OH radical pool reacts with the available fuel vapor (*n*-$C_{10}H_{22}$ + OH = *n*-$C_{10}H_{21}$ + H_2O) thereby increasing the temperature to ~ 800 K forming a moderate temperature region that drives the droplet to vaporize more fuel to establish a lean fuel-oxidizer mixture. However, due to the higher flash point temperature of *n*-$C_{10}H_{22}$,

the fuel vapor does not attain the critical condition in the first attempt. As the OH concentration evolves due to transport and reaction kinetics, at ~ 0.11 s ~ 20 ppm OH is found to be present near the droplet surface which subsequently increases the temperature to ~ 800 K very close to the droplet surface ($r/r_d \sim 2.0$). This sharp rise in the temperature very close to droplet surface ensures a further increase in the fuel vapor concentration (Figure 6.8 (b)) and diffuses further outward in the radial direction which takes place in between ~ 0.10 and 0.12 seconds. During this stage, the fuel vapor and OH radical concentration attain the critical limit which is sufficient to transition the system to a stable self-sustaining cool flame burn. This transient behavior of *n*-$C_{10}H_{22}$ fuel vapor evolution prior to the establishment of stable cool flame is further temporally illustrated at fixed radial distances (r/r_d = 1.0, 2.0, and 3.0) in the supplementary Figure 6.16. Unlike *n*-C_7H_{16}, where the O_3 decomposed atomic O generates the required OH radical to react with the fuel vapor and increase the temperature to initiate a stable cool flame burn, the larger flash point temperature *n*-$C_{10}H_{22}$ due to its slowly evolving fuel vapor mixture and its ability to attain a lean flammable mixture induces significant time lag to attain the critical condition sufficient to establish a low temperature burn. For *n*-$C_{10}H_{22}$ the system undergoes three attempts to achieve the required condition. Due to the larger time lag, some of the atomic O undergoes recombination through O + O (+M) = O_2 (+M) due to the unavailability of a large concentration of fuel vapor in the ambient and in the vicinity of the droplet. This suggests that other higher molecular weight straight chain alkanes e.g. *n*-dodecane (*n*-$C_{12}H_{26}$) can be ignited and established as a stable cool flame burn with a higher O_3 seeded environment so that sufficient O is available in the environment as the liquid fuel heats up to provide the necessary fuel vapor prior to stable cool flame.

6.4.4 EFFECT OF O_3 LOADING ON COOL FLAME BURN AT ATMOSPHERIC AND HIGHER PRESSURE

The impact of ozone (O_3) loading for different droplet sizes and higher pressure is also investigated in this effort. Numerical results are presented for two different initial diameters (D_o = 0.1, 0.5 mm) with ignition source of ~ 0.05 J and ~ 0.39 J respectively, but with different levels of O_3 mole fraction systematically exchanged with nitrogen (N_2). The effect of O_3 is only presented for *n*-heptane here. For *n*-decane similar characteristics are observed but for a slightly different ozone seeding range. Figure 6.9 summarizes the predicted droplet burning histories and peak gas temperature profiles. Irrespective of initial droplet diameter, there exists a minimum threshold O_3 level that results in a quasi-steady cool flame burn. For X_{O3} = 1.0%, both droplet diameters require significantly longer time to ignite and subsequently exhibit unsteady combustion that fails to transition to a quasi-steady burning behavior. As the O_3 loading increases (e.g. X_{O3} = 2.0%), a cool flame burn is established for both droplet sizes and a complete burn is observed. Quasi-steady cool flame droplet burning with an increased burning rate (i.e. greater slope in $(D/D_o)^2$ history) is established with further increase in the initial O_3 seeding level. Increased O_3 seeding level also leads to the more rapid inception of the partially premixed burning stage [34]. The simulations indicate that there exists an upper limit of O_3 seeding level above which only a high-temperature hot flame droplet burning occurs. However, this upper limit of O_3 seeding level is also dependent on the initial droplet diameter. For example, the limiting seeding level, $X_{O3,\,upper,}$ above which only high-temperature burning is observed for D_o = 0.5 mm is X_{O3} > 5.0 %. However, droplets having an initial diameter of 0.1 mm never transition to high temperature burning at 1 atm for any of the O_3 seeding levels studied

(X_{O3} < 8.0 %). Though the induction time decreases and vice versa for the rate of heat release with increased O_3 seeding, the peak gas temperature fails to reach the values to that of the 0.5 mm case. This is due to the lower heat generation limited by the flammable partially premixed vapor/oxidizer volume surrounding the droplet relative to the heat loss to surroundings at this smaller drop diameter. Thus, smaller initial drop diameters characteristic of freely falling droplet experiments favor cool flame droplet diameter for the same O_3 seeding level.

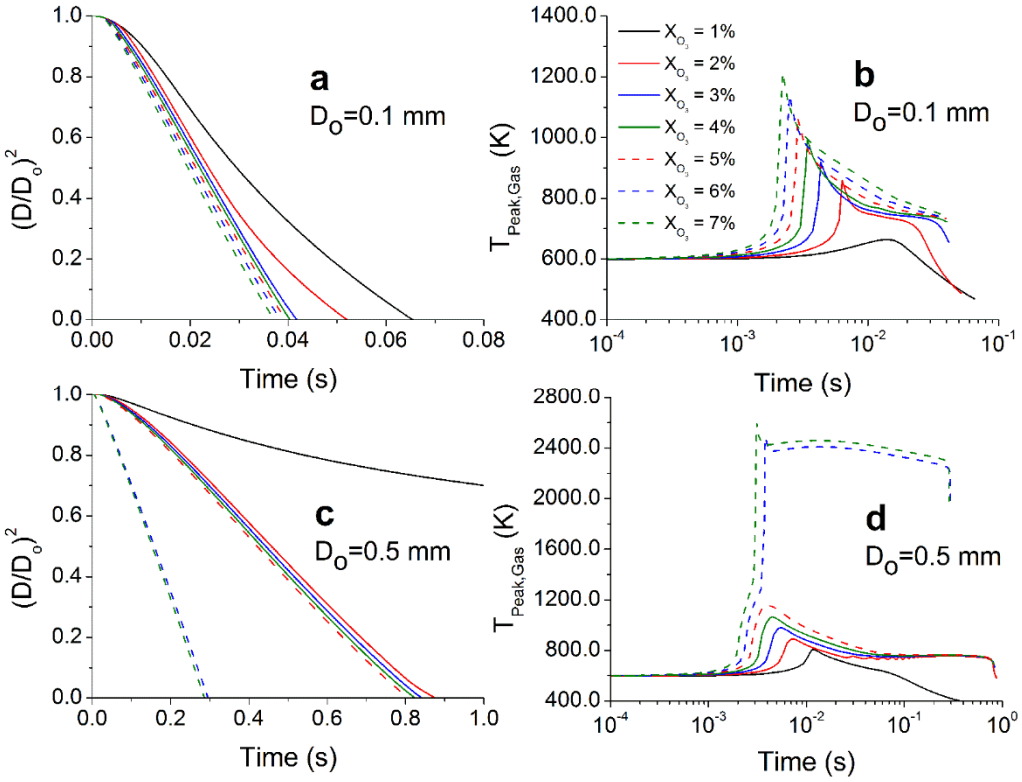

Figure 6.9 Effect of ozone (O_3) on droplet burning history of *n*-C_7H_{16} droplet and peak gas temperature profiles for D_o = 0.1 mm (subplot a, b) and D_o = 0.5 mm (subplot c, d). X_{O2} = 21%, mole fractions of O_3 are as indicated in the legend with balance N_2. Ambient condition: P = 1 atm, T = 298 K.

Figure 6.10 summarizes the numerical predictions of the peak gas temperature for the 0.1 mm (Figure 6.10 (a)) and 0.5 mm (Figure 6.10 (b)) initial droplet exposed to 25 atm

pressure and 298 K ambient temperature. Even though a number of O_3 seeding levels were simulated, the results are presented for two different levels of O_3 mole fractions of 0.5% and 2.0% where parametric exchanges of O_2/N_2 are considered. The ozone levels are so chosen because at the elevated pressure condition the smallest droplet size (D_o = 0.1 mm) initiates a cool flame burn at the lower O_3 loading (0.5%) and a hot flame transition readily takes place for the 2.0% seeding. It can be seen that irrespective of the droplet diameter, the initiation process attempts to achieve an initial peak gas temperature of either ~ 620 K (X_{O3} = 0.5%) or ~ 690 K (X_{O3} = 2.0%) depending on the O_3 loading condition. As the Figure 6.10 illustrates, at the elevated pressure condition, a combination of smaller droplet size (0.1 mm) and low O_3 seeding (0.5%) yields only low-temperature burn. For the identical case when the O_3 mole fraction is increased to 2%, the dynamics of the system changes completely and it shifts towards hot-ignition preceded by a significantly longer induction time (~ 0.027 s) during which a peak gas temperature of ~ 690 K is maintained. This is indicative of a comparatively longer low-temperature burn before the system transitions to a hot flame. The hot flame is only maintained for ~ 30% of the total burn time. With larger diameter droplet (D_o = 0.5 mm), for any of the O_3 loading studied here- the system inevitably undergoes hot ignition and a subsequent quasi-steady high-temperature burn.

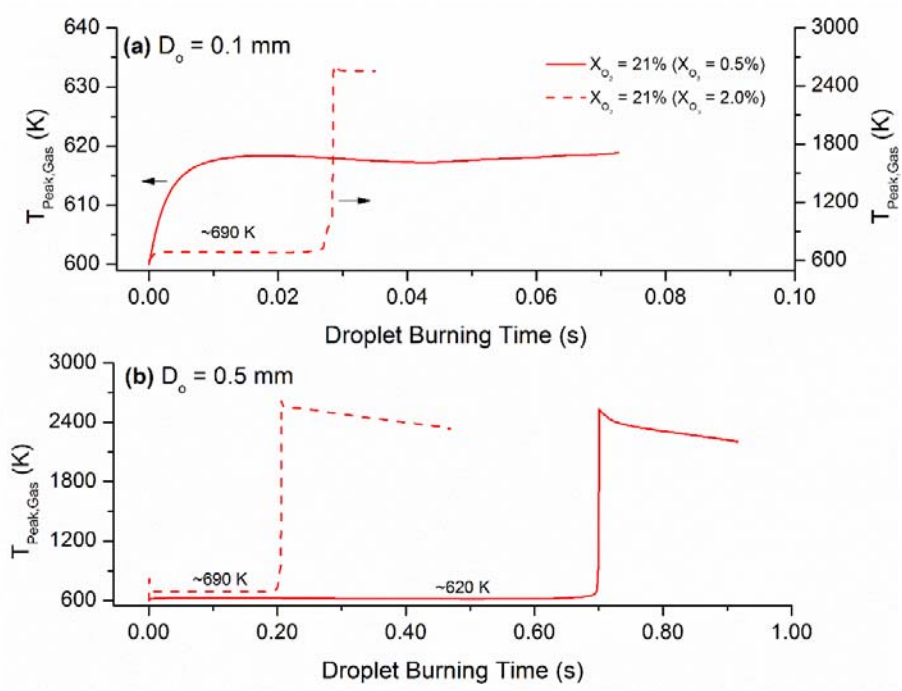

Figure 6.10 Effect of ozone (O_3) on peak gas temperature profiles at higher ambient pressure for *n*-C_7H_{16} droplets (a) D_o = 0.1 mm and (b) D_o = 0.5 mm. The mole fraction of ozone is indicated in the legend. Ambient condition: P = 25 atm, T = 298 K.

It is clear that there is a direct relationship between O_3 concentration and the time to hot ignition transition at elevated pressure conditions. O_3 molar concentration as low as 0.5% results in the establishment of high-temperature burning (c.f. Figure 6.10 (b)). The role of pressure is also investigated by comparing the burning characteristics of the 0.5 mm droplet at 1 atm (3% O_3, producing cool flame) and 25 atm (0.5% O_3). The results are presented in Figure 6.11. At atmospheric pressure, the relative importance of H_2O_2 in transitioning the gas phase reactive mixture to hot ignition via H_2O_2 (+M) = OH + OH (+M) is much less pronounced than the elevated pressure scenario where the O_3 loading is purposely made small. At higher pressure, the drastic consumption of H_2O_2 and the evolution of gas phase temperature and OH radicals (cf. subplots in bottom row) manifest the impact of pressure in shifting the system to hot ignition.

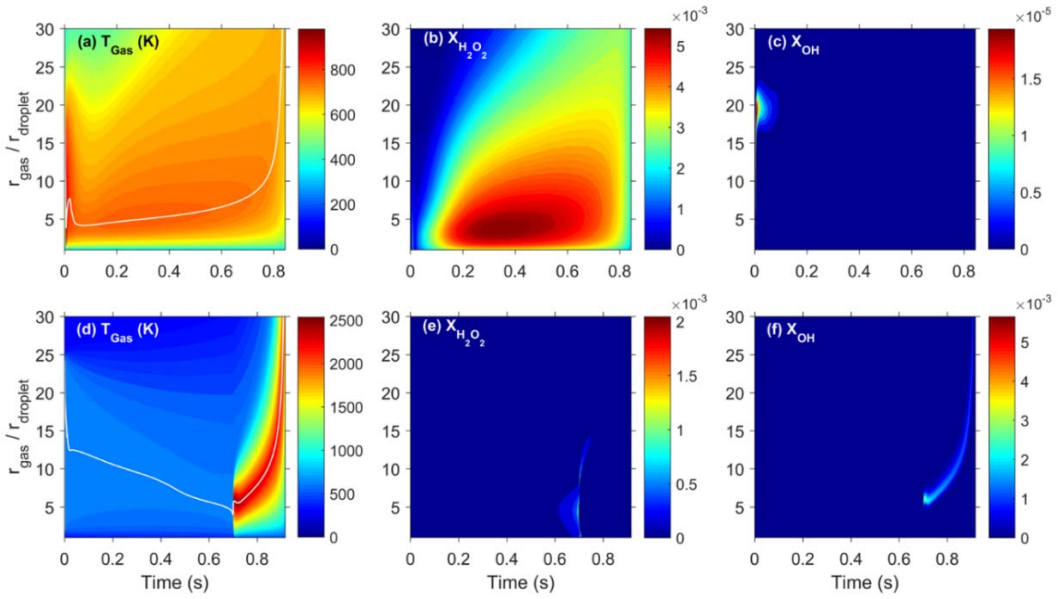

Figure 6.11 Comparison of the spatiotemporal evolution of gas phase temperature (subplot a, d), H_2O_2 mole fraction (subplot b, e) and OH radical mole fraction (subplot c, f) distributions for *n*-C_7H_{16} droplet combustion at different ambient pressures. Simulation conditions: D_o = 0.5 mm, X_{O2} = 21%, X_{O3} = 3%, balance X_{N2}, P = 1 atm (subplot a-c); D_o = 0.5 mm, X_{O2} = 21%, X_{O3} = 0.5%, balance X_{N2}, P = 25 atm (subplot d-f). The maximum value for the color bar has been reduced by a factor of 4.0 for subplots (c) and (e) for visual clarity.

6.5 CONCLUDING REMARKS

Isolated *n*-alkane (*n*-C_7H_{16} and *n*-$C_{10}H_{22}$) droplet combustion was computationally investigated for different initial diameters (D_o = 0.1, 0.5 mm), ambient pressures (1, 25 atm) with selected levels of O_3 in the surrounding. The prime objective of this study was to explore whether cool flame droplet burning can be directly established for sub-millimeter sized *n*-alkane droplets at conditions where radiative extinction is unlikely. Computations were performed for *n*-C_7H_{16} and *n*-$C_{10}H_{22}$ fuels, as low and high flash point exemplars. Summarizing the results of this analysis:

1. The required initiation energy for igniting low and high flashpoint (relative to ambient temperature) fuel droplets differ as a result of combustion of partially premixed flammable vapor present in the low flashpoint case. The rapid combustion of this

mixture provides additional energy to sustain burning over the transition from partially premixed to diffusive burning. In the case of high flash temperature fuel (n-$C_{10}H_{22}$), the droplet liquid must be heated above its flash temperature by the initiation energy, which must also provide the energy to sustain the transition to diffusive burning.

2. Without ozone present, the fuel/vapor temperature required to initiate the burning of the low flash point fuel and the rate and duration of vaporization of the droplet makes it difficult to avoid the transition to hot flame conditions.

3. Without ozone present, and with the limited vaporization typical of high flash point fuels, the initiation energy can be controlled in terms of rate and duration to achieve cool flame burning without incurring hot flame conditions.

4. The seeding of O_3 into the surrounding air offers an ability to reduce the temperature (and therefore initiation energy required) to initiate gas phase reactions of the flammable vapor/air mixtures. The amount of O_3 seeding affects the rate of energy release occurring at and subsequent to reaction initiation.

5. For fixed droplet diameter, ambient temperature, a level of initiation energy can be found such that:
    a. For both low and high flash point cases, there exists a threshold minimum O_3 concentration to institute quasi-steady cool flame droplet burning.
    b. For both low and high flash point cases, there exists a threshold maximum O_3 concentration above which hot flame burning will always occur.

6. Combined effects of initial droplet diameter, ignition source, and ambient O_3 concentration play a major role in achieving direct initiation of quasi-steady cool flame

burning or hot flame burning. At elevated pressure (here, 25 atm), the requirement for threshold maximum O_3 concentration that drives the system to hot ignition decreases significantly due to the pressure dependence of reactions forming HO_2 and especially the H_2O_2 (+M) = OH + OH (+M).

6.6 SUPPLEMENTARY FIGURES

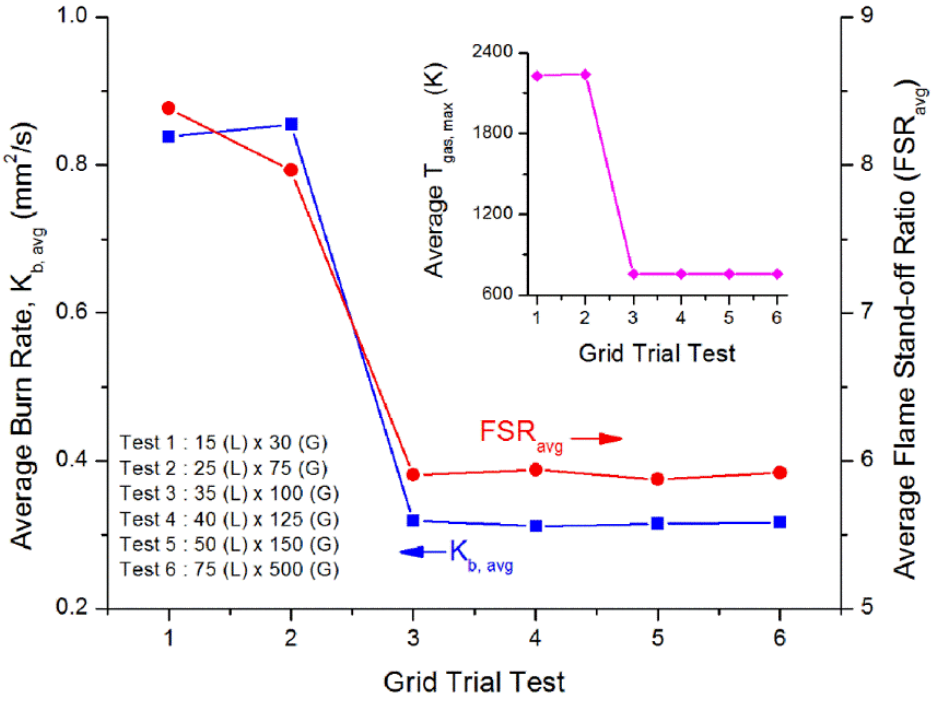

Figure 6.12 Grid independence test results for different droplet combustion marker targets of *n*-C_7H_{16} droplet combustion. D_o = 0.5 mm, X_{O3} = 5% and X_{O2} = 21% with balance N_2. Ambient conditions: P = 1 atm and T = 298 K.

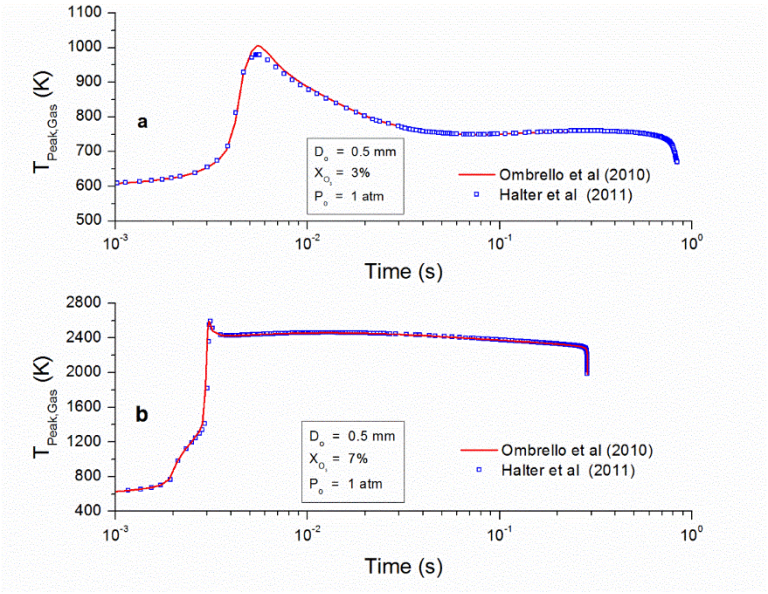

Figure 6.13 Influence of different ozone kinetics on the predicted peak gas temperature evolution for *n*-C_7H_{16} droplet (a) X_{O3} = 3% and (b) X_{O3} = 7%. D_o = 0.5 mm, X_{O2} = 21%, balance X_{N2}. Ambient conditions: P = 1 atm and T = 298 K.

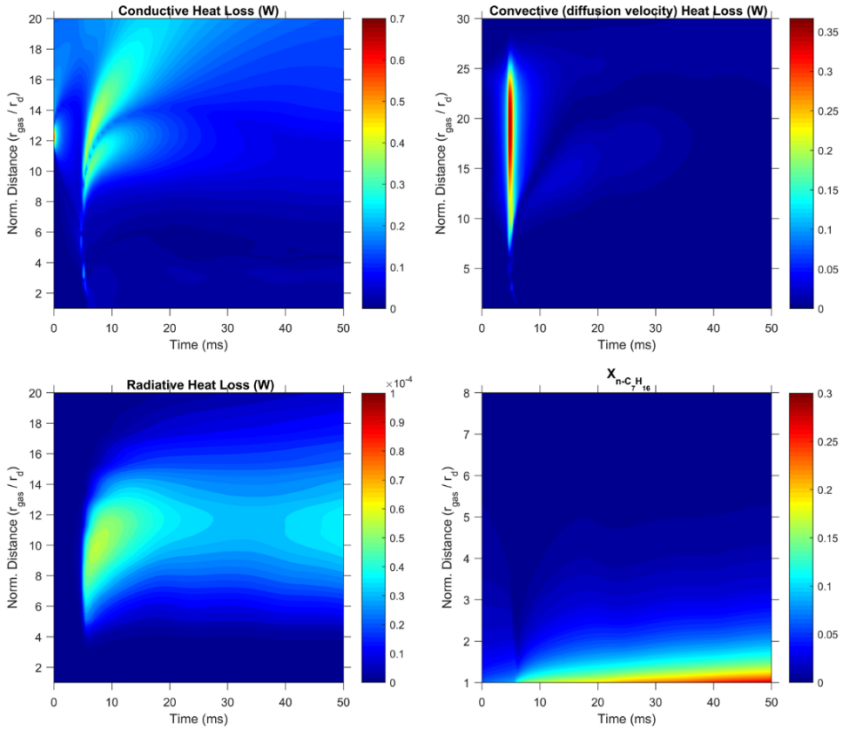

Figure 6.14 Spatiotemporal evolution of conductive, convective, radiative heat loss and fuel vapor mole fraction for *n*-C_7H_{16} fuel, D_o = 0.5 mm, X_{O2} = 21%, X_{O3} = 3%, balance X_{N2}. Ambient condition: P = 1 atm and T = 298 K.

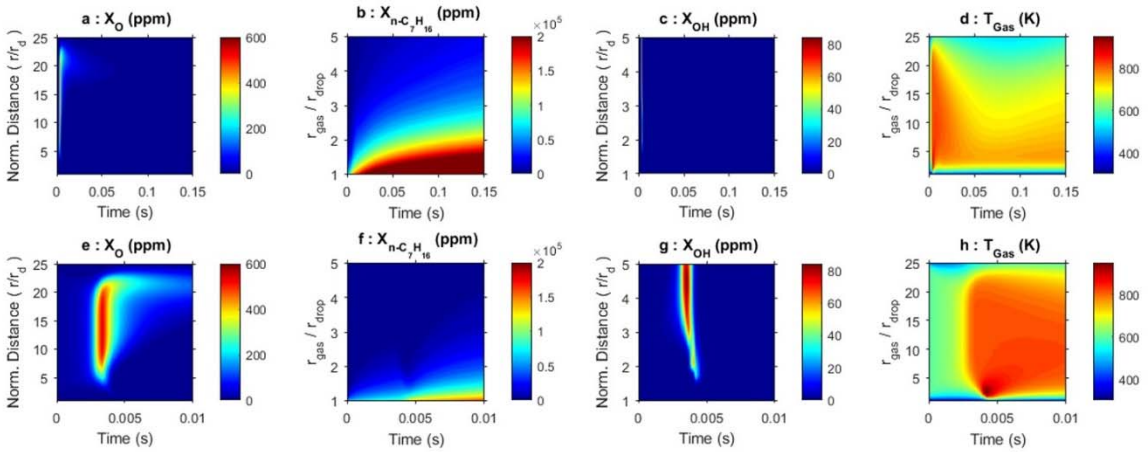

Figure 6.15 Spatiotemporal evolution of atomic O mole fraction (a, e), fuel vapor (b, f), OH mole fraction (c, g) and gas phase temperature (d, h) for *n-C_7H_{16}* droplet. D_o = 0.5 mm, X_{O2} = 21%, X_{O3} = 5% and balance N_2. Ambient condition: P = 1 atm, T = 298 K. Top row presents an extended temporal range where the system has evolved to a self-sustaining cool flame burning mode (t = 0.15 s) and the bottom row presents the evolution prior to ignition (t = 0.01 s).

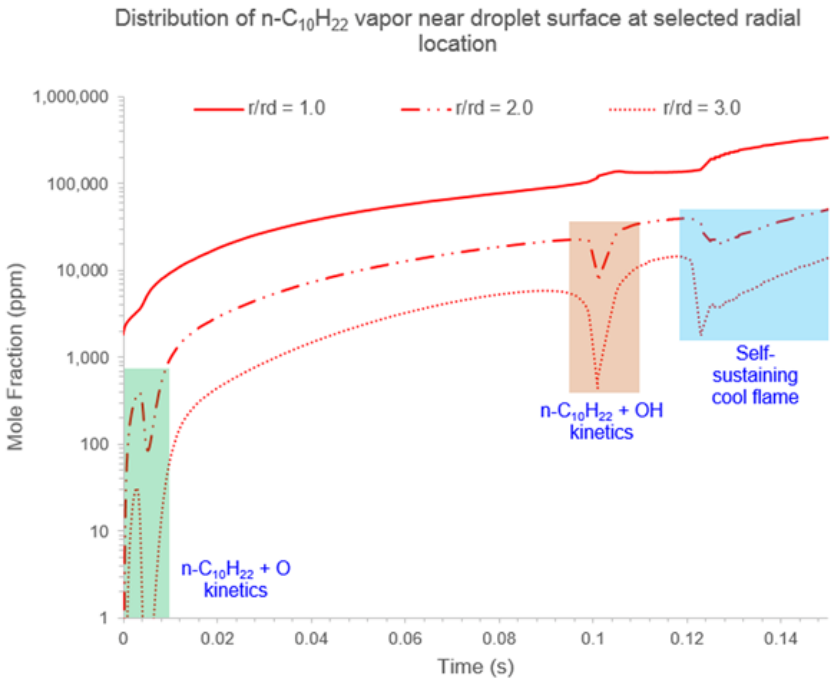

Figure 6.16 Temporal evolution of *n-$C_{10}H_{22}$* fuel vapor at different radial location adjacent to liquid the surface. D_o = 0.5 mm, X_{O2} = 21%, X_{O3} = 5%, balance X_{N2}, P = 1 atm and T = 298 K. The simulated results are shown up to 0.15 s (inception of stable cool flame region).

6.7 REFERENCES

[1] V. Nayagam, D.L. Dietrich, P.V. Ferkul, M.C. Hicks, F.A. Williams, Can cool flames support quasi-steady alkane droplet burning?, Combust. Flame 159 (2012) 3583-3588.

[2] D. Dietrich, V. Nayagam, M. Hicks, P. Ferkul, F. Dryer, T. Farouk, B. Shaw, H. Suh, M. Choi, Y. Liu, C.T. Avedisian, F. Williams, Droplet Combustion Experiments Aboard the International Space Station, Microgravity Sci. Technol. 26 (2014) 65-76.

[3] T.I. Farouk, F.L. Dryer, Isolated n-heptane droplet combustion in microgravity: "Cool Flames" – Two-stage combustion, Combust. Flame 161 (2014) 565-581.

[4] T.I. Farouk, M.C. Hicks, F.L. Dryer, Multistage oscillatory "Cool Flame" behavior for isolated alkane droplet combustion in elevated pressure microgravity condition, Proc. Combust. Inst. 35 (2015) 1701-1708.

[5] T.I. Farouk, D. Dietrich, F.E. Alam, F.L. Dryer, Isolated n-decane droplet combustion – Dual stage and single stage transition to "Cool Flame" droplet burning, Proc. Combust. Inst. 36 (2017) 2523-2530.

[6] G.J. Minkoff, C.F.H. Tipper, The Chemistry of Combustion Reactions, Butterworths Publishing Co., London, England, 1962.

[7] S.W. Benson, The kinetics and thermochemistry of chemical oxidation with application to combustion and flames, Prog. Energy Combust. Sci. 7 (1981) 125-134.

[8] NOAA, n-Decane Chemical Datasheet. https://cameochemicals.noaa.gov/chemical/3070 (accessed 28th November 2016).

[9] NOAA, n-Heptane Chemical Datasheet. https://cameochemicals.noaa.gov/chemical/831 (accessed 28th November 2016).

[10] A.J. Marchese, F.L. Dryer, V. Nayagam, Numerical modeling of isolated n-alkane droplet flames: initial comparisons with ground and space-based microgravity experiments, Combust. Flame 116 (1999) 432-459.

[11] S. Kumagai, T. Sakai, S. Okajima, Combustion of free fuel droplets in a freely falling chamber, Symp. (Int.) Combust. 13 (1971) 779-785.

[12] S.H. Won, B. Jiang, P. Diévart, C.H. Sohn, Y. Ju, Self-sustaining n-heptane cool diffusion flames activated by ozone, Proc. Combust. Inst. 35 (2015) 881-888.

[13] C.B. Reuter, S.H. Won, Y. Ju, Experimental study of the dynamics and structure of self-sustaining premixed cool flames using a counterflow burner, Combust. Flame 166 (2016) 125-132.

[14] C.B. Reuter, S.H. Won, Y. Ju, Flame structure and ignition limit of partially premixed cool flames in a counterflow burner, Proc. Combust. Inst. 36 (2017) 1513-1522.

[15] A.J. Marchese, F.L. Dryer, R.O. Colantonio, V. Nayagam, Microgravity combustion of methanol and methanol/water droplets: Drop tower experiments and model predictions, Symp. (Int.) Combust. 26 (1996) 1209-1217.

[16] A.J. Marchese, F.L. Dryer, R.O. Colantonio, Radiative effects in space-based methanol/water droplet combustion experiments, Symp. (Int.) Combust. 27 (1998) 2627-2634.

[17] T. Farouk, F.L. Dryer, Microgravity droplet combustion: effect of tethering fiber on burning rate and flame structure, Combust. Theory Modell. 15 (2011) 487-515.

[18] T.I. Farouk, F.L. Dryer, On the extinction characteristics of alcohol droplet combustion under microgravity conditions – A numerical study, Combust. Flame 159 (2012) 3208-3223.

[19] W. Sun, Z. Chen, X. Gou, Y. Ju, A path flux analysis method for the reduction of detailed chemical kinetic mechanisms, Combust. Flame 157 (2010) 1298-1307.

[20] S. Dooley, S. Won, F. Haas, J. Santner, Y. Ju, F. Dryer, T. Farouk, Development of Reduced Kinetic Models for Petroleum-Derived and Alternative Jet Fuels, 50th AIAA/ASME/SAE/ASEE Joint Propulsion Conference, Cleveland, Ohio, 2014.

[21] H.J. Curran, P. Gaffuri, W.J. Pitz, C.K. Westbrook, A Comprehensive Modeling Study of n-Heptane Oxidation, Combust. Flame 114 (1998) 149-177.

[22] C.K. Westbrook, W.J. Pitz, O. Herbinet, H.J. Curran, E.J. Silke, A comprehensive detailed chemical kinetic reaction mechanism for combustion of n-alkane hydrocarbons from n-octane to n-hexadecane, Combust. Flame 156 (2009) 181-199.

[23] T.E. Daubert, R.P. Danner, Physical and Thermodynamic Properties of Pure Chemicals, Hemisphere Publishing Corp. , New York, USA, 1989.

[24] F. Halter, P. Higelin, P. Dagaut, Experimental and Detailed Kinetic Modeling Study of the Effect of Ozone on the Combustion of Methane, Energy Fuels 25 (2011) 2909-2916.

[25] T. Ombrello, S.H. Won, Y. Ju, S. Williams, Flame propagation enhancement by plasma excitation of oxygen. Part I: Effects of O3, Combust. Flame 157 (2010) 1906-1915.

[26] G.D. Smekhov, L.B. Ibraguimova, S.P. Karkach, O.V. Skrebkov, O.P. Shatalov, Numerical simulation of ignition of a hydrogen-oxygen mixture in view of electronically excited components, High Temp. 45 (2007) 395-407.

[27] S. Schnaubelt, O. Moriue, T. Coordes, C. Eigenbrod, H. Rath, Detailed numerical simulations of the multistage self ignitio process of n-heptane isolated droplets and their verification by comparison with microgravity experiments, Proc. Combust. Inst. 28 (2000) 953 - 960.

[28] A. Marchese, T. Vaughn, K. Kroenlein, F. Dryer, Ignition delay of fatty acid methyl ester fuel droplets: microgravity experiments and detailed numerical modeling, Proc. Combust. Inst. 33 (2011) 2021 - 2030.

[29] T.I. Farouk, Y.C. Liu, A.J. Savas, C.T. Avedisian, F.L. Dryer, Sub-millimeter sized methyl butanoate droplet combustion: Microgravity experiments and detailed numerical modeling, Proc. Combust. Inst. 34 (2013) 1609-1616.

[30] H. Yamada, K. Suzaki, A. Tezaki, Y. Goto, Transition from cool flame to thermal flame in compression ignition process, Combust. Flame 154 (2008) 248-258.

[31] K. Zhang, C. Banyon, J. Bugler, H.J. Curran, A. Rodriguez, O. Herbinet, F. Battin-Leclerc, C. B'Chir, K.A. Heufer, An updated experimental and kinetic modeling study of n-heptane oxidation, Combust. Flame 172 (2016) 116-135.

[32] G. Paczko, N. Peters, K. Seshadri, F.A. Williams, The role of cool-flame chemistry in quasi-steady combustion and extinction of n-heptane droplets, Combust. Theory Modell. 18 (2014) 515-531.

[33] A. Cuoci, M. Mehl, G. Buzzi-Ferraris, T. Faravelli, D. Manca, E. Ranzi, Autoignition and burning rates of fuel droplets under microgravity, Combust. Flame 143 (2005) 211-226.

[34] J.B. Masurier, F. Foucher, G. Dayma, P. Dagaut, Homogeneous Charge Compression Ignition Combustion of Primary Reference Fuels Influenced by Ozone Addition, Energy Fuels 27 (2013) 5495-5505.

CHAPTER 7

OSCILLATORY COOL FLAME BEHAVIOR OF SUB-MILLIMETER SIZED N-ALKANE DROPLET UNDER NEAR LIMIT CONDITIONS

7.1 ABSTRACT

This chapter reports simulation results of oscillatory cool flame burning of an isolated, sub-millimeter sized n-heptane (n-C_7H_{16}) droplet in a selectively ozone seeded nitrogen-oxygen environments at atmospheric pressure. An evolutionary one-dimensional droplet combustion code, as discussed at length in chapter 2, encompassing relevant physics and detailed chemistry was employed to explore the roles of low-temperature chemistry, ozone seeding, and dynamic flame structure on burning behaviors. For X_{O2}=21% and a range of selective ozone seeding, near-quasi-steady cool flame burning is achieved directly (without requiring hot flame initiation and radiative extinction). Under low oxygen index conditions, with 5% ozone seeding (v/v), a nearly quasi-steady cool flame is initially established that then transitions to a dynamically oscillating cool flame burning mode until the droplet is completely consumed. It is found that the oscillation is initiated by the depletion of fuel vapor-oxidizer layer evolving near the droplet surface and its dynamic re-establishment through liquid vaporization and vapor/oxidizer transport. A kinetic analysis indicates that the dynamic competition between the reaction classes- (a) degenerate chain branching and (b) chain termination/propagation - along with continuous fuel and oxygen leakage through the flame location contributes to an oscillatory burning phenomena of ever-increasing amplitude. Analysis based on single full-cycle of oscillatory burning shows that the reaction progression matrices (evolution of heat and species) for QOOH➔chain propagation/termination reactions directly scales with the gas phase temperature field. On the contrary, the QOOH➔degenerate branching reactions undergoes

three distinct stages within the same cycle. The coupled flame dynamics and kinetics suggest that in the oscillatory burning mode, kinetic processes dynamically cross through conditions characterizing the negative temperature coefficient (NTC) turnover temperature separating low temperature and NTC kinetic regimes. In addition, a parametric study is conducted to determine the role of ozone seeding level on the observed oscillation phenomena.

7.2 INTRODUCTION

Numerical analyses of large diameter n-alkane cool flame droplet burning experiments [1, 2] on board the International Space Station (ISS) [3] are yielding fundamental insights of practical relevance to engine knock and multi-stage auto-ignition [4], lean flammability [5] and spacecraft fire safety [1] and to elucidating low and negative-temperature coefficient (NTC) kinetics [6, 7]. These endeavors differ from the cool flame, gas phase premixed/non-premixed flame research [5-13] and involve heat-release/loss rate driven effects present in multi-phase, isolated sphero-symmetric droplet combustion [1-3, 14-19].

The Multi-user Droplet Combustion Apparatus (MDCA) platform on the ISS [3] has been operated in a mode to initiate cool flame droplet burning behavior over a wide range of n-alkane fuels and n-alkane/iso-alkane fuel mixtures, operating pressures, oxygen indices, and diluent compositions. Commonly, those experiments that yielded cool flame behavior, required large initial diameter droplets (D_o> ~3.0 mm) and radiative extinction of an initial, hot-flame burning mode. Comprehensive numerical analyses led to a detailed interpretation of the initiation and flame dynamics [15, 19]. In rare cases, cool flame

burning was able to be established directly, without incurring an initial hot flame mode and subsequent radiative extinction. Subsequent analyses [18] showed that the overall ignition energy resulting from hotwire heating rate and the heat release from stratified vapor/oxidizer layer oxidation near the drop surface could sufficiently reduce to initiate direct cool flame burning, especially with n-alkanes having flash points greater than the initial ambient temperature. Applying the results described in Won et al. [9] that investigated ozone seeding to reduce chemical induction times for fuel/oxidizer autoignition, numerical analyses for isolated droplet conditions with ozone seeding [20] revealed the possibility of achieving direct and sustained cool flame droplet burning behavior for even sub-millimeter sized (D_o = 0.5 mm) cases and higher n-alkane fuels. The latter results suggest that cool flame droplet burning should likely be able to be investigated in ground-based, sub-millimeter diameter experiments, yielding substantial advantages in characterizing the chemical characteristics of the cool flame droplet burning problem. Here, we extend these earlier predictions to further elucidate oscillatory droplet burning behaviors that may also be observed in such ground-based research.

Oscillatory, fully pre-vaporized diffusion flame phenomena have been extensively studied in the past through theoretical, numerical and experimental efforts [21-23]. Farouk and coworkers [17] have recently studied multi-cycle, two-stage (high temperature–cool flame) burning behavior of n-heptane (n-C_7H_{16}) at high pressure (3 atm) and in presence of carbon-dioxide (CO_2) in the diluent composition. The dynamical balance of heat generation from negative-temperature coefficient and hot ignition kinetics and principally, convective/diffusive (not radiative) heat loss to the far-field were shown to be the cause of the oscillatory observations. Cuoci et al. [19] suggested that the oscillatory behavior for n-

decane (n-$C_{10}H_{22}$) droplets (D_o~1.0-2.0 mm) could also result from the competition between progressive fuel consumption and slow evolution of gas phase n-$C_{10}H_{22}$ vapor due to reduced heat feedback to the droplet surface. While these studies provide insights into the oscillatory cool flame droplet burning for large diameter droplets, neither experimental observations themselves nor their theoretical/computational analyses forecast that such behaviors might be present for the small droplet diameters (D_o < 1.0 mm) studied in [24].

In this chapter, we numerically investigate the oscillatory cool flame behavior of O_3 assisted sub-millimeter sized (D_o=0.5 mm) n-C_7H_{16} droplet burning at atmospheric conditions (P=1 atm, T=298 K) and two reduced oxygen indices (X_{O2} = 10% and 15%) that bracket the known limiting oxygen index (LOI) (about 13%) for spherosymmetric n-heptane droplet combustion [24]. The establishment of directly induced, near quasi-steady, cool flame burning of small diameter droplets is briefly discussed first, and subsequently, conditions that result in dynamically oscillating cool flame behavior are compared with this base case. The detailed flame structures are analyzed, and the role of underlying thermo-kinetic/transport properties on oscillatory behaviors is elucidated.

7.3 NUMERICAL MODELING

This numerical study is performed using an evolving sphero-symmetric, multi-component droplet combustion code, the details of which (both the physics and the numerical schemes) have been thoroughly presented elsewhere [25, 26] and references therein. Prominent features of this one-dimensional (1-D) model are in its ability to incorporate detailed gas phase kinetics, multi-component transport considerations, spectrally resolved radiative interactions and thermal perturbations of microgravity

experimental observations that occur from the presence of tethering fibers. The results presented here were generated for an initial droplet diameter of n-C_7H_{16} fuel of 0.5 mm using two different detailed kinetic models: (a) a detailed model (652 species, 2827 elementary reactions) from reference [27]; and (b) a numerically reduced model (130 species, 565 elementary reactions) [28] which has been further refined for droplet combustion simulations [15]. Reaction sets of O_3 kinetics from Reuter et al. [5] were appended to the n-C_7H_{16} models. Lastly, n-C_7H_{16} liquid phase properties were evaluated based on the correlations reported in Daubert and Danner [29]. The kinetic model predictions were extensively validated using gas phase [9, 12, 28], as well as multi-phase experimental targets [15, 17]. The predictive quality of the reduced version against its detailed counterpart (see Supplementary Figure 7.8) were found to be excellent, including those for multi-component comparisons. Subsequently, further droplet burning predictions were generated using only the reduced kinetic version in order to reduce computational turnaround times. Selective O_3 seeded ambient levels and reduced initiation energy conditions recommended in [20] were employed here in order to assure an initial establishment of cool flame burning conditions.

All the reported simulations are for atmospheric conditions (1 atm, 298 K). The base case considers X_{O2} = 10%, X_{O3} = 5%, balance N_2 that has an oxygen index significantly lower than the n-C_7H_{16} LOI condition. The results presented are for a spatial resolution of 200 grid points (50 in the liquid and 150 in the gas phase) that confirmed a grid independent solution.

7.4 RESULTS AND DISCUSSIONS

Figure 7.1 summarizes the temporal evolution of major droplet combustion parameters - droplet diameter regression, burning rates (K_o), peak gas temperature (T_{max}), flame stand-off ratio (FSR) - as well as the droplet surface Stefan flux and liquid surface temperature for two different oxygen indices and the same ozone seeding level (5%). For the X_{O2} = 21% case, the model predicts an almost immediate establishment of a near-quasi-steady cool flame burn (within 6% of the total burn time). For this low flash point fuel (T_{flash} = 269.3 K), a significant flammable vapor/oxidizer volume is present near the droplet surface initially. Rapid consumption of the mixture results as the initiation energy leads to decomposition of the ozone in the volume, and subsequent reaction of O atoms with fuel vapor (RH + O ➔ R˙ + OH), followed by RH + OH ➔R˙ + H_2O and associated heat release. Chemically induced heat release as well as energy supplied by the initiation source provides subsequent heating of the liquid surface [20] and transition of the partially premixed reaction near the surface to diffusive cool flame burning. The predicted average quasi-steady state (QSS) cool flame temperature is ~760 K. The burning rate evolution shows a negative value during the initial phase due to the thermal expansion of the liquid droplet and then progresses through a smooth transition – increasing and then decreasing towards the end of the burn. The FSR evolution during the cool flame burn shows a continually increasing trend due to thermal buffering of the far field that leads to decreased loss of heat from the flame structure and an ever-increasing FSR as burning progresses, which is observed in prior sub-millimeter sized n-heptane experiments [24].

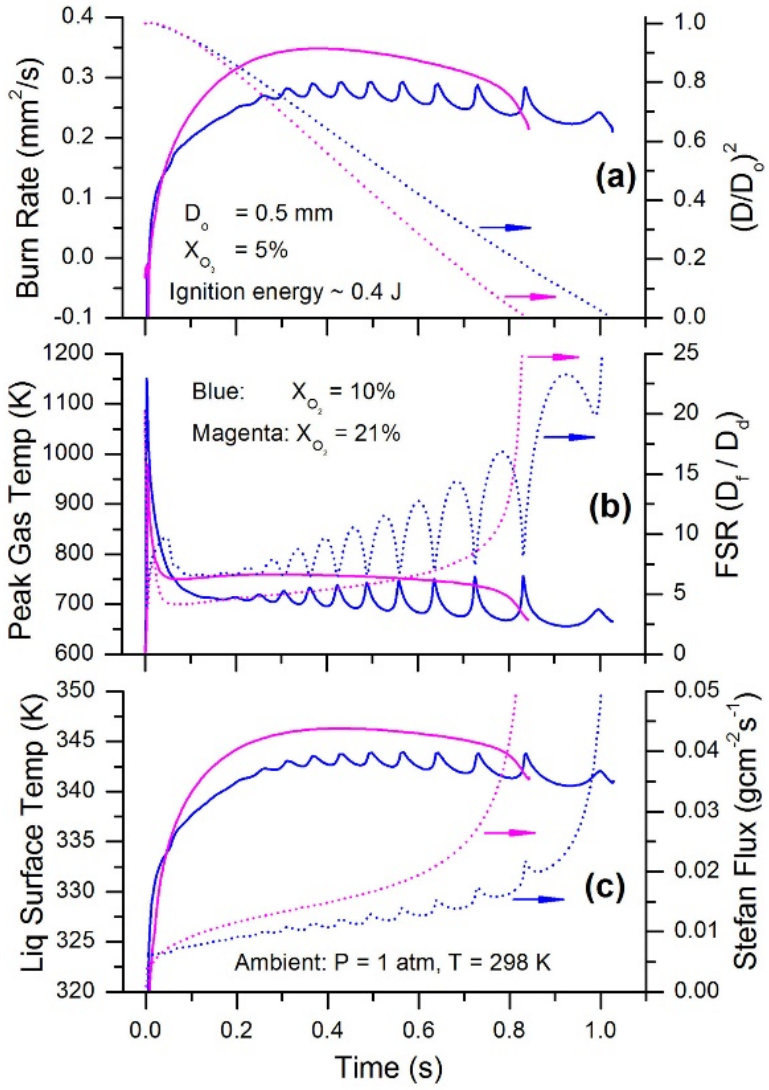

Figure 7.1 Temporal evolution of (a) droplet diameter regression and burning rate, (b) peak gas temperature and flame stand-off ratio, and (c) droplet surface temperature and Stefan flux at the droplet surface for n-heptane droplet (D_o = 0.5 mm) combustion. Ambient conditions: P = 1 atm, T = 298 K. Details of the gas compositions are in the figure text.

For the reduced oxygen index cases, a QSS cool flame is predicted to occur after an induction time of ~0.12 s, with a discernibly lower cool flame temperature of ~710 K. Lowering the ambient oxygen level increases the FSR and as a consequence, T_{max} and K_o decrease significantly from the values for 21% oxygen index. Even though the ambient oxygen index is well below the LOI conditions, reactions of the seeded ozone produce

molecular oxygen, producing a higher (effective) oxygen index. After the initial O_3 decomposition stimulates vapor phase oxidation of the fuel, and the local heat release leads to temperatures near the drop surface exceeding 1100 K, the transition to diffusive burning is unstable. The dynamic balance of diffusive-thermo-kinetic terms, as discussed in [17], stabilizes the flame temperature at around ~710 K for a brief period (till t~0.18 s), at which time an oscillatory/pulsing behavior occurs and continues until combustion ceases with complete loss of liquid phase fuel. During these pulsations, the FSR, T_{max}, and K_o progressively grow in magnitude with each successive pulsation as the droplet burning proceeds (c.f. subplot (a-c)). Consequently, the Stefan flux at the droplet surface also follows a similar trend. The droplet diameter regression does not show any distinctive changes in its evolution despite the oscillatory pattern of other parameters, e.g. T_{max} and FSR. A unique feature of the oscillation is that at every successive cycle, the cyclic amplitudes of FSR and T_{max} increase but their oscillations are out of phase. During each cycle, the FSR maximum occurs for the lowest peak flame temperature, with FSR decreasing to its minimum value as the local flame temperature increases to its maximum. The differences between the minimum and maximum FSRs and local maximum and the minimum flame temperatures grow over subsequent cycles with a notable decrease in cycle frequency. For example, at ~0.42 s, the peak gas temperature increases to ~738 K from a plateau of ~696 K, dropping to ~692 K in the next cycle after reaching a value of ~ 742 K. During this time period, the FSR oscillates from ~9.6 to ~6.5 and then ~10.5 to ~ 6.7. With an increase in the ambient index (i.e. X_{O2} = 15%), a similar pulsing pattern was observed but having lower amplitude and higher frequency (see Figure 7.8 in the supplementary section).

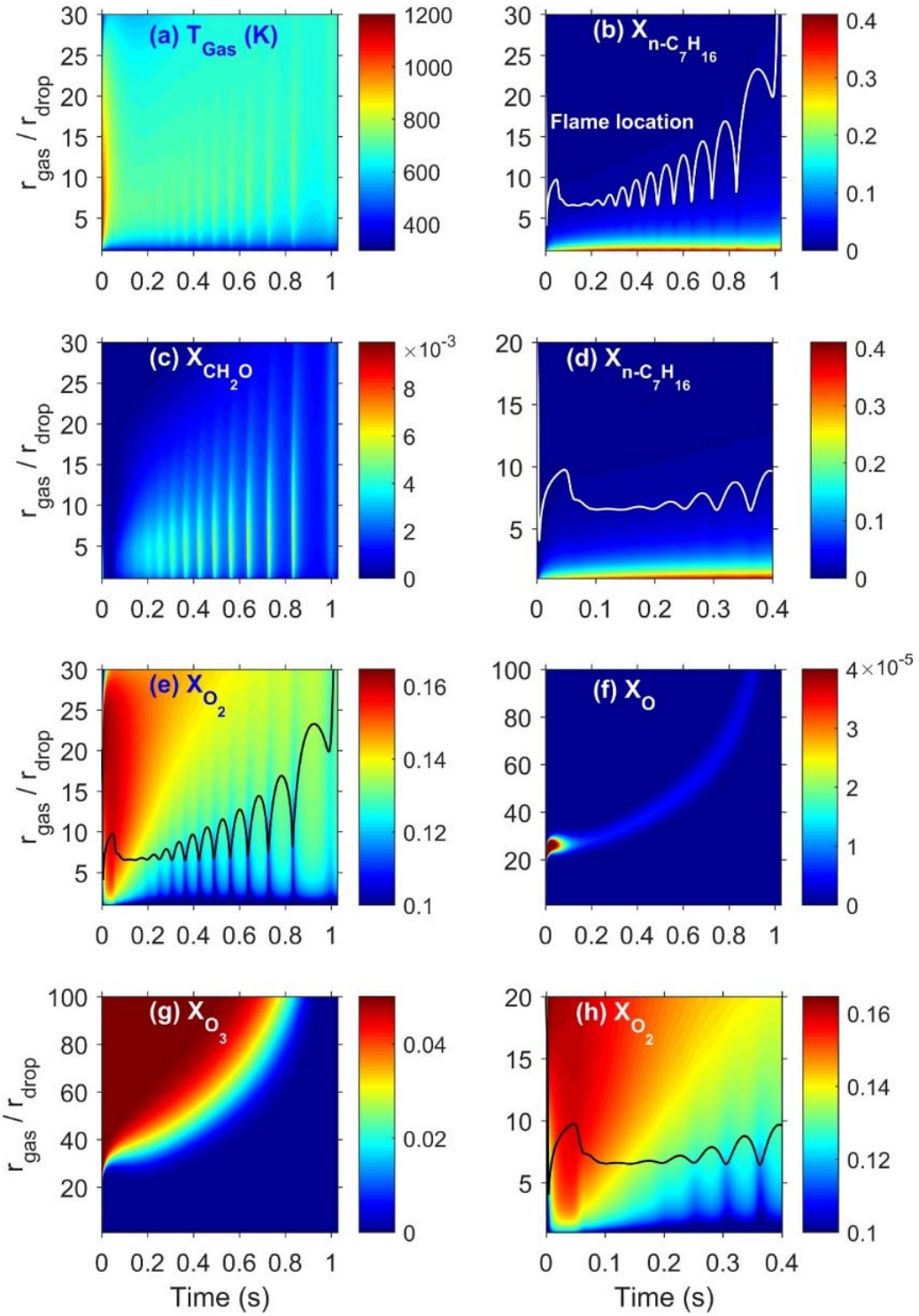

Figure 7.2 Spatiotemporal evolution of (a) gas phase temperature, (b) $X_{n\text{-}C7H16}$ with FSR, (c) X_{CH2O}, (e) X_{O2} with FSR, (f) X_O, and (g) X_{O3} for n-heptane droplet combustion. Subplot (d) and (h) shows $X_{n\text{-}C7H16}$ and X_{O2} distribution during the early transients (D_o = 0.5 mm, X_{O2} = 10%, X_{O3} = 5%, balance X_{N2}, 1 atm). r_{gas}/r_{drop}=1 denotes droplet surface. Subplot (a) is rescaled and attached as supplementary Figure 7.9 for visual clarity.

Figure 7.2 presents the spatiotemporal evolution of the gas phase temperature and selective species (n-C_7H_{16}, CH_2O, O_3, O_2, and O) to display further insights into the oscillatory flame dynamics. The gas phase temperature instantaneously increases to ~1150 K upon initiation energy deposition, consuming the initially evolved stratified fuel vapor/oxidizer layer. As a consequence of the rapid chemical energy heat release, the flame expands radially through the flammable mixture (subplot b), resulting in a gradual decrease in the flame temperature. To accommodate the heat transfer to the liquid to sustain vaporization, the flame eventually contracts and positions itself closer to the droplet surface having an FSR of ~ 6.5. During this period a cool flame burn (T_{max} ~710 K) is stabilized for a brief period of time before transitioning to a continuous the oscillatory flame mode. It is obvious from the X_{O2} distribution (subplot e, h) that ozone in the ambient initially dissociates (primarily via $O_3+N_2 \rightarrow O_2+O+N_2$) from the initial ignition energy deposition and increases the local effective oxygen index in the region from near 0.10 to near 0.16, which is then maintained at that level as the system attempts to attain stable burning. As the burn evolves to the oscillatory mode, the peak X_{O2} in the surrounding is maintained at ~ 0.14. A sharp peak in X_O is also observed at a normalized radial location of ~ 20 during this initial phase. The peak X_O radial location propagates outward as the pulsing cool flame regime progresses and then overlaps with the outer edge of the ozone depletion from the far field concentration (subplot f). For every subsequent pulse, the flame region progressively expands outward, a fraction of the ozone in the outer field is dissociated and locally increases the oxygen index. The evolution of X_{CH2O} shows the onset of the low-temperature kinetics and its extent during the burn time.

A closer look at the X_{O2} and $X_{n\text{-}C7H16}$ spatiotemporal evolution (Figure 7.2 e and h) show the inception of the pulsing behavior. The pulsing initiates when the X_{O2} in the reaction zone (i.e., flame location based on peak temperature) approaches ~ 0.12. The local reduction in the oxidizer drives the flame to move outward during which unreacted X_{O2} diffuses through the reaction zone toward the droplet surface. As the X_{O2} increases in the reaction zone, the flame temperature increases, the flame contracts, depleting the local X_{O2}, and the cyclic process repeats. As the pulsing progress, the time of flame expansion and contraction increases, enabling more X_{O2} to diffuse through the reaction zone, which results in the progressive increase in T_{max} in every pulse. It is interesting to note that at every pulse the flame continues to expand until the X_{O2} near the droplet surface and close to the fuel vapor layer reaches a value of ~ 0.11.

To further understand the kinetic regimes affecting the oscillatory flame, the temperature and selective low-temperature species evolutionary profile for one complete cycle is presented in Figure 7.3. A temporal window of ~0.558-0.638 s is chosen as the fluctuation magnitude of both temperature and species are distinctive at this stage. Figure 7.3 illustrates T_{max} and maximum mole fraction of $\Sigma C_7H_{14}O_3$ and ΣC_7H_{14} profiles. These two species (with cumulative isomers) are considered to represent the extent of influence of hydroperoxyheptyl radical ($C_7H_{14}OOH$) consumption stemming from the competition between chain propagation/termination and degenerate chain branching reactions [27]. The first reaction class converts $C_7H_{14}OOH$ primarily to n-C_7H_{14} (chain termination via HO_2 elimination) and $C_7H_{14}O$+OH (chain propagation). The degenerate chain branching route converts $C_7H_{14}OOH$ to $C_7H_{14}O_3$ through secondary molecular O_2 addition and internal hydrogen abstraction. The figure indicates that T_{max} decreases from a higher value of ~746

K to a saddle value of ~682 K, and then increases to a higher value of ~750 K before entering the next cycle. The evolution of n-C_7H_{14} species can be directly correlated to the temperature progression while the evolution of $C_7H_{14}O_3$ passes through three distinct stages, 1 – 3.

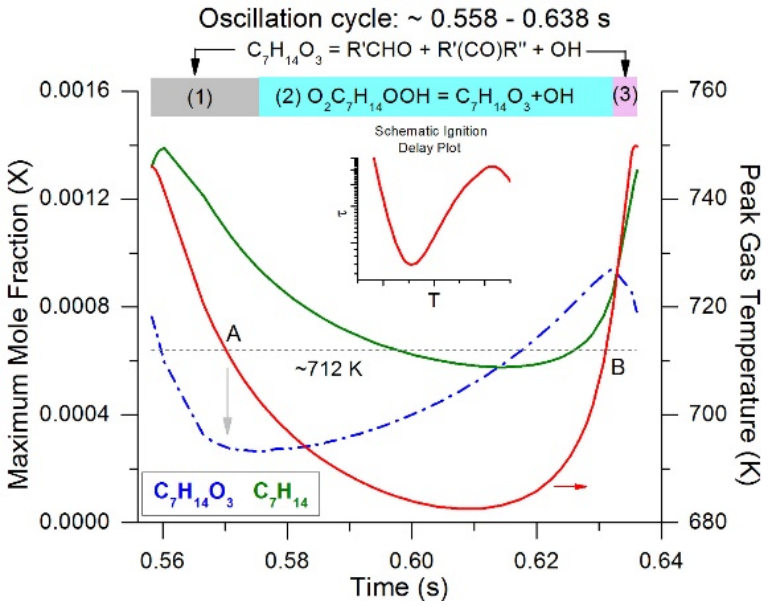

Figure 7.3 Temporal evolution of peak $X_{C7H14O3}$ and $X_{n\text{-}C7H14}$ and T_{max} for an oscillation cycle between ~0.558-0.638 s for the base case. Solid-dash line demarcates the temperature responsible for driving the $C_7H_{14}O_3$ kinetics: threshold temperature for $C_7H_{14}O_3$ kinetics.

Typically, the maximum favorable temperature for $O_2C_7H_{14}OOH$ production hovers around 700 K at atmospheric pressure condition. As the cycle starts from a higher temperature, the production rate diminishes for $O_2C_7H_{14}OOH$ (precursor for $C_7H_{14}O_3$) and the influence is reflected on $C_7H_{14}O_3$ mole fraction evolution and subsequent reduction in heat generation *via* the exothermic $O_2C_7H_{14}OOH = C_7H_{14}O_3+OH$ reaction class. Moreover, the initially high temperature starts to decompose $C_7H_{14}O_3$ through the endothermic reaction class $C_7H_{14}O_3 = R'CHO+R'(CO)R''+OH$ (stage 1). The result is a sharp decrease in temperature as the reaction zone cannot sustain the reaction temperature from the

contribution of exothermic chain branching (QOOH = OH+QO) alone. As a result, the peak n-C_7H_{14} mole fraction also decreases with time. As the temperature drops, the slope of the $C_7H_{14}O_3$ profile changes and at ~0.57 s the saddle point '**A**' (time-coordinate) is reached, beyond which the $C_7H_{14}O_3$ starts to increase (change in slope). It is understandable that the gas phase temperature falls below a 'threshold value' that supports $C_7H_{14}O_3$ formation. This reactivates the exothermic O_2QOOH = $C_7H_{14}O_3$+OH reaction-class and is reflected in the temperature slope change after ~0.58 s. Thus, the simultaneous contribution of heat release from both the degenerate chain branching and chain propagation routes enables the peak temperature to recover. This process continues up to point '**B**' ~0.63 s where the temperature increases sufficiently to force $C_7H_{14}O_3$ production to essentially cease. In essence, in the pulsing regime, the kinetics processes switch back and forth crossing the NTC turnover temperature with every pulsation.

The dynamic competition of chain branching and propagation/termination is also explored in terms of the spatiotemporal evolution of ketohydroperoxide ($C_7H_{14}O_3$) and cyclic ether ($C_7H_{14}O$) presented in Figure 7.4, along with an inlay of the rescaled peak gas temperature evolution. The result of attempting to achieve a steady cool flame initially ($r/r_d<5.0$) for such low-level O_2 ambient is clearly visible from the quasi-steady evolution of both of these species. However, as the oscillation grows, the phase lag between the species starts to become apparent. Chain propagation reactions (QOOH = QO+OH) can be supported at an intermediate temperature (> 800 K) compared to $C_7H_{14}O_3$ kinetics at atmospheric pressure condition. Therefore, at temperatures that exceed the necessary temperature condition, an increase of $C_7H_{14}O$ and decrease/near-depletion of $C_7H_{14}O_3$ mole fraction is observed. The temperature response of these two important reaction classes

(through their representative species peak mole fraction) has been further examined through analyzing the phase diagram presented in Figure 7.5. The plot covers the time span of the entire oscillatory behavior (t>0.125 s) excluding the dynamic initiation phase, and the inset illustrates the magnified view of one representative complete oscillation cycle (t~0.636-0.725 s). The centroid of each of the subplots indicates the inception of flame oscillation that then grows with time. The $C_7H_{14}O_3$ and $C_7H_{14}O$ have semi-oval and skewed-ellipsoidal responses with temperature. The skewed nature of $C_7H_{14}O$ clearly suggests that the production rate of chain propagation reaction couples with the temperature fluctuation and is favored at higher temperatures. On the other hand, the semi-oval shape of $C_7H_{14}O_3$ denotes the presence of a phase lag and corroborates the earlier discussion of the three-stage temperature response over an oscillation. It also indicates that $C_7H_{14}O_3$ kinetics is favored at a lower temperature. Similar response behaviors have been observed in [11] for a near-limit cool flame in a counterflow diffusion flame configuration.

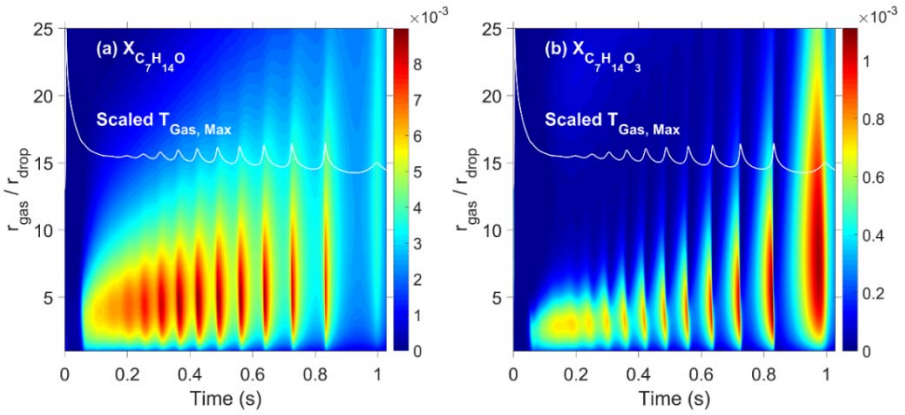

Figure 7.4. Spatiotemporal evolution of (a) X_{C7H14O} and (b) $X_{C7H14O3}$ for n-heptane droplet combustion (d_o = 0.50 mm, X_{O2} = 10%, X_{O3} = 5%, balance X_{N2}, 1 atm). r_{gas}/r_{drop}=1 denotes the droplet surface. A scaled peak gas temperature fluctuation is also overlaid for visual correlation of the species and temperature.

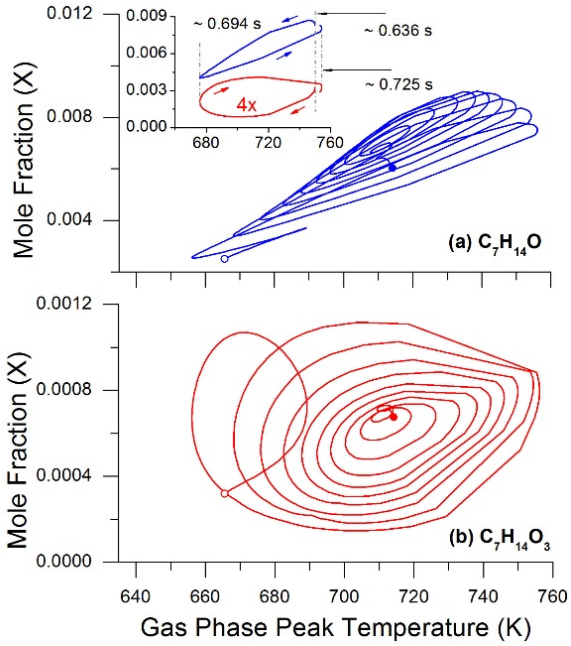

Figure 7.5 Phase diagram summarizing the response of peak (a) X_{C7H14O} and (b) $X_{C7H14O3}$ to temperature over the entire oscillatory time period for the base case. The start and end of the pulsing regime are denoted with the closed and open circle symbol. Subplot (a) inset: magnified view at t~0.636-0.725 s.

In the oscillatory mode of the cool flame burning, the spatial influence of the pulse progressively increases affecting the outer field. This is indicative of the fact that at every pulse, unburnt fuel and fuel fragment continue to build up in the outer region. Figure 7.6 illustrates the $X_{n\text{-}C7H16}$ evolution over time (t~0.48-0.56 s) at three different radial locations with respect to the FSR. Significant amounts of fuel and other fuel-derived species diffuse radially outward through the flame location without being fully consumed by oxidation processes. As a result, a radial growth of the species distribution is observed after every oscillation cycle and there is a build-up of unreacted fuel fragments in the far field as time progresses. For the time-window reported in Figure 7.6, ~34-46% and ~ 13-27% of the fuel vapor within the flame volume escapes the flame zone unreacted and appears at 1.5xFSR and 2.0xFSR respectively. Unreacted fuel vapor and intermediate species (its

derived species/products) continuously pass through the partially-oxidized cool flame location, and their accumulation affects the subsequent growth of the oscillatory behavior outside the peak maximum temperature location.

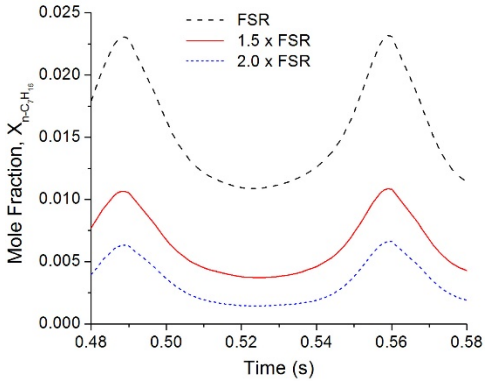

Figure 7.6 Temporal evolution of n-C_7H_{16} mole fraction over time window ~0.48-0.58 s at three different spatial locations for the base case.

To assess the influence of ozone in the pulsing behavior, simulations were conducted for a range of ozone loadings. The temporal evolution of T_{max} for these cases is summarized in Figure 7.7. It is clear that the ozone content of the ambient strongly influences the oscillation patterns. For an oxygen index that is lower than the LOI, the pulsing magnitude decreases with increasing ozone loading. In addition, the pulse frequency is also found to increase as the ozone fraction is increased. For a critical ozone level of X_{O3} = 6.0%, the system transitions to hot-flame burning. It can be inferred from the analysis that under near limit conditions (i.e. LOI) the ozone which was introduced to permit direct initiation of cool flame burning also perturbs the cool flame burning behavior. However, this perturbation effect diminishes and becomes small when larger oxygen index conditions are applied.

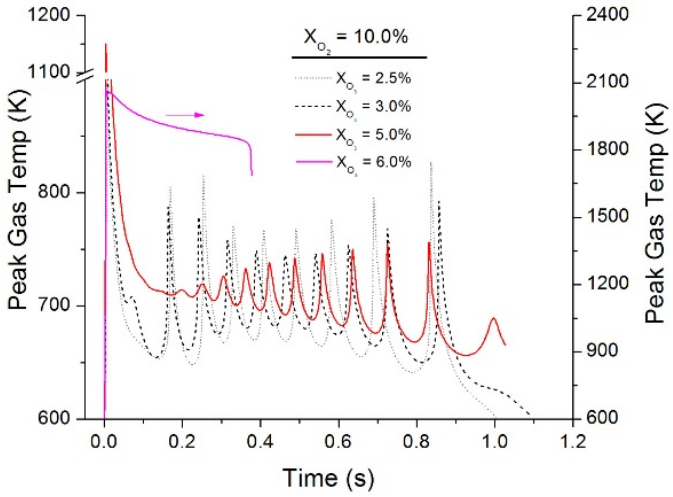

Figure 7.7 Temporal evolution of peak gas temperature under different O_3 mole fractions (see the legend) for n-C_7H_{16} droplet (D_o = 0.5 mm) combustion. Ambient condition: P = 1 atm, T = 298 K, X_{O2} = 10% with balance X_{N2}.

7.5 CONCLUDING REMARKS

The dynamics of near-limit cool flame burning of isolated sub-millimeter sized n-heptane (n-C_7H_{16}) droplet (D_o = 0.5 mm) has been numerically investigated under atmospheric pressure condition. To provide the necessary near limit constraint, the oxygen in the ambient was set to a value that is lower than the limiting oxygen index (LOI) criteria for n-C_7H_{16} and ozone (O_3) was seeded (5% v/v) to the ambient to accomplish cool flame initiation. Based on the detailed analysis, the following features can be drawn as highlighting points for this computational study.

1. At an atmospheric O_2 concentration (21%) with 5% O_3 (both v/v), sub-millimeter sized n-C_7H_{16} droplet attains direct initiation of cool flame upon ignition energy initialization. Heat feedback to the droplet surface stemming from the consequence of 'pre-vaporized fuel + atomic O' reaction contributes as secondary initiation energy.
2. For the exemplary reduced O_2 case (10%), the resultant ignition energy escalates the local gas phase temperature ~1150 K, consuming the fuel vapor near the droplet, and

simultaneously increasing the O_2 mole fraction ~16% (v/v) following the decomposition of O_3. Due to the diffusive/thermo-kinetic balance of heat generation, the system attains a quasi-steady cool flame burn for a brief period of time which then enters an ever-oscillatory low-temperature cool flame burn.

3. It is found that within each full oscillatory cycle, the maximum local gas phase temperature (i.e., flame) resides closest to the droplet, and the flame positions itself to the furthest radial location when its value reaches the cycle minima. At each successive pulse, the flame region (including the reaction zone) progressively grows outward as a result of continuous fuel leakage through the flame location.
4. The inception of oscillation is initiated by the local depletion of O_2 below the critical mole fraction of 12%. This reduction of O_2 compels the flame to grow outside to meet the O_2 requirement for spherical diffusion flame.
5. Further analyses indicate that the dynamic interaction of degenerate chain branching and chain termination/propagation reaction classes of QOOH associated with the low temperature and NTC kinetic regimes, and continuous fuel leakage across the flame location contribute to the ever-increasing trends of the oscillation magnitude. It is found that while the progression of QOOH➔chain propagation/termination reaction class directly correlates with the gas phase temperature field within a full oscillation cycle, the QOOH➔degenerate branching reactions undergo three distinct stages within the same oscillation cycle. The oscillatory burning, which essentially is a perturbation effect resulting from the presence of ozone, is prominent under low ozone loading and diminishes as the ozone fraction in the system is increased.

7.6 SUPPLEMENTARY FIGURES

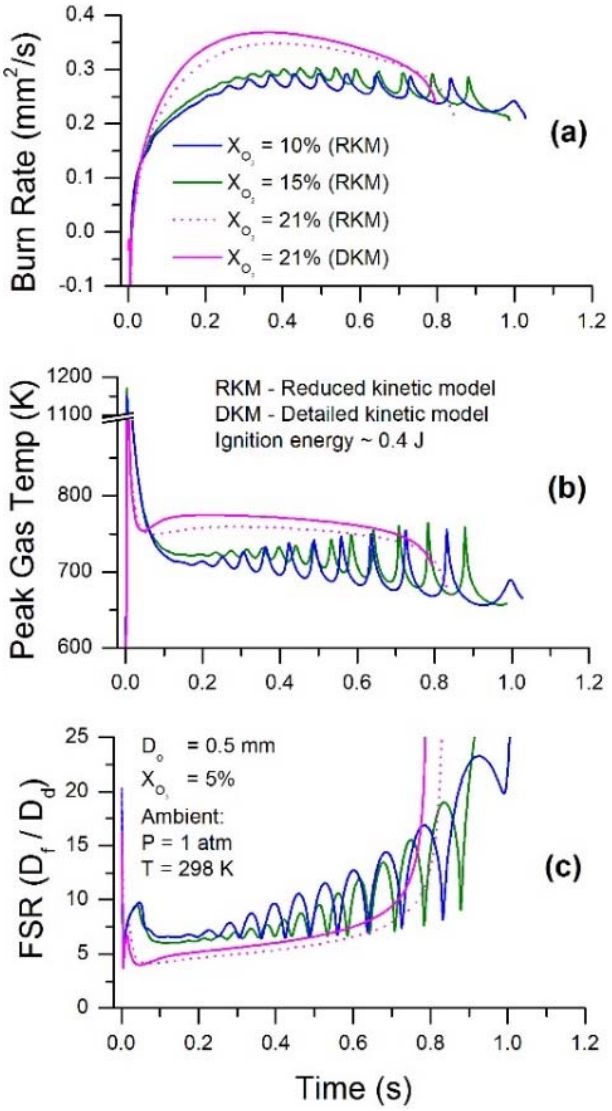

Figure 7.8 Temporal evolution of (a) burning rate, (b) peak gas temperature, and (c) flame stand-off ratio for initial n-C_7H_{16} droplet diameter D_o = 0.5 mm. Three different O_2 mole fraction is considered- X_{O2}=10% (blue), X_{O2}=15% (green) and X_{O2}=21% (magenta). X_{O2}=21% case is simulated employing both the reduced and detailed kinetic models. Ambient condition: X_{O3}=5% with balanced O_2 and N_2. Initial ignition energy is ~0.4 J, P=1 atm and T=298 K.

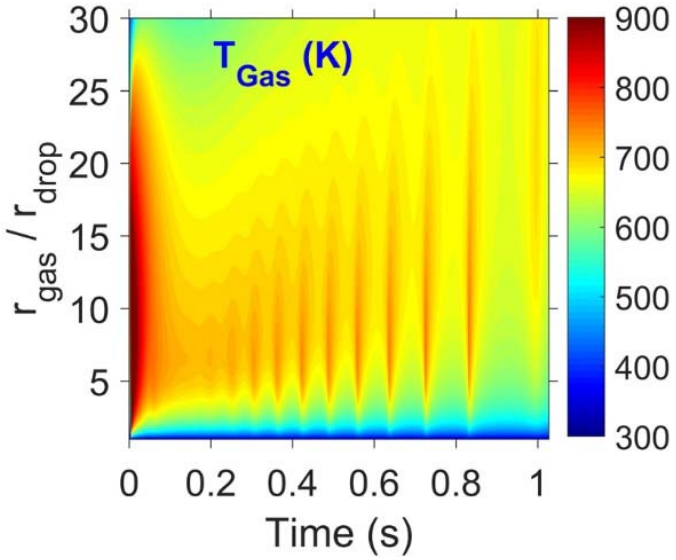

Figure 7.9 Rescaled spatiotemporal evolution of peak gas temperature, previously depicted in Figure 7.2 (a).

7.7 REFERENCES

[1] V. Nayagam, D.L. Dietrich, P.V. Ferkul, M.C. Hicks, F.A. Williams, Can cool flames support quasi-steady alkane droplet burning?, Combustion and Flame, 159 (2012) 3583-3588.

[2] V. Nayagam, D.L. Dietrich, M.C. Hicks, F.A. Williams, Cool-flame extinction during n-alkane droplet combustion in microgravity, Combustion and Flame, 162 (2015) 2140-2147.

[3] D. Dietrich, V. Nayagam, M. Hicks, P. Ferkul, F. Dryer, T. Farouk, B. Shaw, H. Suh, M. Choi, Y. Liu, C.T. Avedisian, F. Williams, Droplet Combustion Experiments Aboard the International Space Station, Microgravity Sci. Technol., 26 (2014) 65-76.

[4] J.E. Dec, Advanced compression-ignition engines—understanding the in-cylinder processes, Proceedings of the Combustion Institute, 32 (2009) 2727-2742.

[5] C.B. Reuter, S.H. Won, Y. Ju, Experimental study of the dynamics and structure of self-sustaining premixed cool flames using a counterflow burner, Combust. Flame, 166 (2016) 125-132.

[6] W. Liang, C.K. Law, Extended flammability limits of n-heptane/air mixtures with cool flames, Combustion and Flame, 185 (2017) 75-81.

[7] C.B. Reuter, M. Lee, S.H. Won, Y. Ju, Study of the low-temperature reactivity of large n-alkanes through cool diffusion flame extinction, Combustion and Flame, 179 (2017) 23-32.

[8] R. Fairlie, J.F. Griffiths, K.J. Hughes, H. Pearlman, Cool flames in space: experimental and numerical studies of propane combustion, Proceedings of the Combustion Institute, 30 (2005) 1057-1064.

[9] S.H. Won, B. Jiang, P. Diévart, C.H. Sohn, Y. Ju, Self-sustaining n-heptane cool diffusion flames activated by ozone, Proceedings of the Combustion Institute, 35 (2015) 881-888.

[10] C.B. Reuter, S.H. Won, Y. Ju, Flame structure and ignition limit of partially premixed cool flames in a counterflow burner, Proceedings of the Combustion Institute, 36 (2017) 1513-1522.

[11] C.H. Sohn, H.S. Han, C.B. Reuter, Y. Ju, S.H. Won, Thermo-kinetic dynamics of near-limit cool diffusion flames, Proceedings of the Combustion Institute, 36 (2017) 1329-1337.

[12] V.R. Katta, W.M. Roquemore, Formation of a cool diffusion flame and its characteristics, Proceedings of the Combustion Institute, 36 (2017) 1369-1376.

[13] S. Deng, D. Han, C.K. Law, Ignition and extinction of strained nonpremixed cool flames at elevated pressures, Combustion and Flame, 176 (2017) 143-150.

[14] A. Cuoci, M. Mehl, G. Buzzi-Ferraris, T. Faravelli, D. Manca, E. Ranzi, Autoignition and burning rates of fuel droplets under microgravity, Combustion and Flame, 143 (2005) 211-226.

[15] T.I. Farouk, F.L. Dryer, Isolated n-heptane droplet combustion in microgravity: "Cool Flames" – Two-stage combustion, Combustion and Flame, 161 (2014) 565-581.

[16] G. Paczko, N. Peters, K. Seshadri, F.A. Williams, The role of cool-flame chemistry in quasi-steady combustion and extinction of n-heptane droplets, Combustion Theory and Modelling, 18 (2014) 515-531.

[17] T.I. Farouk, M.C. Hicks, F.L. Dryer, Multistage oscillatory "Cool Flame" behavior for isolated alkane droplet combustion in elevated pressure microgravity condition, Proceedings of the Combustion Institute, 35 (2015) 1701-1708.

[18] T.I. Farouk, D. Dietrich, F.E. Alam, F.L. Dryer, Isolated n-decane droplet combustion – Dual stage and single stage transition to "Cool Flame" droplet burning, Proceedings of the Combustion Institute, 36 (2017) 2523-2530.

[19] A. Cuoci, A. Frassoldati, T. Faravelli, E. Ranzi, Numerical modeling of auto-ignition of isolated fuel droplets in microgravity, Proceedings of the Combustion Institute, 35 (2015) 1621-1627.

[20] F.E. Alam, S.H. Won, F.L. Dryer, T.I. Farouk, Ozone Assisted Cool Flame Combustion of Sub-millimeter Sized n-Alkane Droplets at Atmospheric and Higher Pressure, Combustion and Flame, (2017, Under review stage).

[21] S. Kukuck, M. Matalon, The onset of oscillations in diffusion flames, Combustion Theory and Modelling, 5 (2001) 217-240.

[22] E.W. Christiansen, S.D. Tse, C.K. Law, A computational study of oscillatory extinction of spherical diffusion flames, Combustion and Flame, 134 (2003) 327-337.

[23] M. Miklavčič, I.S. Wichman, Theoretical and numerical analysis of oscillating diffusion flames, Combustion and Flame, 173 (2016) 99-105.

[24] T.I. Farouk, Y.C. Liu, A.J. Savas, C.T. Avedisian, F.L. Dryer, Sub-millimeter sized methyl butanoate droplet combustion: Microgravity experiments and detailed numerical modeling, Proceedings of the Combustion Institute, 34 (2013) 1609-1616.

[25] A.J. Marchese, F.L. Dryer, V. Nayagam, Numerical modeling of isolated n-alkane droplet flames: initial comparisons with ground and space-based microgravity experiments, Combustion and Flame, 116 (1999) 432-459.

[26] T. Farouk, F.L. Dryer, Microgravity droplet combustion: effect of tethering fiber on burning rate and flame structure, Combustion Theory and Modelling, 15 (2011) 487-515.

[27] M. Mehl, W.J. Pitz, C.K. Westbrook, H.J. Curran, Kinetic modeling of gasoline surrogate components and mixtures under engine conditions, Proceedings of the Combustion Institute, 33 (2011) 193-200.

[28] W. Sun, S.H. Won, T. Ombrello, C. Carter, Y. Ju, Direct ignition and S-curve transition by in situ nano-second pulsed discharge in methane/oxygen/helium counterflow flame, Proceedings of the Combustion Institute, 34 (2013) 847-855.

[29] T.E. Daubert, R.P. Danner, Physical and Thermodynamic Properties of Pure Chemicals, Hemisphere Publishing Corp. , New York, USA, 1989.

CHAPTER 8

CONCLUSION

8.1 PREFACE TO CLOSURE

Combustion of sub-millimeter sized (D_o < 1.0 mm) isolated sphero-symmetric liquid fuel droplets has been numerically studied in this thesis work employing one-dimensional CFD code for renewable alcohol fuels and higher n-alkanes. Methanol (CH_3OH) and butanol (C_4H_9OH, including its four isomers) represent the first category of fuels while n-heptane (n-C_7H_{16}) and n-decane (n-$C_{10}H_{22}$) consist of the second category. Two major forms of flame configurations, namely high temperature and low temperature (including cool) flames, have been extensively studied. In this dissertation, results pertaining to the high-temperature flames are exclusively related to the renewable alcohol fuels, while the low-temperature flames are examined through the higher n-alkanes. To emulate the practical droplet combustion in reduced or near-absence of gravity condition, all the relevant physics are incorporated in the modeling formulation along with detailed description of kinetics. For selective case studies, experimental comparison and validation have also been performed on *ad-hoc* basis against international space station (ISS) and terrestrial drop-tower test data. The unified goal of this research work is to demonstrate the droplet combustion's unique capabilities in relation to both the applied and scientific understanding of fuel combustion. Although each of the fuel has been investigated under the same generic computational framework, i.e., microgravity droplet combustion, the objectives, and consequent research findings from each study are uniquely disparate. The the following section discusses the main contributions and highlighting points arising from this research endeavor.

8.2 MAJOR CONTRIBUTIONS

a. Understanding the fire-suppression mechanism under zero-gravity environment is important in designing next-generation spacecraft fire safety protocols. Practically speaking, it is also very relevant to the existing space programs in relation to inadvertent fire hazards. Therefore, the necessity to assess the effectiveness of different fire-suppressant mediums is critical. However, testing these suppressants under the g~0 condition is logistically challenging and expensive. In this thesis, it has been demonstrated that the computational droplet combustion study can contribute to predicting the fire-extinguishment behavior of any untested gaseous suppressant. An exemplary case has been reported for xenon (Xe) in chapter 3, *the-then* considered as a potential fire extinguisher for space application by the National Aeronautics and Astronautics Agency (NASA). Through exhaustive numerical calculations, it has been unambiguously shown that xenon underperforms compared to other existing fire-suppressants due to its uniquely low thermal diffusivity. As a direct contribution from our research effort, NASA also realized the possible drawbacks of xenon as a micro-gravity fire suppressant and postponed testing and investing resources on it.

b. Robust design of the chemical kinetic model is an intrinsically necessary part of numerical computations for reacting systems. Therefore, the predictive reliability of simulation directly depends on the accuracy and fidelity of the kinetic model itself. In this dissertation, through chapters 4-5, it has been manifested that droplet combustion simulation can be utilized as an effective tool for model validation and refinement. Furthermore, it has also been demonstrated that droplet combustion can surpass the validation capabilities of the traditional gas-phase unsteady homogenous and steady

transport dependent experimental targets. As a benchmark study, the combustion chemistry of butanol and its isomer are considered, and two detailed models (Sarathy et al. 2012, Marchent et al. 2013) have been tested for this purpose against ground base drop tower droplet combustion test data. The initial validation exercise highlighted that the Sarathy et al. model predicted an accelerated fuel burning for butanol isomers, leading us to investigate the primary reason for such anomaly behavior. Through meticulous computational rigor via droplet combustion, the inherent source of the inconsistency for Saraty et al. model has been identified. Following the recommendations from our studies to update fuel specific transport parameters, the model was revised by its authors, the prediction performances improved significantly for both gas and liquid phase targets.

c. The low-temperature kinetic behavior of straight chain paraffinic fuels is unique due to their negative temperature coefficient (NTC) response. And, within the NTC range of temperature, cool flame for droplet is defined as the low-temperature chemistry-driven flame that can support maximum burning rate at a given ambient (P, T) and constraint by the transport phenomena, i.e. diffusive loss/gain. Because of its applied importance to engine knock and ignition in spark and compression ignition engines respectively, and potential for homogeneous charge compression ignition (HCCI) engines, the cool flame has been widely studied in recent years under diversified experimental and computational platforms. However, considering its practical relevance to multiphase spray arrangement, cool flame for sub-millimeter sized droplets has neither been explored experimentally nor computationally. Here, we have advanced the understanding of ozone assisted (O_3) directly initiated smaller fuel droplet (D_o = 0.5

mm) cool flame by employing CFD simulation with detailed kinetics. The mechanistic features of such direct establishment of cool flame are thoroughly explained to encourage the experimental researchers to conduct tests on ground-based drop tower test facilities. In addition, the oscillatory behavior of such smaller droplet cool flame is further investigated to elucidate the kinetic competitions (i.e., pathways) responsible for such oscillatory flame behavior.

8.3 FUTURE RECOMMENDATIONS

The strength of the current version of isolated droplet combustion CFD code stems from the simplicity of low dimensional flow field that augments the coupling of large kinetics and other associated thermo-fluid sub-models. To further transcend its capability, the following recommendations are provided in light of the experiences harnessed through the course of this dissertation work. The author believes that each of the three proposals reported here could be a Ph.D. and/or M.S. level research topic by their own prospect for future exploration.

a. Sooting fuel simulation. To model the sooting fuels, currently, the CFD code has two versions of soot model, namely- the BIN method [1] and the moment method [2]. Both of these soot modeling methods are fairly detailed in nature, therefore the simulation complexity increases tremendously when coupled with detailed gas phase kinetics. A potential way forward to address the soot modeling for droplet combustion is to incorporate semi-detailed soot modeling [3] to reduce the simulation turn over time.

b. The inclusion of real gas formulation. The ideal gas law is a typically the default choice for the equation of states (EOS) for most of the available commercial and in-house legacy codes. This simplified formulation of EOS is found to work satisfactorily at ambient and above ambient pressures for both the reacting and non-reacting CFD simulations. However, ideal gas law starts to underperform significantly as the gas phase system approaches critical pressure regime for the species of interests. Therefore, to address this concern, the real gas effect should be included and the overall code structure has to be updated and validated against experimental targets accordingly.

c. Multi-dimensional effect. Although the one-dimensional droplet combustion is simple in terms of fluid physics, it is relevant to the complex spray combustion by incorporating moving boundary effects, unsteady heat transfer, mass diffusion to and from the droplet surface, temperature dependent variable properties, phase equilibrium at the interface and radiative perturbation. In order to progress towards real spray arrangement without compromising in terms of kinetic aspect, the next step should be to include multi-dimensional effect for isolated droplet combustion. With this end in view, the influence of gravity, external convective perturbation and heat and mass transfer among multiple droplets should be considered.

8.4 REFERENCES

[1] A. Stagni, A. Cuoci, A. Frassoldati, E. Ranzi, T. Faravelli, Numerical investigation of soot formation from microgravity droplet combustion using heterogeneous chemistry, Combustion and Flame, 189 (2018) 393-406.

[2] M. Frenklach, Method of moments with interpolative closure, Chemical Engineering Science, 57 (2002) 2229-2239.

[3] G. Vishwanathan, R.D. Reitz, Application of a semi-detailed soot modeling approach for conventional and low temperature diesel combustion – Part I: Model performance, Fuel, 139 (2015) 757-770.

APPENDIX A

ACADEMIC VITAE

MOHAMMAD FAHD EBNA ALAM
Contact: alamme@email.sc.edu; fahd1@outlook.com

Education

University of South Carolina, SC, USA 04/2018
Ph.D. in Mechanical Engineering (CGPA 3.83/4.00)
Dissertation title: Combustion Behavior of Sub-millimeter Sized Oxygenated and n-Alkane Fuel Droplets
Academic Adviser: Tanvir I. Farouk, Ph.D.
Major Collaborator: Frederick L. Dryer, Ph.D.

National University of Singapore, Singapore 06/2012
M.Sc. in Mechanical Engineering (CGPA 4.45/5.00)
Research project: Engine Performance and Emission Analysis for Biodiesel and Water Emulsion Diesel
Academic Adviser: Siaw K. Chou, Ph.D.

Bangladesh University of Engineering and Technology, Bangladesh 06/2007
B.Sc. in Mechanical Engineering (CGPA 3.67/4.00)

Research Interests

Droplet combustion	Low temperature and NOx kinetics	Speciation diagnostics
Computational fluid dynamics	Fundamental combustion experiment	Engine experiment

Professional Affiliation

The Combustion Institute 07/2013 – present
The American Society for Gravitational and Space Research (ASGSR) 07/2013 – present
The American Society of Mechanical Engineers (ASME) 01/2014 - present

Honors and Awards

1. Breakthrough Graduate Research Award 2017 (Office of research, U of SC, USA)
2. Outstanding Research Award (Presented by the ASGSR in the 29th Annual Meeting, 2013)
3. Conference Travel Grants
   ASGSR (2013, 2015, and 2017)
   The Combustion Institute (2013, 2014, 2015, 2016, and 2017)
   U of SC Graduate School (2014, 2015, and 2017)
4. Session chair, SIAM 16th International Conference on Numerical Combustion (2017)

External Funding

Funding agency (and amount): NASA Physical Sciences Informatics System ($180,000)
Role (and category): Lead PI (Graduate student's original proposal, status- active)
Project: Effect of external thermal and convective perturbation on droplet cool flames

List of Publications

Droplet combustion / Alternative fuels / Low temperature kinetics

1. **F.E. Alam**, T.I. Farouk, F.L. Dryer. Computational study of oscillatory 'cool flame' for sub-millimeter sized n-heptane droplet. Received Excellent / Very good / Very good ratings form the Combustion Symposium '18 reviewers
2. **F.E. Alam**, S.H. Won, T.I. Farouk, F.L. Dryer. Ozone assisted cool flame combustion of sub-millimeter sized n-alkane droplets at atmospheric and higher pressure. In press status, Combustion & Flame, 2018
3. T.I. Farouk, D. Dietrich, **F.E. Alam**, F.L. Dryer. Isolated n-decane droplet combustion - dual stage and single stage transition to "cool flame" droplet burning. Proceeding of the Combustion Institute (Volume 36, 2017)
4. Y.C. Liu[§], **F.E. Alam**[§], Y. Xu, F.L. Dryer, C.T. Avedisian, T.I. Farouk. Combustion characteristics of butanol isomers in multiphase configurations. Combustion & Flame (Volume 169, 2016). [§]Equal contributing author.
5. **F.E. Alam**, T.I. Farouk, F.L. Dryer. Effectiveness of xenon as fire suppressant under micro gravity combustion environment. Combustion Science & Technology (Volume 88, 2016)
6. **F.E. Alam**, Y.C. Liu, C.T. Avedisian, F.L. Dryer, T.I. Farouk. n-Butanol droplet combustion: numerical modeling and reduced gravity experiments. Proceeding of the Combustion Institute (Volume 35, 2015)

NOx kinetics / Fundamental combustion experiment

7. **F.E. Alam**, F.M. Haas, T.I. Farouk, F.L. Dryer. Influence of trace nitrogen oxides on natural gas oxidation: flow reactor measurements and kinetic modeling. Energy & Fuels (Volume 31, 2017)

Diesel engine experiment/ Fuel property characterization

8. **F.E. Alam**, W.M. Yang, P.S. Lee, S.K. Chou, C.R. Yap. Experimental investigation of the performance and emission characteristics of direct injection diesel engine by water emulsion diesel under varying engine load condition. Applied Energy (Volume 102, 2013)
9. **F.E. Alam**, W.M. Yang, P.S. Lee, S.K. Chou, C.R. Yap. Experimental study and empirical correlation development of fuel properties of waste cooking palm-biodiesel and its diesel blends at elevated temperatures. Renewable Energy (Volume 68, 2014)
10. W.M. Yang, H. An, S.K. Chou, S. Vedharaji, R. Vallinagam, M. Balaji, **F.E. Alam**, K.J.E. Chua. Emulsion fuel with novel nano-organic additives for diesel engine application. Fuel (Volume 104, 2013)